ATTOSECOND IONIZATION DYNAMICS IN A MOLECULAR CHARGE-TRANSFER SYSTEM

DISSERTATION
ZUR ERLANGUNG DES AKADEMISCHEN GRADES
DOCTOR RERUM NATURALIUM (DR. RER. NAT.)

VORGELEGT DEM RAT DER CHEMISCH-GEOWISSENSCHAFTLICHEN
FAKULTÄT DER FRIEDRICH-SCHILLER-UNIVERSITÄT JENA

VON

FRIEDRICH GEORG FRÖBEL, M. SC.

geboren am 8. MAI 1988
in STARNBERG

Gutachter:

1. ....
2. ....
(3. ....)

Tag der Verteidigung: ....

Gewidmet meinen Eltern,
Folker & Marianne

Teilergebnisse der vorliegenden Arbeit wurden veröffentlicht in:

> Mirjam Falge, Friedrich Georg Fröbel, Volker Engel, and Stefanie Gräfe. Time-resolved photoelectron spectroscopy of ir-driven electron dynamics in a charge transfer model system. *Physical Chemistry Chemical Physics*, 19(30):19683–19690, 2017.

Teilergebnisse der vorliegenden Arbeit wurden zur Veröffentlichung eingereicht bei:

> *Physical Review A*, received: May 14, 2019. Friedrich Georg Fröbel, Ulf Peschel, Stefanie Gräfe and Alexander Schubert. Attosecond ionization dynamics in a molecular charge-transfer system with correlated electrons.

CONTENTS

A Word on Notation

Throughout this work several variables with physical and/or numerical meaning will be used. In general, bold characters indicate vectors, while circumflexes or hats - as in $\hat{T}$ - indicate operators. Furthermore, if not stated otherwise within the text, following variable assignments will be employed:

Table 1. Variable assignment

Variable	Meaning
$\hat{\mathcal{H}}$	Hamilton operator
Ψ, ψ	wave function
$\widetilde{\psi}$	Fourier transform of ψ
$\mathcal{F}$	operator of the Fourier transform
$\mathbf{r}$	spatial coordinate
t	time
i	imaginary unit
$\hbar$	Planck constant
M, m	mass
$\boldsymbol{\nabla}$	nabla operator
$\mathcal{E}$	electric field
B	magnetic field
E	energy
$\mathbf{A}$	vector potential
Φ	scalar potential
q	charge of a particle
e	elementary charge
e	exponential function

INTRODUCTION

The study of nature has always been the study of nature's constituents, i.e. matter in its broadest sense, and the interaction with more abstract aspects, such as light. The primary means to investigate smaller and smaller objects came to be the interaction with light, and the ability to manipulate the properties of it the limiting factor thereof. By utilization of lenses in eyeglasses during the 13th century, the first type of simple microscopes found widespread application and marked the moment, where optical magnification turned to objects too small to be clearly resolved by the naked human eye [1–3]. Four centuries later, Isaac Newton first adopted the word *spectrum* in his famous experiment to describe how a prism could split white light into the colors of a rainbow, from which ultimately the scientific field specialized in the study of light-matter interactions, *spectroscopy*, would emerge. Since then, many breakthroughs, such as the *flame spectroscopy* [4–6], the discovery of *Bremsstrahlung* [7] that goes to wavelengths far below the visible range, and eventually the coherent light in form of *LASER* [8] allowed for an ever more intricate analysis.

With the beginning of the third millennium, the combination of short wavelengths and coherent light in form of ultrafast coherent x-ray radiation has opened up a new regime of possibilities with different light sources allowing for a variety of applications. Among these sources are huge facilities that produce ultrafast x-ray beams of immense brilliance [9] such as synchrotrons [10] and free electron lasers (FEL) like FLASH in Hamburg, Germany [11], the Linac coherent light source in the SLAC National Accelerator lab in Stanford, USA [12] or the SACLA in Japan [13]. However, table-top sources utilizing high harmonic generation (HHG) start to emerge as well [14–16] and pose an affordable means in creating coherent ultrashort pulses. While synchrotrons and FELs support photon energies throughout the extreme ultraviolet (XUV), soft x-ray and hard x-ray range, HHG sources are only beginning to reach the levels of soft x-ray radiation [17]. At the same time, high harmonic generation enables pulse durations on an attosecond timescale [18], whereas FELs operate upwards of several femtoseconds and synchrotrons on the scale of hundreds of femtoseconds for slicing and picoseconds in normal mode. As such, there is no single light source best suited for every use case, but rather different sources for application, depending on the employed experimental technique and specific scientific question asked.

Among the various parameters of the produced light pulses, the central wavelength as well as the pulse length are of special interest: While the wavelength (or frequency) of an electric field determines the specific light-matter interaction taking place, the pulse length characterizes how narrow the temporal window (spectrally broad the pulse) is, when the interaction occurs. While nuclear dynamics are described on a femtosecond timescale, the dynamics of electronic motion is much faster and requires an attosecond timescale to be adequately resolved [19]. As such, ultrashort pulses open up this new regime of dynamics [14].

Considering molecules in the gas phase, light-matter interaction of few positively charged nuclei and the surrounding electrons are possible to be studied alongside precise simulations [20, 21]. By absorption of a photon, energy is transferred from the light pulse to the molecule and various processes might occur: At first, a change in the electronic structure is initiated, which can lead to non-adiabatic transitions between neighbouring electronic states, potentially triggering a geometry change of the molecule (see e.g. Refs. [22–31]), the formation or the break-up of chemical bonds, or ionization, when one or more electrons are emitted from the molecule. While electrons are strongly accelerated by an external field, nuclei react much slower, however, additional nuclear dynamics may be initiated by the altered electronic structure. Hereby, the charge displacement and the subsequent dynamics can be understood as the molecule's "response" to the external electric field, and go beyond the *Born-Oppenheimer approximation* as soon as non-adiabatic transitions occur. Excitation of electrons to higher states or vibrational modes might occur, where the latter is over time accompanied by a (partial) conversion into heat (see e.g. [32–34]). In general, the ensuing vibrational and electronic dynamics are determined by the occurring energy conversion mechanisms, which are dominated by the fastest (accessible) processes [35–39], where processes of the radiative kind typically take place on a nanosecond or longer, and radiationless processes on a pico- to femtosecond timescale. As such, it is assumed that for most optically excited polyatomic systems, nonradiative processes play a crucial role in determining the energy conversion processes [39, 40].

To investigate molecules typically one of two schemes is employed: When operating with a single pulse of light, the investigated molecule can be analyzed by inspection of the absorbed parts of the pulse, known as *absorption spectroscopy*, the subsequent emission of photons from the sample, known as *fluorescence spectroscopy*, or the measurement of photoelectrons after ionization (*photoelectron spectroscopy*). Alternatively, two or more pulses can be employed, where an altering of the time delay between the individual pulses allows for a time-resolved investigation of the system's response to the first pulse, hence the name *pump-probe spectroscopy*, as the first pulse initiates dynamics which are subsequently probed by the second pulse (see for example Ref. [41]). Within these processes it further needs to be distinguished whether the light pulse is resonant or non-resonant with the various energetic levels of the investigated molecule. In the non-resonant case, the bound electrons are accelerated and behave like a driven oscillator, as such constituting an induced time-dependent dipole with electron dynamics on the attosecond timescale for as long as the pulse interaction lasts. One common practice is the application of a non-resonant field, inducing a polarization within the molecules and aligning them along the beam axis [42]. While this example usually serves as a preparational step before the actual investigation, techniques like *Coherent Diffractive Imaging* (CDI) utilize only a single intense light burst: Ultrashort pulses from the extreme ultraviolet (XUV) to the hard x-ray regime coupled with a high irradiation intensity, as achieved with a FEL, allow for the creation of high resolution diffraction patterns when they hit non-periodic nano-scale objects, such as large biomolecules [43]. Hereby, the ultrashort pulse length ensures that no nuclear displacement occurs during the exposure, which would be visible in the diffraction pattern [44].

Turning to ultrashort pulses resonant with an energetic level of the probed material, pulses operating in the XUV regime have the property that their photon energy typically corresponds to the binding energy of one of the inner shell (core) electrons, which are highly localized (as opposed to the valence electron, which is highly delocalized). From here several different phenomena can occur, which enable different probing techniques: In the *near edge x-ray absorption fine structure* (NEXAFS) scheme, the photon energy is near the ionization barrier, so that the emitted photoelectron has a large chance to scatter at neighbouring atoms. By scanning the photon energy, the recorded absorption spectrum carries structural information on the probed material. Molecular study began with small molecules [45,46], however, research utilizing NEXAFS soon turned to small molecules on surfaces [47, 48] and eventually to complex systems in solution [49, 50]. As the photon energy is increased, more energy is transferred to the photoelectron and scattering becomes less likely, which is known as *extended x-ray absorption fine structure* (EXAFS).

Complementary to (N)EXAFS is the technique of *x-ray fluorescence spectroscopy* (XFS): Here, the photon energy is sufficient to ionize the probed molecule by emission of a core electron as well, however, it is not the absorption spectrum that is measured: Subsequent to ionization, relaxation of an electron from an occupied orbital to the core orbital leads to the emission of a photon, whose frequency corresponds to the energy difference of the involved states, and as such enabling the detection of higher-lying states. However, this process competes with radiationless Auger decay, where the relaxation of a first electron does not lead to photoemission, but the emission of a second electron instead [51, 52]. Typically, Auger decay into a core hole occurs on the timescale of femtoseconds, which is much faster compared to photoemission in the soft x-ray regime [53] and thus increasing the demand for light sources of high photon energies.

The last significant excitation scheme involving a single interaction is the one of *x-ray photoelectron spectroscopy* (XPS), where ionization of the sample leads to the emission of a core electron into the continuum, which exhibits a certain kinetic energy and angular distribution that are subsequently measured [54].

By introduction of a second laser pulse, the dynamics induced by the first pulse can be probed. Usually, an XUV pulse is used to pump the system as described before, and subsequently a field from the near-infrared employed to further address the various channels of decay (cf. e.g. relaxation in iodine [55]). Some of these channels may ultimately lead to fragmentation with the fragments exhibiting a *kinetic energy release* (KER) and angular distribution characteristic to the respective channel, which is measured [56] (cf. fragmentation of a O_2 molecule [57]).

Coupling XPS with an infrared field is known as *streaking spectroscopy*: Here, the emitted electron is accelerated by the IR-field, where its final momentum solely depends on its momentum during ionization and the IR-field's vector potential at the instant of ionization. By varying the XUV arrival time relative to the IR-pulse, the oscillations of the IR-field are reflected in the photoelectron spectrum [58]. A more recent work by Ossiander and coworkers employed attosecond streaking spectroscopy to measure the kinetic energy of an electron emitted from the ground state of helium [59]. Next to the main signal, a lower-energy side-band revealed that the remaining electron had been excited to a higher electronic state, also know as *shake-up*, thus indicating the influence of electronic correlations during ionization. Theoretical works of Awasthi and Saenz before had investigated the (common) application of the single-active electron approximation (SAE) for molecular hydrogen. They found that by ionization with a femtosecond pulse, correlations between electrons cannot be neglected and are visible within the photoelectron spectrum [60, 61].

As outlined, light-matter interaction and, in particular, ionization of molecular samples pose as great tools to investigate intramolecular electronic and nuclear dynamics. By employing pump-probe schemes, time-resolved measurements become possible and allow for the tracking of coupled electronic-nuclear motion. Hereby, newly available sources capable of producing coherent light pulses with femto- and even attosecond durations enable the investigations of dynamics on a timescale not accessible before.

In this context, the presented thesis first employs a molecular charge-transfer model to simulate streaking patterns of coupled electron-nuclear dynamics. Gräfe, Engel and coworkers showed that pump-probe experiments with femtosecond pulses are "well suited for the mapping of vibrational wave packets" [62] and used the model extensively before [63–71].

In this thesis, the impact of the coupled electron-nuclear motion on the measured photoelectron spectrum is theoretically and numerically investigated by variation of the pulse parameters of the ionizing XUV pulse and the NIR-field. Additionally, the behaviour of systems behaving adiabatically, i.e. electrons adjusting quasi-instantaneously to nuclear motion, is compared to diabatic systems, where electrons remain mostly stationary.

In a second step, the molecular model system is extended by a second electron, and electronic correlations are analyzed via attosecond photoelectron spectroscopy. As such, the investigated system describes a molecule as opposed to the helium atom from the works of Ossiander et. al. [59], and furthermore includes electron-nuclear correlations, extending the model of Awasthi and Saenz [60, 61].

The work is structured as follows: Chapter 1 provides the theoretical background of the relevant physical concepts and their numerical implementation required for computer-based simulations. In chapter 2 the employed molecular model system by Shin and Metiu is introduced in detail and the subsequently applied parameter configurations are discussed. The analysis of simulated streaking patterns in the context of adiabatic and diabatic systems is presented in chapter 3. Chapter 4 covers the extension of the previously used model by adding a second electron and investigating the effects of electron-electron correlations during and after ionization. Lastly, the conducted research is summarized and a brief outlook for future research endeavors given.

Chapter

Theory & Implementation Techniques

1

This chapter covers the theoretical background underlying the investigations presented in Ch. 3 – *Time-resolved Photoelectron Spectroscopy of IR-driven Electron Dynamics*, and Ch. 4 – *Attosecond Ionization Dynamics with Correlated Electrons.*

Section 1.1 first introduces the field-free *Time-dependent Schrödinger Equation* (TDSE) followed by the *Time-Evolution Operator*, which is used to solve a wave function's temporal evolution numerically. How precisely the time-evolution operator is applied on a wave function is explained by the *Split-operator Technique.* Next, the *Imaginary Time Propagation* introduces a technique how to numerically obtain a system's eigenstates, which is used to define an initial wave function, $\psi(t = 0, \mathbf{r})$, and analyze its temporal evolution. To interpret the results further, the commonly used *Born-Oppenheimer Approximation* is presented in section 1.2, concluding with a discussion on the approximation's accuracy.

In the next part, external fields are added to the TDSE with section 1.3 covering the description of the *field-interaction Hamiltonian*, $\hat{\mathcal{H}}(t)$ of charged particles in electromagnetic fields. Two possible representations of $\hat{\mathcal{H}}(t)$ in terms of its kinetic ($\hat{T}$) and potential energy terms ($\hat{V}$) are presented in *Length vs. Velocity Gauge.* The advantage of the velocity gauge when propagating individual particles is illustrated in *Cut-off Functions.* As the employed fields have large wavelengths compared to the dimensions of the investigated systems, the *Electric Dipole Approximation* is used to simplify the fields' description.

Lastly, numerical implementation in terms of grids and the application of discretized Fourier transforms is introduced in section 1.5.

1.1 Field-free Propagation Methods

1.1.1 Time-dependent Schrödinger Equation

The temporal evolution of a single-particle wave function $\Psi(\mathbf{r}, t)$ is obtained by solving the *time-dependent Schrödinger equation* (TDSE)

$$\mathrm{i}\hbar \frac{\partial \Psi(\mathbf{r}, t)}{\partial t} = \hat{\mathcal{H}}(t)\Psi(\mathbf{r}, t) = \left[-\frac{\hbar^2}{2m}\boldsymbol{\nabla}^2 + \hat{V}(\hat{\mathbf{r}}, t)\right]\Psi(\mathbf{r}, t), \tag{1.1}$$

with $\hat{V}(\hat{\mathbf{r}}, t)$ denoting a time-dependent potential, $\boldsymbol{\nabla}$ the nabla operator, and m the mass of the particle described [72, 73]. Often times a potential is comprised of a not explicitly time-dependent operator, such as the intramolecular Coulomb potential, and an external perturbation in form an electromagnetic field. For static potentials, i.e. $V(\mathbf{r}, t) = V(\mathbf{r})$, the total wave function can be separated into spatial and temporal terms, $\Psi(\mathbf{r}, t) = \sum_j c_j\, \varphi_j(\mathbf{r})\, f_j(t)$, where Ψ is expressed in terms of a basis set of eigenfunctions φ_j with expansion coefficients c_j respective to their contribution to the total wave function. For a single eigenstate φ_j of the Hamiltonian $\hat{\mathcal{H}}$, Eq. (1.1) becomes

$$\varphi_j(\mathbf{r})\, \mathrm{i}\hbar \frac{\partial f_j(t)}{\partial t} = f_j(t)\left[-\frac{\hbar^2}{2m}\boldsymbol{\nabla}^2 + V(\mathbf{r})\right]\varphi_j(\mathbf{r}), \tag{1.2}$$

$$\frac{\mathrm{i}\hbar}{f_j(t)}\frac{\partial f_j(t)}{\partial t} = \frac{1}{\varphi_j(\mathbf{r})}\left[-\frac{\hbar^2}{2m}\boldsymbol{\nabla}^2 + V(\mathbf{r})\right]\varphi_j(\mathbf{r}). \tag{1.3}$$

As time and spatial dependencies can be separated to the left-hand and right-hand side of Eq. (1.3), both sides must equal a constant. This constant is the state's energy E_j. Inserting this constant into Eqs. (1.2) & (1.3), two ordinary differential equations can be derived:

$$\frac{1}{f_j(t)}\frac{\partial f_j(t)}{\partial t} = -\frac{iE_j}{\hbar}, \tag{1.4}$$

$$\left[-\frac{\hbar^2}{2m}\boldsymbol{\nabla}^2 + V(\mathbf{r})\right]\varphi_j(\mathbf{r}) = E_j\varphi_j(\mathbf{r}). \tag{1.5}$$

The latter equation is known as the *time-independent Schrödinger equation* and $\varphi_j(\mathbf{r})$, consequently, the stationary solution to the system for an individual state. The solution of the former time-dependent equation can readily be found to be

$$f_j(t) = f_j(t_0) \cdot \mathrm{e}^{-\mathrm{i}E_j t/\hbar}, \tag{1.6}$$

where $f_j(t_0)$ is an integration constant, which can be included in c_j. The state's wave function can then be written as

$$\Psi_j(\mathbf{r}, t) = c_j\, \mathrm{e}^{-\mathrm{i}E_j t/\hbar}\, \varphi_j(\mathbf{r}). \tag{1.7}$$

As Eq. (1.7) was built from a single eigenstate, $\Psi_j(\mathbf{r},t) = c_j\, \varphi_j(\mathbf{r})\, f_j(t)$, it represents only a particular solution to the time-dependent Schrödinger equation (1.1). The general solution is a linear combination of all possible eigenstates and their respective expansion coefficients c_j:

$$\Psi(\mathbf{r},t) = \sum_j c_j\, \mathrm{e}^{-\mathrm{i}E_j t/\hbar}\, \varphi_j(\mathbf{r}). \tag{1.8}$$

In the next section it will be shown how to use the time-dependent Schrödinger equation to solve a wave function's temporal evolution numerically without employing the eigenstate representation.

1.1.2 Time-Evolution Operator

On a base level, the goal of this work is to analyze many-particle quantum systems after they have been affected by time-dependent perturbations. The physical quantity used to achieve this is the wave function $|\psi(t)\rangle$ itself. Generally, the temporal evolution of any given system is fully characterized by the Hamiltonian $\hat{\mathcal{H}}(t)$, which is comprised of both, components dependent and independent of time. To describe how a system evolves from any given initial state $|\psi(t_0)\rangle$ into a final state $|\psi(t)\rangle$, one defines the *time-evolution operator* or *propagator* $\hat{U}(t,t_0)$ [74]:

$$|\psi(t)\rangle := \hat{U}(t,t_0)\, |\psi(t_0)\rangle\,. \tag{1.9}$$

Such an operator has to have certain properties to be physically viable:

1. **Unity**
The propagator must conserve the system's norm, i.e.

$$P(t) = \langle\psi(t)|\psi(t)\rangle = \langle\psi(t_0)|\hat{U}^\dagger\hat{U}|\psi(t_0)\rangle = \langle\psi(t_0)|\psi(t_0)\rangle\,, \tag{1.10}$$

which is fulfilled for $\hat{U}^\dagger = \hat{U}^{-1}$.

2. **Time continuity**
The state has to remain unchanged, when start and end point coincide, i.e. when $t_0 = t$:

$$\hat{U}(t,t) = 1. \tag{1.11}$$

3. **Composition property**
The final state has to be the same regardless of whether it is reached in one step ($t_0 \to t_2$) or in multiple steps ($t_0 \to t_1 \to t_2$):

$$\hat{U}(t_2,t_0) = \hat{U}(t_2,t_1)\, \hat{U}(t_1,t_0), \qquad (t_2 > t_1 > t_0). \tag{1.12}$$

Also note that since $\hat{U}$ operates to the right, the order of multiple such propagators matters.

4. **Time reversal**
By exchanging start and end point, the *time-reversal propagator* is defined:

$$\hat{U}(t_0, t)\,\hat{U}(t, t_0) = 1, \tag{1.13}$$

implying $\hat{U}(t_0, t) = \hat{U}^{-1}(t, t_0)$.

By inserting the time-evolution operator from Eq. (1.9) into the TDSE, Eq. (1.1), the time dependence is shifted from the state vector to the propagator (atomic units employed, $m_\mathrm{e} = e = k_\mathrm{e} = \hbar = 1$, k_e being Coulomb's constant):

$$\hat{\mathcal{H}}(t)\,|\psi(t)\rangle = \hat{\mathcal{H}}(t)\;\hat{U}(t, t_0)\,|\psi(t_0)\rangle = \mathrm{i}\,\frac{\partial}{\partial t}\,\hat{U}(t, t_0)\,|\psi(t_0)\rangle\,. \tag{1.14}$$

As Eq. (1.14) holds true for every possible initial state $|\psi(t_0)\rangle$, it must hold true for the operators themselves:

$$\hat{\mathcal{H}}(t)\,\hat{U}(t, t_0) = \mathrm{i}\,\frac{\partial}{\partial t}\,\hat{U}(t, t_0). \tag{1.15}$$

The goal is now to express $\hat{U}(t, t_0)$ solely in terms of the active Hamiltonian. Integration over time on both sides leads to

$$\hat{U}(t, t_0) = 1 - \mathrm{i}\int_{t_0}^{t} \mathrm{d}t_1 \hat{\mathcal{H}}(t_1)\hat{U}(t_1, t_0), \tag{1.16}$$

where the integration constant is derived from the time continuity property. Continuing with this iterative approach, a *Neumann series*,

$$\begin{aligned}\hat{U}(t, t_0) =& 1 - \mathrm{i}\int_{t_0}^{t} \mathrm{d}t_1 \hat{\mathcal{H}}(t_1) + (-\mathrm{i})^2 \int_{t_0}^{t} \mathrm{d}t_1 \int_{t_0}^{t_1} \mathrm{d}t_2 \hat{\mathcal{H}}(t_1)\hat{\mathcal{H}}(t_2) + \ldots \\ &+ (-\mathrm{i})^n \int_{t_0}^{t} \mathrm{d}t_1 \int_{t_0}^{t_1} \mathrm{d}t_2 \cdots \int_{t_0}^{t_{n-1}} \mathrm{d}t_n \hat{\mathcal{H}}(t_1)\hat{\mathcal{H}}(t_2)\cdots\hat{\mathcal{H}}(t_n) + \ldots,\end{aligned} \tag{1.17}$$

is found, where $t_1 > t_2 > \ldots > t_n$ describe the ordering of the time-dependent Hamiltonians. By introduction of a *time-ordering operator* $\hat{\mathcal{T}}$ and utilization of symmetry properties, the individual terms of Eq. (1.17) can be written as

$$\hat{U}_n = \frac{(-\mathrm{i})^n}{n!} \int_{t_0}^{t} \mathrm{d}t_1 \int_{t_0}^{t} \mathrm{d}t_2 \cdots \int_{t_0}^{t} \mathrm{d}t_n \hat{\mathcal{T}}\hat{\mathcal{H}}(t_1)\hat{\mathcal{H}}(t_2)\cdots\hat{\mathcal{H}}(t_n). \tag{1.18}$$

Finally, summation over all terms yields the *Dyson series* [75]:

$$\hat{U}(t, t_0) = \sum_{n=0}^{\infty} \hat{U}_n(t, t_0) = \hat{\mathcal{T}}\mathrm{e}^{-\mathrm{i}\int_{t_0}^{t} \mathrm{d}\tau \hat{\mathcal{H}}(\tau)}. \tag{1.19}$$

Eq. (1.19) represents the most general form of the propagator describing systems not only with a time-dependent Hamiltonian, but also the property of the Hamiltonian not commuting with itself for different times. A typical example for such a system would be a spin$-\frac{1}{2}$ particle in a magnetic field changing its polarization over time.

On the other hand, systems of electric fields whose amplitudes vary over time – as covered in this work – have Hamiltonians that do not commute for different times. However, by numerically calculating $\hat{U}$ for sufficiently small time steps Δt, where $\hat{\mathcal{H}}(t)$ can be assumed constant on time intervals $t \longrightarrow t + \Delta t$, the time-ordering operator $\hat{\mathcal{T}}$ can be dropped for $\Delta t > 0$. This is the so-called *short-time approximation.* The time-evolution operator then reads

$$\hat{U}(t + \Delta t, t) = \mathrm{e}^{-\mathrm{i} \int_t^{t+\Delta t} \hat{\mathcal{H}}(\tau) \mathrm{d}\tau} \approx \mathrm{e}^{-\mathrm{i}\, \hat{\mathcal{H}}(t) \Delta t}. \tag{1.20}$$

For estimating evolution over longer periods of time, $\hat{U}(t+\Delta t, t)$ simply has to be applied consecutively on the initial state:

$$|\psi(t)\rangle = \hat{U}(t, t_0) \, |\psi(t_0)\rangle = \left(\prod_{n=0}^{N} \hat{U}(t_n + \Delta t, t_n) \right) |\psi(t_0)\rangle \, . \tag{1.21}$$

How $\hat{U}(t+\Delta t, t)$ is applied numerically to a wave function will be explained in the next section.

1.1.3 Split-operator Technique

Application of the time-evolution operator on a given state heavily depends on the composition of the system's Hamiltonian. In general, a Hamiltonian can be written as

$$\hat{\mathcal{H}}(t) = \hat{T} + \hat{V}(t), \tag{1.22}$$

where $\hat{T}$ is the kinetic energy operator, and $\hat{V}$ the operator of a potentially time-dependent potential. The former is typically expressed in terms of the momentum operators $\hat{\mathbf{p}}_j$, where j differentiates particles, the latter, $\hat{V}$, on the other hand in terms of particle positions $\hat{\mathbf{r}}_j$. When solving the Schrödinger equation numerically using the short-time approximation, both $\hat{T}$ and $\hat{V}$ are assumed to be constant during a single time step Δt as long as $\hat{V}$ only has a spatial dependence otherwise (e.g. Coulomb interactions). While in spatial representation, $\hat{V}$ can simply be multiplied onto a given wave function,

$$\mathrm{e}^{-\mathrm{i}\, \hat{V}(\hat{\mathbf{r}}) \Delta t} \, |\psi(t)\rangle = \mathrm{e}^{-\mathrm{i}\, V(\mathbf{r}) \Delta t} \, |\psi(t)\rangle \, , \tag{1.23}$$

the momentum operator $\hat{\mathbf{p}}$, however, is expressed as a derivative with respect to the positional coordinate: $\hat{\mathbf{p}} = -\mathrm{i}\hbar \boldsymbol{\nabla}_r$. Therefore, an application of $\hat{\mathbf{p}}$ in momentum space is convenient, as it there simplifies to a mere multiplication as well:

$$\mathrm{e}^{-\mathrm{i}\,\hat{T}(\hat{\mathbf{p}})\Delta t}\,\mathcal{F}\,|\psi(t,\mathbf{r})\rangle = \mathrm{e}^{-\mathrm{i}\,T(\mathbf{p})\Delta t}\,|\widetilde{\psi}(t,\mathbf{p})\rangle\,. \tag{1.24}$$

Here, $\mathcal{F}$ represents the Fourier transformation to momentum space, see Sec. 1.5. At this point, the infinitesimal propagator $\hat{U}(t+\Delta t, t)$ reads [76]

$$\hat{U}(t+\Delta t, t) = \mathrm{e}^{-\mathrm{i}\,\hat{\mathcal{H}}\Delta t} = \mathrm{e}^{-\mathrm{i}(\hat{T}+\hat{V})\Delta t}. \tag{1.25}$$

By splitting propagator $\hat{U}$ into those parts, which can be applied by multiplication in real space and – after Fourier transformation – in momentum space, a numerically efficient solution is obtained.

According to the weaker form of the *Baker-Campbell-Hausdorff formula* [77], operators $\hat{X}$ and $\hat{Y}$ connected via exponential function can be separated as

$$\mathrm{e}^{\hat{X}+\hat{Y}} = \mathrm{e}^{\hat{X}}\,\mathrm{e}^{\hat{Y}}\,\mathrm{e}^{-\frac{1}{2}[\hat{X},\hat{Y}]}, \tag{1.26}$$

where $[\hat{X},\hat{Y}]$ denotes the commutator between $\hat{X}$ and $\hat{Y}$. As $[\hat{T},\hat{V}]$ can only be applied numerically in a cost-inefficient way, an approximation is in order [78]. Simple omission of the commutator part is commonly known as *Lie splitting* [79]:

$$\mathrm{e}^{\hat{X}+\hat{Y}} = \mathrm{e}^{\hat{X}}\,\mathrm{e}^{\hat{Y}}. \tag{1.27}$$

Employing $\hat{T}$ and $\hat{V}$, the Taylor expansion corresponding to the left-hand side of Eq. (1.27) up to the second order in Δt yields

$$\begin{aligned}\mathrm{e}^{-\mathrm{i}(\hat{T}+\hat{V})\Delta t} &= 1 - \mathrm{i}\,(\hat{T}+\hat{V})\Delta t \\ &\quad + \frac{(-\mathrm{i})^2}{2\,!}\Big(\hat{T}^2 + \hat{T}\hat{V} + \hat{V}\hat{T} + \hat{V}^2\Big)\Delta t^2 + \mathcal{O}(\Delta t^3),\end{aligned} \tag{1.28}$$

where $\mathcal{O}(\Delta t^3)$ represents higher-order terms, while the terms in blue depend on the order of the operators. Expanding the separated exponentiated operators (cf. right-hand side of Eq. (1.27)),

$$\begin{aligned}\mathrm{e}^{-\mathrm{i}\,\hat{T}\Delta t}\,\mathrm{e}^{-\mathrm{i}\,\hat{V}\Delta t} &= 1 - \mathrm{i}\,\hat{T}\Delta t - \mathrm{i}\,\hat{V}\Delta t \\ &\quad + \frac{(-\mathrm{i})^2}{2\,!}\Big(\hat{T}^2 + \hat{V}^2 + 2\,\hat{T}\hat{V}\Big)\Delta t^2 + \mathcal{O}(\Delta t^3),\end{aligned} \tag{1.29}$$

one already finds a divergence in the second order in Δt compared to the exact solution. More accurate approximations can be achieved by a symmetric splitting of the operators, so-called *Strang splitting* [80]. For the calculations presented here, symmetric splitting of $\hat{V}$ is applied,

$$\begin{aligned}
\mathrm{e}^{-\mathrm{i}\,\hat{V}\Delta t/2}\,\mathrm{e}^{-\mathrm{i}\,\hat{T}\Delta t}\,\mathrm{e}^{-\mathrm{i}\,\hat{V}\Delta t/2} &= 1-\mathrm{i}\,\hat{V}\frac{\Delta t}{2}-\mathrm{i}\,\hat{T}\Delta t-\mathrm{i}\,\hat{V}\frac{\Delta t}{2}\\
&\quad+(-\mathrm{i})^2\left(\hat{V}\hat{T}+\frac{\hat{V}^2}{2}+\hat{T}\hat{V}\right)\frac{\Delta t^2}{2}\\
&\quad+\frac{(-\mathrm{i})^2}{2\,!}\left(\frac{\hat{V}^2}{4}+\hat{T}^2+\frac{\hat{V}^2}{4}\right)\Delta t^2+\mathcal{O}(\Delta t^3)\\
&= 1-\mathrm{i}\,(\hat{T}+\hat{V})\Delta t\\
&\quad-\frac{1}{2}\left(\hat{T}^2+\hat{T}\hat{V}+\hat{V}\hat{T}+\hat{V}^2\right)\Delta t^2\\
&\quad+\mathcal{O}(\Delta t^3),
\end{aligned}\tag{1.30}$$

which reduces the error to the third order in Δt for the expense of an additional N multiplications.

With this we arrive at the final form of the infinitesimal propagator $\hat{U}(t+\Delta t, t)$ as it is used throughout this work:

$$|\psi(t+\Delta t)\rangle = \mathrm{e}^{-\mathrm{i}\,\hat{V}\Delta t/2}\,\mathcal{F}^{-1}\,\mathrm{e}^{-\mathrm{i}\,\hat{T}\Delta t}\,\mathcal{F}\,\mathrm{e}^{-\mathrm{i}\,\hat{V}\Delta t/2}\,|\psi(t)\rangle\,. \tag{1.31}$$

It should be noted that further splitting is possible. A common splitting procedure involving seven exponential functions was found to reduce the error in Δt to the fourth order making it even more accurate [81]. However, as more Fourier transformations and multiplications have to be computed – and abovementioned splitting proofed working – its usage for this work was forgone.

1.1.4 Imaginary Time Propagation

To analyze a temporal evolution of a given quantum system, it is crucial to know its eigenstates. One way to obtain them numerically is given by the *imaginary time propagation*, also known as *relaxation method* [82].

Starting point is the time-evolution operator from Eq. (1.25) with a variable transformation of $\Delta t \longrightarrow -\mathrm{i}\,\Delta t$. As will be seen, this transformation has some convenient consequences. A state's temporal evolution is then given as

$$\begin{aligned}
|\psi(t+\Delta t)\rangle &= \mathrm{e}^{-\hat{\mathcal{H}}\Delta t}\,|\psi(t)\rangle\\
&= \sum_n \mathrm{e}^{-\hat{\mathcal{H}}\Delta t}\,\langle\varphi_n|\psi(t)\rangle\,|\varphi_n\rangle\\
&= \sum_n \mathrm{e}^{-E_n\Delta t}\,\langle\varphi_n|\psi(t)\rangle\,|\varphi_n\rangle\,,
\end{aligned}\tag{1.32}$$

where the inserted projector $\sum_n |\varphi_n\rangle\langle\varphi_n| = 1$ is used to express the wave function $|\psi\rangle$ in terms of the eigenstates of $\hat{\mathcal{H}}$, i.e. $\{\varphi_n\}$. The initial wave function $|\psi(t=0)\rangle$ can be chosen almost arbitrarily as long as it is not orthogonal to the ground state $|\varphi_0\rangle$.

Effectively, the transformation to negative imaginary time changes how the exponential term impacts the eigenstates $\{\varphi_n\}$: While an imaginary exponential, $\mathrm{e}^{-\mathrm{i}E_n\Delta t}$, acts phase-altering, a negative real-valued exponential dampens the contribution of each individual eigenstate to the total wave function by a factor of $\mathrm{e}^{-E_n\Delta t}$. This means, that by applying the imaginary time propagator repeatedly, all contributions of the eigenstates will be suppressed according to their eigenenergies E_n. Because of that the wave function has to be renormalized for each step of the iteration. By doing so the relative contributions to the total wave function of all states, but the ground state, get reduced over time.

A sensible criterion for deciding when a system has converged into the ground state is given by comparing ground state eigenenergies for two consecutive time steps. The ground state eigenenergy can readily be calculated from Eq. (1.32), after reaching convergence:

$$E_0(t+\Delta t) = -\frac{1}{2\,\Delta t}\ln\left(\frac{\langle\psi(t+\Delta t)|\psi(t+\Delta t)\rangle}{\langle\psi(t)|\psi(t)\rangle}\right), \tag{1.33}$$

where $|\psi(t)\rangle$ is normalized to $\langle\psi|\psi\rangle = 1$, while $|\psi(t+\Delta t)\rangle$ is the wave function before renormalization. Should the change in energy be lower than a certain threshold ϵ,

$$|E_0(t+\Delta t) - E_0(t)| \;<\; \epsilon, \tag{1.34}$$

convergence can be assumed. For the results presented in the following chapters, the threshold value ϵ was chosen to lie one order of magnitude above double precision on a 32-bit computer ($\approx 10^{-16}$), i.e. 10^{-15}.

After calculating the ground state it is now possible to calculate the higher states. For this, the same procedure is applied, however, at the beginning of each time step, all lower states have to be projected out of wave function ψ according to

$$\left|\psi'(t)\right\rangle = |\psi(t)\rangle - \sum_{n=0}^{m-1}\langle\varphi_n|\psi(t)\rangle\,|\varphi_n\rangle\,, \tag{1.35}$$

with m indicating the currently calculated state and $|\psi'\rangle$ being the wave function without contributions of lower states. By doing so, $|\psi'\rangle$ effectively becomes the new lowest populated state.

1.2 Born-Oppenheimer Approximation and its Limits

Molecular systems are often described by the many-particle version of the Schrödinger equation, Eq. (1.1). Analytically it can be solved for up to two-particle systems, as there is no general closed form solution for the three-body problem as of yet. While the *Time-Evolution Operator* and the *Split-operator Technique* represent techniques for solving the time-dependent Schrödinger equation numerically, typically approximations are made to describe many-particle systems. One of these is the *Born-Oppenheimer approximation*, which separates nuclear and electronic degrees of freedom. The molecular Hamiltonian is given as

$$\hat{\mathcal{H}}_{\text{tot}} = \hat{T}_{\text{nucl}}(\mathbf{R}) + \hat{T}_{\text{el}}(\mathbf{x}) + \hat{V}(\mathbf{x},\mathbf{R}), \tag{1.36}$$

with $\mathbf{R}$ and $\mathbf{x}$ denoting the sets of nuclear and electronic coordinates [83, 84]. $\hat{T}_{\text{nucl}}(\mathbf{R})$ and $\hat{T}_{\text{el}}(\mathbf{x})$ are the kinetic energy operators of nuclei and electrons and $\hat{V}(\mathbf{x},\mathbf{R})$ describes the Coulomb interactions of all particles involved. Utilizing atomic units ($m_{\text{e}} = e = k_{\text{e}} = \hbar = 1$) they read:

$$\begin{aligned}
\hat{T}_{\text{nucl}}(\mathbf{R}) &= -\sum_{\alpha} \frac{1}{2M_\alpha} \boldsymbol{\nabla}_\alpha^2 \\
\hat{T}_{\text{el}}(\mathbf{x}) &= -\sum_{i} \frac{1}{2} \boldsymbol{\nabla}_i^2 \\
\hat{V}(\mathbf{x},\mathbf{R}) &= \underbrace{\sum_i \sum_{j>i} \frac{1}{|\mathbf{x}_i - \mathbf{x}_j|}}_{\text{electron repulsion}} + \underbrace{\sum_\alpha \sum_{\beta>\alpha} \frac{Z_\alpha Z_\beta}{|\mathbf{R}_\alpha - \mathbf{R}_\beta|}}_{\text{nucleus repulsion}} - \underbrace{\sum_i \sum_\alpha \frac{Z_\alpha}{|\mathbf{x}_i - \mathbf{R}_\alpha|}}_{\text{attraction}} .
\end{aligned} \tag{1.37}$$

Here, i and j are used for distinguishing electrons, α and β for the nuclei, respectively, $Z_{\alpha,\beta}$ indicate the nuclear charges. The idea is now to separate a system's nuclear and electronic motions, as they respond on different timescales: With the nuclear mass M of a hydrogen atom being approximately 1800 times larger than the electron mass m_e, nuclear motion acts much "slower" to the same Coulomb force compared to the "fast" motion of electrons. While a separation into electronic and nuclear wave functions, which depend solely on either electronic or nuclear coordinates, would be ideal, the attraction term from Eq. (1.37) prohibits this. However, a separation into an electronic wave function, which depends parametrically on the nuclear coordinate is possible, as long as the parametric dependence is continuous and differentiable. The separation of Eq. (1.36) is done according to

$$\hat{\mathcal{H}}_{\text{tot}} = \hat{T}_{\text{nucl}}(\mathbf{R}) + \hat{\mathcal{H}}_{\text{el}}, \text{ with} \tag{1.38}$$

$$\hat{\mathcal{H}}_{\text{el}} = \hat{T}_{\text{el}}(\mathbf{x}) + \hat{V}(\mathbf{x},\mathbf{R}). \tag{1.39}$$

Here, $\hat{\mathcal{H}}_{\text{el}}$ represents the *electronic Hamiltonian*, whose eigenvalue equation is satisfied by the *adiabatic electronic wave functions* $\varphi_n(\mathbf{x};\mathbf{R})$:

$$\hat{\mathcal{H}}_{\text{el}}\varphi_n(\mathbf{x};\mathbf{R}) = \epsilon_n(\mathbf{R})\varphi_n(\mathbf{x};\mathbf{R}). \tag{1.40}$$

$\epsilon_n(\mathbf{R})$ are the corresponding eigenenergies, which depend *parametrically* on the nuclear coordinates[1]. The total wave function can then be expressed as

$$\Psi_{\text{tot}}(\mathbf{x},\mathbf{R}) = \sum_n \varphi_n(\mathbf{x};\mathbf{R})\chi_n(\mathbf{R}), \tag{1.41}$$

where $\varphi_n(\mathbf{x};\mathbf{R})$ denotes the electronic and $\chi_n(\mathbf{R})$ the nuclear part of the total wave function $\Psi_{\text{tot}}(\mathbf{x},\mathbf{R})$. The electronic wave functions $\{\varphi_n(\mathbf{x};\mathbf{R})\}$ form a complete basis set of orthonormal eigenvectors with $\chi_n(\mathbf{R})$ acting as their expansion coefficients with superscript n indicating individual electronic states:

$$\langle\varphi_n|\varphi_{n'}\rangle_x = \delta_{nn'}. \tag{1.42}$$

Here it was only integrated over $\mathbf{x}$, so that $\delta_{nn'}$ holds for any choice of $\mathbf{R}$. The total Schrödinger equation can be written as

$$\sum_n \left[\hat{T}_{\text{nucl}}(\mathbf{R}) + \hat{\mathcal{H}}_{\text{el}}\right]\varphi_n(\mathbf{x};\mathbf{R})\chi_n(\mathbf{R}) = E_{\text{tot}}\sum_n \varphi_n(\mathbf{x};\mathbf{R})\chi_n(\mathbf{R}). \tag{1.43}$$

Note, that up to this point no approximation has been made, and the new representation of the Schrödinger equation is solely achieved by expressing it in terms of the system's eigenfunctions.

Using the definition

$$\hat{T}_{\text{nucl}}(\mathbf{R}) = -\sum_\alpha \frac{1}{2M_\alpha}\boldsymbol{\nabla}_\alpha^2 := \boldsymbol{\nabla}_{\text{nucl}}^2 \tag{1.44}$$

Eq. (1.43) can be expanded into

$$\begin{aligned}
&\sum_n \left[\boldsymbol{\nabla}^2_{\text{nucl}} + \hat{\mathcal{H}}_{\text{el}}\right]\varphi_n\chi_n \\
\Longleftrightarrow &\sum_n \boldsymbol{\nabla}^2_{\text{nucl}}\varphi_n\chi_n + \hat{\mathcal{H}}_{\text{el}}\varphi_n\chi_n \\
\Longleftrightarrow &\sum_n \boldsymbol{\nabla}_{\text{nucl}}\big(\chi_n(\boldsymbol{\nabla}_{\text{nucl}}\varphi_n) + \varphi_n(\boldsymbol{\nabla}_{\text{nucl}}\chi_n)\big) + \chi_n\hat{\mathcal{H}}_{\text{el}}\varphi_n \\
\Longleftrightarrow &\sum_n \chi_n\big(\boldsymbol{\nabla}^2_{\text{nucl}}\varphi_n\big) + 2(\boldsymbol{\nabla}_{\text{nucl}}\chi_n)(\boldsymbol{\nabla}_{\text{nucl}}\varphi_n) + \varphi_n\big(\boldsymbol{\nabla}^2_{\text{nucl}}\chi_n\big) + \chi_n\epsilon_n\varphi_n \\
&\qquad = E_{\text{tot}}\sum_n \varphi_n\chi_n.
\end{aligned} \tag{1.45}$$

---

[1] As will be seen later, it is these electronic eigenenergies which are the potential energy surfaces used to describe the vibrational dynamics in the Born-Oppenheimer picture.

Projecting Eq. (1.45) onto the electronic eigenstate φ_m^* and integrating over the electronic coordinates $\mathbf{x}$ yields

$$\begin{aligned} &\boldsymbol{\nabla}^2_{\text{nucl}}\chi_m + \epsilon_m\chi_m \\ &+\sum_n 2\left\langle\varphi_m|\boldsymbol{\nabla}_{\text{nucl}}|\varphi_n\right\rangle_x \boldsymbol{\nabla}_{\text{nucl}}\chi_n + \left\langle\varphi_m|\boldsymbol{\nabla}^2_{\text{nucl}}|\varphi_n\right\rangle_x \chi_n = E_{\text{tot}}\chi_m, \end{aligned} \tag{1.46}$$

where the orthonormality property from Eq. (1.42) was used. The last two terms on the left hand side of the form $T^{(k)}_{mn} = \langle\varphi_m|\boldsymbol{\nabla}^k_{\text{nucl}}|\varphi_n\rangle$ (with $k = 1, 2$) describe the coupling of different electronic states via derivatives with respect to nuclear coordinates. They are called k-th-order *non-adiabatic coupling elements*, respectively. They are neglected withing the Born-Oppenheimer approximation leading to decoupled nuclear dynamics in different electronic states.

If only coupling terms between electronic states are neglected, but non-adiabatic elements on the main-diagonal are maintained, Eq. (1.46) transforms into

$$\left(\boldsymbol{\nabla}^2_{\text{nucl}} + \epsilon_m + \langle\varphi_m|\boldsymbol{\nabla}^2_{\text{nucl}}|\varphi_m\rangle\right)\chi_m = E_{\text{tot}}\chi_m, \tag{1.47}$$

which is known as *Born-Huang approximation* [85]. Note, that the first-order non-adiabatic coupling element vanishes due to symmetry reasons: This is a result of the orthonormality property of the electronic wave functions (1.42) and the fact, that the $\boldsymbol{\nabla}_{\text{nucl}}$-operator is Hermitian:

$$\begin{aligned} &\langle\varphi_n|\varphi_n\rangle = 1 \\ \Longrightarrow\ &\boldsymbol{\nabla}_{\text{nucl}}\langle\varphi_n|\varphi_n\rangle = 0 \\ &\boldsymbol{\nabla}_{\text{nucl}}\langle\varphi_n|\varphi_n\rangle = \langle\boldsymbol{\nabla}_{\text{nucl}}\varphi_n|\varphi_n\rangle + \langle\varphi_n|\boldsymbol{\nabla}_{\text{nucl}}\varphi_n\rangle \\ \Longleftrightarrow\ &\langle\boldsymbol{\nabla}_{\text{nucl}}\varphi_n|\varphi_n\rangle = -\langle\varphi_n|\boldsymbol{\nabla}_{\text{nucl}}\varphi_n\rangle \\ \text{Hermitian property:}\quad &\langle\boldsymbol{\nabla}_{\text{nucl}}\varphi_n|\varphi_n\rangle \equiv \langle\varphi_n|\boldsymbol{\nabla}_{\text{nucl}}\varphi_n\rangle \\ \Longrightarrow\ &\langle\varphi_n|\boldsymbol{\nabla}_{\text{nucl}}\varphi_n\rangle = -\langle\varphi_n|\boldsymbol{\nabla}_{\text{nucl}}\varphi_n\rangle = 0. \end{aligned} \tag{1.48}$$

For the Born-Oppenheimer approximation the *diagonal correction* term, i.e. $\langle\varphi_m|\boldsymbol{\nabla}^2_{\text{nucl}}|\varphi_m\rangle$, is dropped as well, as it is much smaller compared to ϵ_m due to the nuclear mass entering into the denominator [86]. With this, the nuclear Schrödinger equation in the *Born-Oppenheimer approximation* can be written as

$$\left[\hat{T}_{\text{nucl}}(\mathbf{R}) + \epsilon_m(\mathbf{R})\right]\chi_m(\mathbf{R}) = E_{\text{tot}}\chi_m(\mathbf{R}). \tag{1.49}$$

Eq. (1.49) illustrates how the nuclear motion in the Born-Oppenheimer picture is confined to a single electronic state and how it moves along the potential energy surfaces determined by electronic eigenenergies $\epsilon_m(\mathbf{R})$, obtained from the electronic Schrödinger equation, Eq. (1.40) [87].

Accuracy of the Born-Oppenheimer Approximation

When operating in the Born-Oppenheimer approximation it is important to have an understanding of when it is accurate and when it breaks down. In the last section we saw that the approximation's core components are the non-adiabatic coupling elements $T_{mn}^{(1)}$ and $T_{mn}^{(2)}$ with $m \neq n$. As the latter includes the square of the nuclear gradient operator $\boldsymbol{\nabla}_{\text{nucl}}$ (1.44), it is fair to assume

$$\frac{T_{mn}^{(2)}}{T_{mn}^{(1)}} \ll 1, \tag{1.50}$$

as $\boldsymbol{\nabla}_{\text{nucl}}$ depends on the nuclear mass [83]. As of this, an estimation of $T_{mn}^{(1)}$ shall suffice: It can be found that

$$\langle \varphi_m | \boldsymbol{\nabla}_{\text{nucl}} | \varphi_n \rangle = \frac{\langle \varphi_m | [\boldsymbol{\nabla}_{\text{nucl}}, \hat{\mathcal{H}}_{\text{el}}] | \varphi_n \rangle}{\epsilon_n - \epsilon_m}, \tag{1.51}$$

with ϵ_m and $\epsilon_{n\neq m}$ describing the eigenenergies of electronic eigenstates φ_m and $\varphi_{n\neq m}$, respectively. With this, it becomes apparent that the non-adiabatic coupling terms dramatically increase in the vicinity of two potential energy surfaces getting close to each another, i.e. when $\epsilon_m \approx \epsilon_n$.

Furthermore, Medvedev and Osherov [83] found corrections to wave function and energy derived via perturbation theory:

$$\delta\Psi_{n\nu} \approx \kappa^3 (\epsilon/\Delta\epsilon)^2 \ \Psi_{n'\nu'} \tag{1.52}$$

$$\delta E_{n\nu} \approx \kappa^6 (\epsilon/\Delta\epsilon)^3. \tag{1.53}$$

Here, ν depicts the current vibrational state, ϵ the electronic energy and $\Delta\epsilon$ the energy separation of electronic states with $\kappa = (1/M)^{1/4}$ being the *Born-Oppenheimer parameter* in atomic units.

1.3 Field Propagation Methods

1.3.1 Field-interaction Hamiltonian

The simulations conducted for this work cover multiple charged particles in the presence of electromagnetic fields. For this, the field-interaction Hamiltonian, $\hat{\mathcal{H}}_{\text{int}}(t)$, is derived for a single particle by solving the Euler-Lagrange equation. As such, a classical derivation serves as a means to formulate the quantum mechanical representation of the Hamiltonian (*correspondence principle*). From this, the total Hamiltonian, $\hat{\mathcal{H}}(t)$, is constructed by additionally introducing a potential describing the Coulomb interaction between several particles.

The Lagrangian function L satisfies the Euler-Lagrange equation

$$\frac{\mathrm{d}}{\mathrm{d}t}\frac{\partial L}{\partial \dot{q}_i} - \frac{\partial L}{\partial q_i} = 0, \tag{1.54}$$

where q_i is in general a function of time, $q_i(t)$, and describes the generalized coordinate with i indexing the vector's components. Therefore, the Lagrangian itself is a function of the generalized coordinate, its time-derivative and time, $L = L(\mathbf{q}, \dot{\mathbf{q}}, t)$. Once L has been determined, the Hamiltonian function H can be derived as a conserved quantity of the system via

$$H(\mathbf{q}, \mathbf{p}, t) = \sum_i p_i \dot{q}_i - L(\mathbf{q}, \dot{\mathbf{q}}, t), \tag{1.55}$$

where p_i is the generalized momentum defined as

$$p_i(\mathbf{q}, \dot{\mathbf{q}}, t) = \frac{\partial L}{\partial \dot{q}_i}. \tag{1.56}$$

To find L, the equation of motion (EOM) will be compared to the Euler-Lagrange equation, Eq.(1.54). For a single particle in an electromagnetic field, the EOM is defined by the *Lorentz force* and reads

$$\mathbf{F} = \frac{\mathrm{d}}{\mathrm{d}t}(m\,\dot{\mathbf{r}}) = q\,(\mathbf{E} + \dot{\mathbf{r}} \times \mathbf{B}), \tag{1.57}$$

where the generalized coordinate was chosen as $\mathbf{q} = \mathbf{r} = (x, y, z)$. Note, that q in non-bold notation and without index still represents the particle's electric charge. $\mathbf{F}, \mathbf{E}$ and $\mathbf{B}$ correspond to the vectorized force, electric, and magnetic field with the latter two defined via vector potential $\mathbf{A}$ and scalar field ϕ:

$$\mathbf{E} = -\frac{\partial \mathbf{A}}{\partial t} - \boldsymbol{\nabla}\phi, \tag{1.58}$$

$$\mathbf{B} = \boldsymbol{\nabla} \times \mathbf{A}. \tag{1.59}$$

From the EOM in x direction one finds

$$\begin{aligned}
\frac{\mathrm{d}}{\mathrm{d}t}(m\dot{x}) &= qE_x + q\,(\dot{y}B_z - \dot{z}B_y) \\
&= q\Big(-\frac{\partial A_x}{\partial t} - \frac{\partial \phi}{\partial x}\Big) + q\Big(\dot{y}(\frac{\partial A_y}{\partial x} - \frac{\partial A_x}{\partial y}) - \dot{z}(\frac{\partial A_x}{\partial z} - \frac{\partial A_z}{\partial x})\Big) \\
&= q\,\frac{\partial}{\partial x}(A_x\dot{x} + A_y\dot{y} + A_z\dot{z} - \phi) - q\Big(\frac{\partial A_x}{\partial t} + \dot{x}\frac{\partial A_x}{\partial x} + \dot{y}\frac{\partial A_x}{\partial y} + \dot{z}\frac{\partial A_x}{\partial z}\Big) \\
&= q\,\frac{\partial}{\partial x}(\mathbf{A}\dot{\mathbf{r}} - \phi) - q\frac{\mathrm{d}A_x}{\mathrm{d}t},
\end{aligned} \tag{1.60}$$

where the blue terms $q\,\dot{x}\frac{\partial A_x}{\partial x}$ have been inserted on the third line. After bringing all terms to the left-hand side,

$$\frac{\mathrm{d}}{\mathrm{d}t}(m\dot{x} + qA_x) - \frac{\partial}{\partial x}(q\mathbf{A}\dot{\mathbf{r}} - q\phi) = 0, \tag{1.61}$$

the equation takes the shape of the Euler-Lagrange equation, Eq.(1.54). From the term of the partial derivative, the Lagrangian can be deduced to take the shape

$$L = q\mathbf{A}\dot{\mathbf{r}} - q\phi + f(x, \dot{x}), \tag{1.62}$$

where $f(x, \dot{x})$ must satisfy $\partial f/\partial x = 0$. Assuming the scalar field to be only coordinate-dependent, i.e. $\phi = \phi(x, y, z)$, Eq.(1.62) can be inserted into the first term of the Euler-Lagrange equation, Eq.(1.54). After comparing to Eq.(1.61), one finds

$$\frac{\mathrm{d}}{\mathrm{d}t}\frac{\partial L}{\partial \dot{x}} = \frac{\mathrm{d}}{\mathrm{d}t}\left(qA_x + \frac{\partial f}{\partial \dot{x}}\right) \overset{!}{=} \frac{\mathrm{d}}{\mathrm{d}t}(m\dot{x} + qA_x), \tag{1.63}$$

which holds true for $f(x, \dot{x}) = \frac{m}{2}\dot{x}^2$. Including the other directions, the complete Lagrangian reads

$$L = q\mathbf{A}\dot{\mathbf{r}} - q\phi + \frac{m}{2}\dot{\mathbf{r}}^2. \tag{1.64}$$

Using Eq.(1.56), the generalized momentum is found as

$$\mathbf{p}(\mathbf{q}, \dot{\mathbf{q}}, t) = m\dot{\mathbf{q}} + q\mathbf{A}, \tag{1.65}$$

where the first term describes the mechanical momentum, while the latter corresponds to the field-induced momentum. Consequently, the generalized coordinate can be expressed as $\dot{\mathbf{q}} = \mathbf{p}/m - q\mathbf{A}/m$. Inserting the generalized momentum and the Lagrangian, Eq.(1.64), into the Hamiltonian function, Eq.(1.55),

$$\begin{aligned}
H(\mathbf{q}, \mathbf{p}, t) &= \sum_i p_i \dot{q}_i - L(\mathbf{q}, \dot{\mathbf{q}}, t) \\
&= \mathbf{p}\frac{\mathbf{p} - q\mathbf{A}}{m} - q\mathbf{A}\frac{\mathbf{p} - q\mathbf{A}}{m} + q\phi - \frac{m}{2}\left(\frac{\mathbf{p} - q\mathbf{A}}{m}\right)^2 \\
&= \frac{\mathbf{p}^2 - q\mathbf{p}\mathbf{A} - q\mathbf{A}\mathbf{p} + q^2\mathbf{A}^2}{m} - \frac{\mathbf{p}^2 - q\mathbf{p}\mathbf{A} - q\mathbf{A}\mathbf{p} + q^2\mathbf{A}^2}{2m} + q\phi \\
&= \frac{1}{2m}\left(\mathbf{p}^2 - q\mathbf{p}\mathbf{A} - q\mathbf{A}\mathbf{p} + q^2\mathbf{A}^2\right) + q\phi \\
&= \frac{1}{2m}(\mathbf{p} - q\mathbf{A})^2 + q\phi,
\end{aligned} \tag{1.66}$$

the Hamiltonian function $H(\mathbf{q}, \mathbf{p}, t)$ of a single particle interacting with an electromagnetic field is found. By replacing $\mathbf{p}$ with its operator counterpart, $\hat{\mathbf{p}}$, the interaction Hamiltonian $\hat{\mathcal{H}}_{\text{int}}$ is constructed:

$$\hat{\mathcal{H}}_{\text{int}}(t) = \frac{1}{2m}(\hat{\mathbf{p}} - q\mathbf{A})^2 + q\phi. \tag{1.67}$$

For numerical implementation, it is beneficial to have the Hamiltonian $\hat{\mathcal{H}}_{\text{int}}$ in an as simple as possible representation. As the electric and magnetic fields are the only relevant physical quantities, there exists some freedom in choosing vector potential $\mathbf{A}$ and scalar field ϕ without changing the values of $\mathbf{E}$ and $\mathbf{B}$, the so-called *gauge invariance*[2] [88]. As the electric field will be expressed via Eq.(1.58), it is convenient to construct the scalar field as $\phi = 0$. Expanding the bracket of Eq.(1.66) yields

$$\hat{\mathcal{H}}_{\mathrm{int}} = \frac{1}{2m}\big(\hat{\mathbf{p}}^2 - q(\hat{\mathbf{p}}\mathbf{A} + \mathbf{A}\hat{\mathbf{p}}) + q^2\mathbf{A}^2\big), \tag{1.68}$$

where the momentum has been exchanged for its operator counterpart. Note, that the mechanical momentum $\hat{\mathbf{p}}$ in real-space representation corresponds to the derivative with respect to the particle's position: $\hat{\mathbf{p}} = -\mathrm{i}\hbar\boldsymbol{\nabla}_r$. Because of this, the order of $\hat{\mathbf{p}}$ and $\mathbf{A}$ matters. However, further simplification can be achieved by operating in the *Coulomb gauge* [89] ($\boldsymbol{\nabla}\cdot\mathbf{A} = 0$), where $\hat{\mathbf{p}}$ and $\mathbf{A}$ commute, $\hat{\mathbf{p}}\mathbf{A} = \mathbf{A}\hat{\mathbf{p}}$.[3] Finally, the last term of Eq.(1.68) can be neglected for light sources with comparatively low intensities of up to $10^{15}\ \mathrm{W\,cm^{-2}}$, as it is small compared to the other terms.

For a collection of N charged particles, the total Hamiltonian can then be generalized as

$$\hat{\mathcal{H}}(t) = \sum_{i=1}^{N}\left[\frac{\hat{\mathbf{p}}_i^2}{2m_i} - \frac{q_i}{m_i}\mathbf{A}\hat{\mathbf{p}}_i\right] + \sum_{\substack{i=1\\ j>i}}^{N}\hat{V}(\mathbf{r}_i, \mathbf{r}_j), \tag{1.69}$$

where the last term describes Coulomb interaction between different particles.

1.3.2 Length vs. Velocity Gauge

In the last section, the Coulomb gauge was used to simplify the Hamiltonian $\hat{\mathcal{H}}(t)$ leading to Eq. (1.69). When applying this Hamiltonian during propagation, one operates in the so-called *velocity gauge*. However, this is not the only imaginable gauge of "simple" shape. While operating in different gauges does not change the physics behind the equations, the numerical implementation of one gauge over another might be advisable, as the investigated systems are described on grids of finite size (see Sec. 1.5). For this, we will derive the Hamiltonian for operation in *length gauge*, $\hat{\mathcal{H}}^{\mathrm{LG}}$. As the name suggests, the interaction term of $\hat{\mathcal{H}}^{\mathrm{LG}}$ acts on a grid describing a wave function in real-space representation, while the interaction term(s)[4] in velocity gauge are applied in momentum-space representation.

The relationship of the physical quantities of the electric and magnetic fields $\mathbf{E}$ and $\mathbf{B}$ with vector potential $\mathbf{A}$ and scalar field ϕ were presented in the last

---

[2] The next section goes into more detail on the application of different gauges.

[3] Note that the Coulomb gauge does not automatically imply $\phi = 0$. However, both properties, $\boldsymbol{\nabla}\cdot\mathbf{A} = 0$ and $\phi = 0$, can be satisfied at the same time.

[4] In general, two terms have to be applied for the interaction in velocity gauge, however, for relatively weak fields the $\mathbf{A}^2$ term is usually dropped.

section, Eqs. (1.58) & (1.59). Applying a gauge transformation in the shape of

$$\phi \longrightarrow \phi - \frac{1}{c}\frac{\partial \chi}{\partial t}, \tag{1.70}$$

$$\mathbf{A} \longrightarrow \mathbf{A} + \boldsymbol{\nabla}\chi, \tag{1.71}$$

leaves **E** and **B** unchanged, as

$$(\boldsymbol{\nabla} \times \boldsymbol{\nabla})\chi = 0 \quad \text{for any } \chi. \tag{1.72}$$

Here, χ is the so-called *generating function*. Operation in the velocity gauge (VG), as seen in the last section, is represented by

$$\phi^{\mathrm{VG}} = 0, \tag{1.73}$$

$$\mathbf{A}^{\mathrm{VG}} = \mathbf{A}^{\mathrm{VG}}(t), \tag{1.74}$$

where the *electric dipole approximation* is employed, effectively dropping the spatial dependence of the vector potential (see Sec. 1.4). By introducing a gauge transformation with the generating function

$$\chi = -\mathbf{r} \cdot \mathbf{A}^{\mathrm{VG}}, \tag{1.75}$$

the length gauge is obtained:

$$\phi^{\mathrm{LG}} = -\frac{1}{c}\frac{\partial \chi}{\partial t} = \frac{1}{c}\frac{\partial}{\partial t}\mathbf{r} \cdot \mathbf{A}^{\mathrm{VG}} = \mathbf{r} \cdot \frac{1}{c}\frac{\partial \mathbf{A}^{\mathrm{VG}}}{\partial t} = -\mathbf{r} \cdot \mathbf{E}, \tag{1.76}$$

$$\mathbf{A}^{\mathrm{LG}} = \mathbf{A}^{\mathrm{VG}} + \boldsymbol{\nabla}\big(-\mathbf{r} \cdot \mathbf{A}^{\mathrm{VG}}\big) = \mathbf{A}^{\mathrm{VG}} - \mathbf{A}^{\mathrm{VG}} = 0. \tag{1.77}$$

Using Eq. (1.55), the Hamiltonian in length gauge can be expressed as

$$\hat{\mathcal{H}}^{\mathrm{LG}}(t) = \sum_{i=1}^{N} \left[\frac{\hat{\mathbf{p}}_i^2}{2m_i} - q_i\, \hat{\mathbf{r}}_i \cdot \mathbf{E}(t) \right] + \sum_{\substack{i=1 \\ j>i}}^{N} \hat{V}(\mathbf{r}_i, \mathbf{r}_j), \tag{1.78}$$

where the classical momentum and spatial position variables have been substituted for their quantum mechanical operator counterparts.

Propagation of the systems used in this work yielded the same dynamics for either Hamiltonian, length or velocity gauge. As a consequence, either gauge can be used for an accurate description. However, a special situation arises, when a single particle gets separated from the rest, as can be the case for an electron after emission: In the limit of $\mathbf{r}_i \longrightarrow \pm\infty$, while other particles remain bound, the terms of the Coulomb potential describing the emitted particle's interactions go to zero and can be neglected (cf. chapter 3). Separating this part from the wave function, the Hamiltonian for the particle far from the others simplifies to

$$\hat{\mathcal{H}}_{\text{far}}^{\text{LG}} = \frac{\hat{\mathbf{p}}^2}{2m} - q\,\hat{\mathbf{r}} \cdot \mathbf{E}, \tag{1.79}$$

$$\hat{\mathcal{H}}_{\text{far}}^{\text{VG}} = \frac{\hat{\mathbf{p}}^2}{2m} - \frac{q}{m}\mathbf{A}\hat{\mathbf{p}}. \tag{1.80}$$

Here, the Hamiltonian in velocity gauge, Eq. (1.80), only contains the momentum operator, and hence is solely applied in the Fourier domain. As the evolution of this part can exclusively be described in momentum space, the spatial coordinate can be dropped entirely. This is especially advantageous for propagations, where parts of the wave function get driven to large coordinates (cf. Ch. 3) as they would get reflected at a grid's end[5]. Covering these cases would usually require big spatial grids, which in turn scale computational costs tremendously. To combat this, it is advisable to employ smaller grids and propagate isolated particles separately with the Hamiltonian in velocity gauge. The next section, *Cut-off Functions*, goes into more detail.

1.3.3 Cut-off Functions

A common area of molecular investigations concerns dissociative and ionizing processes. While “bound” dynamics occur in the vicinity of a studied system, the process of electron emission covers regions far from the system's initial position. Consequently, large numerical grids are required to describe situations, where the emitted part and the remaining bound part of the system are described at the same time. However, often it is possible to separate the system's total wave function into an inner and and outer, asymptotic region [90]:

$$\psi_{\text{tot}} = \psi_{\text{in}} + \psi_{\text{out}}. \tag{1.81}$$

As introduced in the last section, 1.3.2 – *Length vs. Velocity Gauge*, the parts of a wave function describing individual particles spatially far from others, i.e. ψ_{out}, have vanishing Coulomb interaction terms, and thus a different Hamiltonian, $\hat{\mathcal{H}}_{\text{far}}$, when being propagated. Utilizing this Hamiltonian in the velocity gauge, Eq. (1.80), propagation takes place exclusively within momentum space. While this is computationally beneficial on its own, it also allows to drop the spatial representation at all times, which means, that a spatial description of the entire system can be limited up to the point, where particles start to be considered emitted. By doing so, dissociative processes and ionization can be well described.

---

[5] An inherent property of numerical implementation.

To split the outer part from the total wave function a so-called *cut-off function*, $c(x)$, is introduced as

$$\begin{aligned}\psi_{\text{out,new}}(x,R) &= \quad c(x) \quad \cdot\ \psi_{\text{tot}}(x,R), &(1.82)\\ \psi_{\text{in}}(x,R) &= [1-c(x)]\ \cdot\ \psi_{\text{tot}}(x,R). &(1.83)\end{aligned}$$

This cut-off function is applied after each time-step during the propagation, so that the parts of the wave function, which get separated, are "collected". After the new parts within the outer regions have been identified they are added coherently to the parts that have reached the outer region before them,

$$\psi_{\text{out}}(p_x,R,t+\Delta t) = \psi_{\text{out}}(p_x,R,t) + \mathcal{F}_x\,\psi_{\text{out,new}}(x,R), \tag{1.84}$$

where $\mathcal{F}_x$ is the Fourier transform with respect to the x coordinate. In this context, "adding coherently" simply means that the outer part of the wave function has to be propagated as well – although with its own Hamiltonian, i.e. $\hat{\mathcal{H}}^{\text{VG}}_{\text{far}}$.

Special care has to be taken when selecting an appropriate cut-off function, c: A sharp cut-off function – with the extreme being a Heaviside step function θ – induces higher frequency components in the momentum domain requiring larger momentum grids [91]. For this reason, a smooth function has to be chosen. The investigations presented in Ch. 3 are obtained by employing a two-dimensional grid, using x and R to describe an electronic and a nuclear coordinate, respectively. In that scenario, a cut-off function, $c(x,R)$, has been defined as

$$c(x) = \left[1 + e^{\left(|x|-\frac{3}{4}x_{\max}\right)\frac{R_{\max}}{x_{\max}}\beta}\right]^{-1}, \tag{1.85}$$

where $x_{\max}$ and $R_{\max}$ are the maximum coordinates of their respective grids, while β acts as smoothing parameter. Fig. 1.1 shows $c(x)$ employing the parameters from Ch. 3. A cut-off function like this means that electrons, which have reached a certain distance from a molecule located at $x = 0\,\text{Å}$ are considered as not coming back and hence being emitted.

While it seems obvious to describe a cut-off function in terms of the position where it starts to take effect, the actual position is of less importance once a certain threshold value on the respective spatial grid has been surpassed. The shape of the cut-off function is more crucial. As will be shown in Sec. 1.5, spatial and momentum grids cannot be chosen independently from one another, making the choice of a cut-off function an important matter.

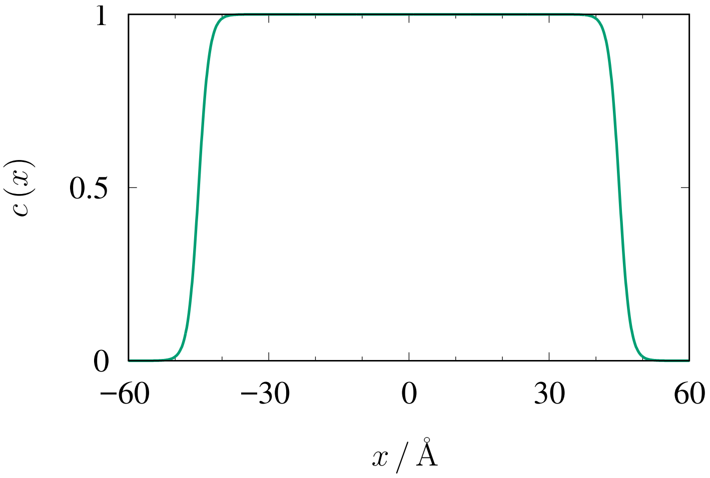

Figure 1.1. Example cut-off function $c(x)$ with $x_{\max} = 60\,\text{Å}$, $R_{\max} = 4\,\text{Å}$ and $\beta = 7\,\text{Å}^{-1}$. Note, that the mask starts to take effect at around $|x| \approx 40\,\text{Å}$ with certain ionization beyond $|x| \approx 50\,\text{Å}$.

1.4 Electric Dipole Approximation

A propagating electric field as the solution to *Maxwell's equations* is typically described by its amplitude, potentially an envelope function, and a trigonometric dependence on a phase factor. Latter is generally expressed in terms of the field's angular frequency ω and its wave vector given by $\mathbf{k}$ so that

$$\mathbf{E}(\mathbf{r}, t) \propto \mathrm{e}^{\mathrm{i}(\omega t - \mathbf{k}\cdot\mathbf{r})}, \tag{1.86}$$

where $\mathbf{k} = \omega/c \cdot \mathbf{n}_\mathrm{k} = 2\pi/\lambda \cdot \mathbf{n}_\mathrm{k}$, with $\mathbf{n}_\mathrm{k}$ being the unit vector in propagation direction and c the speed of light. Expanding the part dependent on the spatial position, $\mathrm{e}^{\mathrm{i}\mathbf{k}\cdot\mathbf{r}}$, into a Taylor series yields

$$\mathrm{e}^{\mathrm{i}\mathbf{k}\cdot\mathbf{r}} = \mathrm{e}^{\mathrm{i}(\omega/c)\mathbf{n}_\mathrm{k}\cdot\mathbf{r}} = 1 + \mathrm{i}\frac{\omega}{c}\mathbf{n}_\mathrm{k} \cdot \mathbf{r} + \ldots, \tag{1.87}$$

which can be approximated by its leading term for typical light fields and small atoms or molecules. In general the relation

$$\frac{\omega}{c}\mathbf{r} = \frac{2\pi}{\lambda}\mathbf{r} \ll 1 \tag{1.88}$$

must be satisfied for the approximation to hold.

$$\omega t - \mathbf{k} \cdot \mathbf{r} \approx \omega t \tag{1.89}$$

is commonly known as the *electric dipole approximation* [92]. The molecules covered in this work extend over a region of 10 Å, while the shortest wavelength employed is 39.5 nm, thus easily meeting the approximation's conditions. Note

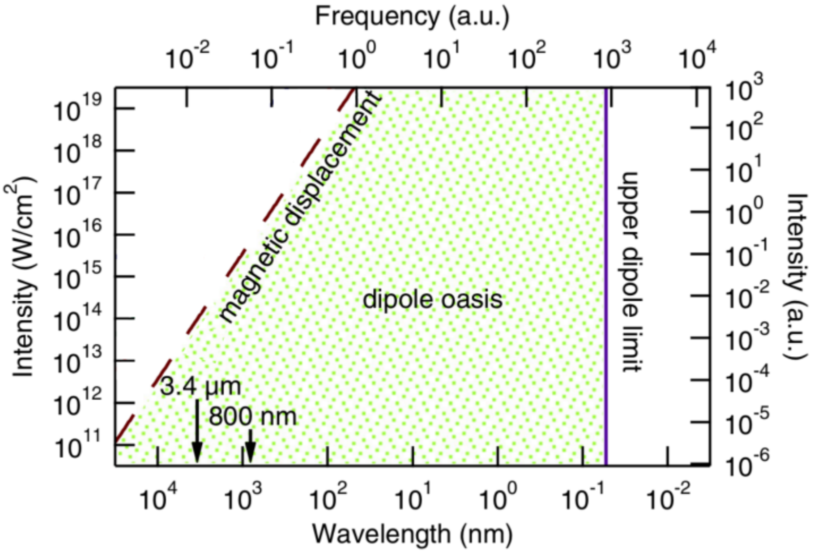

Figure 1.2. Limits of the dipole approximation for a hydrogen atom. While short wavelengths ultimately lead to a breakdown of the dipole approximation, long wavelengths in combination with high field intensities can encompass magnetic and relativistic effects as well. The green dotted area indicates the regions, where the dipole approximation is applicable for a hydrogen atom. Source (modified): Ludwig, Andre, et al. "Breakdown of the dipole approximation in strong-field ionization." Physical Review Letters 113.24 (2014): 243001. [93]

that strong fields accelerate electrons of the molecule to regions beyond 10 Å, however, for the calculations presented, this only happens after the fields are already gone, so that the approximation can still be applied.

Low-frequency Limit

As every natural electric field is accompanied by a magnetic field, there exists also a low-frequency, intensity-dependent limit on the dipole approximation [93]. Figure 1.2 highlights the regions, where the dipole approximation is applicable. As the employed fields are within the boundaries of the "dipole oasis", the low-frequency, intensity-dependent limit is not met.

1.5 Numerical Discretization and Discretized Fourier Transformations on Grids

Traditional computers perform calculations pointwise, i.e. for a given input value an output value is produced. For this, functions $f(x)$ are discretized and represented on a grid f_n with N being the total number of points within the grid and n the current point's position or *index*. If a function is derived from already discretized quantities, their discretization or grid size is also defining the function's discretization:

$$f_n = f(x_n) \quad \text{with} \quad x_n = x_0 + n \cdot \mathrm{d}x \;,\; n \in \{0, 1, 2, ..., N-1\}. \tag{1.90}$$

Here, x_0 is the starting value of the grid and dx its spacing. If computational resources allow it, it is usually best to discretize a function by as many points as possible and/or small spacing dx. However, for some quantities special care has to be taken:

If two variables are connected via *Fourier transformation* $\mathcal{F}$, their discretizations are not independent. An example of such variables would be spatial coordinate x and momentum p:

$$\widetilde{\psi}(p) = \quad \mathcal{F}\ \psi(x) = \frac{1}{2\pi} \int \psi(x)\, \mathrm{e}^{-\mathrm{i}px} \mathrm{d}x, \tag{1.91}$$

$$\psi(x) = \mathcal{F}^{-1}\ \widetilde{\psi}(p) = \int \widetilde{\psi}(p)\, \mathrm{e}^{\mathrm{i}px} \mathrm{d}p, \tag{1.92}$$

with $\widetilde{\psi}$ marking the Fourier transform of ψ and $\mathcal{F}^{-1}$ being the backward transformation[6].

Of course, computing Fourier transforms on discretized variables also requires a discretized definition thereof:

$$\widetilde{\psi}(p_j) = \frac{1}{2\pi N} \sum_{k=0}^{N-1} \psi(x_k) \mathrm{e}^{-\mathrm{i}p_j x_k}, \tag{1.93}$$

$$\psi(x_k) = \sum_{j=0}^{N-1} \widetilde{\psi}(p_j) \mathrm{e}^{\mathrm{i}p_j x_k}, \tag{1.94}$$

with j and k being indices of their respective grids. As the Fourier transform will be employed for solving the time-dependent Schrödinger equation (Sec. 1.1.3 – *Split-operator Technique*, p. 11), parameters specifying spatial and momentum grids must be chosen carefully, so that the wave function ψ and its transform $\widetilde{\psi}$ are always sufficiently and unambiguously described.

---

[6] It should be pointed out, that there is some freedom in assigning the prefactor for the forward and backward transformations and other definitions of Eqs. (1.91) and (1.92) do exist.

The spatial resolution and the total covered real space, i.e $\mathrm{d}x$ and $N \cdot \mathrm{d}x$, also define $\mathrm{d}p$ and the covered momentum space $N \cdot \mathrm{d}p$ with

$$\mathrm{d}p = \frac{2\pi}{N \cdot \mathrm{d}x}. \tag{1.95}$$

Note, however, that while the momentum resolution and covered momentum space follow from the choice of the real space grid, there exists some freedom for choosing the range of the momentum grid, i.e. the starting point of the grid. This stems from the fact, that the momentum representation is periodic on the momentum grid. Consequently, one point on the momentum grid corresponds – in principle – to several momenta [94, 95].

For the investigations conducted in this work, a momentum grid is chosen as

$$p_n = \begin{cases} n \cdot \mathrm{d}p, & n \in \{0, 1, 2, ..., N/2 - 1\}, \\ (n - N) \cdot \mathrm{d}p, & n \in \{N/2, N/2 + 1, ..., N - 1\}, \end{cases} \tag{1.96}$$

consisting of the value zero, $N/2 - 1$ positive, and $N/2$ negative values.

As the numerical calculations of Fourier transforms as in Eqs. (1.93, 1.94) are computationally highly demanding, it is advised to employ the "FFTW 3" libraries ("**F**astest **F**ourier **T**ransform in the **W**est"), which make use of symmetry properties to fasten the calculation [96]. Value zero in the momentum grid is a requirement of the FFTW 3 libraries, while the choice for the positive and negative lobes of the momentum grid is motivated by the employed model system, Ch. 2, where particle acceleration occurs equally in *forward* (positive momenta) and *backward* direction (negative momenta).

CHAPTER

2

Shin-Metiu Model

The *Shin-Metiu model* [97, 98] constitutes the basis of the investigations presented in Chapters 3 and 4 and will be introduced here, while specific implementation is given in the respective chapters. Section 2.1 presents the original system from 1995, employing a single electron, while Sec. 2.2 covers the extension by a second electron as first introduced by Engel and coworkers in 2004 & 2012 [65, 68].

2.1 Single-electron Version

In 1995 Seokmin Shin and Horia Metiu published a study of non-adiabatic effects on the charge transfer rate [97]. Therein, an artificial molecular model system is assembled, where three ions and one electron are strung on a line. The ions are described as nuclei with a charge of $Z = Z_1 = Z_2 = 1$ elementary charges, thus resembling an ionized linear version of H_3^{2+}, with two of the nuclei being stationary at the left- and right-hand side, marking the outer boundaries of the molecule. The remaining nucleus and the electron are mobile and able to move along the molecule's axis, described by the coordinates R and x, respectively. Fig. 2.1 shows the particle configuration.

The strength of the model lies in its simplicity. By having only two degrees of freedom – the mobile nucleus and electron in a single dimension – the dynamics of the system can be solved numerically without the Born-Oppenheimer approximation. In particular, charge-transfer processes, where the nucleus moves from one side of the molecule to the other, are of interest, as the present electron can act as instigator for the dynamics by "pulling" the nucleus to the other side, or as inhibitor when it "glues" the nucleus to its side. The same is true vice versa, when the nucleus moves and the electron instantaneously follows.

While simple, there do exist real-world systems, that are resembled by the model: In doped zeolite[1], a pair of an electron and a sodium ion can transition

---

[1] Doped zeolite actually inspired Shin and Metiu to come up with their model in the first

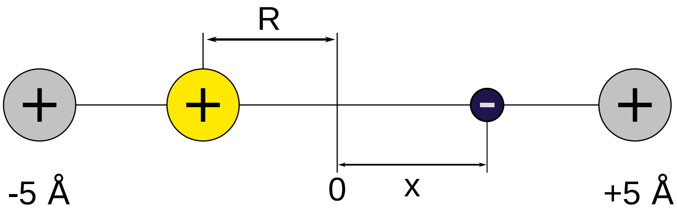

Figure 2.1. Particle configuration of the original Shin-Metiu model [97]. While the outer nuclei are fixed at their positions, the middle nucleus and the electron can move along the molecule's axis according to their coupled dynamics or applied, external fields.

from one zeolite cage to a neighbouring one corresponding to a charge transfer [99–101]. In a more general way, the moving ion can be viewed as a particle of a "medium" which is displaced as the electron changes locations, thus describing polarization [97].

The other big strength of the Shin-Metiu model stems from the fact, that by varying a single parameter in the description of the system's potential, the dynamics can be switched from a more adiabatic to a diabatic type.

2.1.1 Potential

The potential $V(x,R)$ of the single-electron Shin-Metiu model reads (in atomic units)

$$\begin{aligned} V(x,R) = & \frac{Z_1\,Z}{|L/2-R|} + \frac{Z_2\,Z}{|L/2+R|} - \frac{Z_1\,\mathrm{erf}(|L/2-x|/R_\mathrm{f})}{|L/2-x|} \\ & - \frac{Z_2\,\mathrm{erf}(|L/2+x|/R_\mathrm{f})}{|L/2+x|} - \frac{Z\,\mathrm{erf}(|R-x|/R_\mathrm{c})}{|R-x|}, \end{aligned} \tag{2.1}$$

where $\pm L/2$ with $L = 10\,\text{Å}$ are the fixed nuclei's positions, while R_f and R_c are truncation parameters to describe the Coulomb interaction between the electron and the fixed nuclei (R_f) and the mobile nucleus (R_c), respectively. The Coulomb interaction is further expressed via the error functions (erf) in order to avoid numerical instabilities. (See next section for more details.)

Fig. 2.2a shows the system's potential for parameters of $Z = Z_1 = Z_2 = 1$ and $R_\mathrm{f} = R_\mathrm{c} = 1.5\,\text{Å}$. The pattern loosely resembles the letter "z", where the horizontal bars correspond to electronic positions near the fixed outer nuclei, while the diagonal bar represents positions near the mobile nucleus. In contrast, Fig. 2.2b shows the potential for a configuration with $R_\mathrm{c} = 2.5\,\text{Å}$ resulting in deeper wells at the outer nuclei, and a lower one around the mobile nucleus.

---

place.

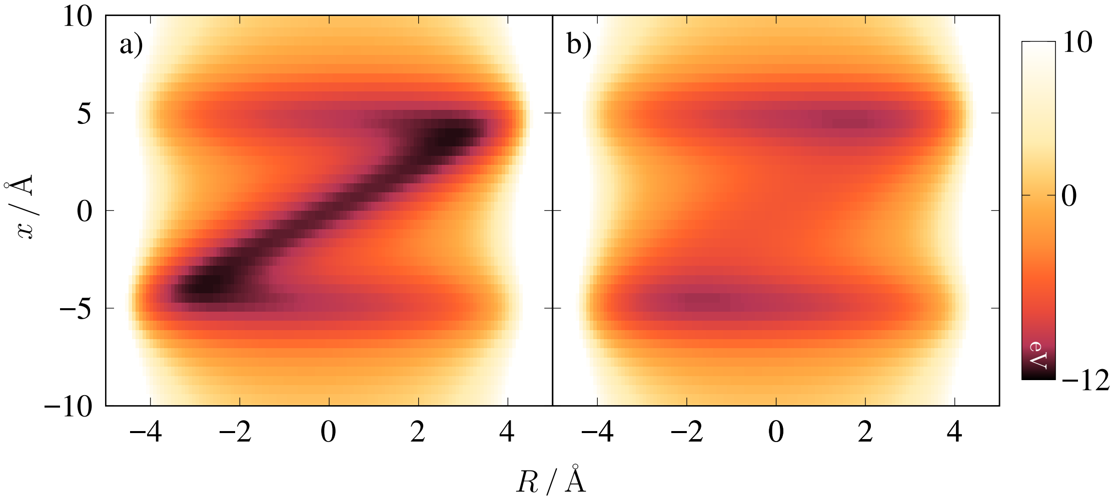

Figure 2.2. Potential $V(x,R)$ for the single-electron Shin-Metiu model. Nuclear charges chosen homogeneously as $Z = Z_1 = Z_2 = 1$ elementary charges with truncation parameters $R_\mathrm{f} = 1.5\,\text{Å}$, $R_\mathrm{c} = 1.5\,\text{Å}$ (a) and $R_\mathrm{c} = 2.5\,\text{Å}$ (b). The outer nuclei are positioned at $\pm L/2 = \pm 5\,\text{Å}$.

2.1.2 Error-function

As seen in the last section, the truncation parameters R_f and R_c can be used to change the system's behaviour. While Sec. 2.1.3 will show the ensuing influence of the parameters on the system's potential energy surfaces $V_n^{1\mathrm{e}}(R)$, the error function as well as their terms in the potential $V(x,R)$, Eq. (2.1), are described here.

Fig. 2.3a depicts $\operatorname{erf}(|x|/R_\mathrm{c})$ for a change in the coupling constant of the electron and the mobile nucleus. For $R_\mathrm{c} = 1.5\,\text{Å}$ the pure error function takes values between (0,1), where the minimum is approached for the limes of $|x| \longrightarrow 0$ and the maximum for $|x| \longrightarrow \infty$.

Switching to the larger value, $R_\mathrm{c} = 2.5\,\text{Å}$, these properties are retained, however, the function's width has increased, meaning that both values are approached slower.

Turning to the full term, $-Z\operatorname{erf}(|R-x|/R_\mathrm{c})/|R-x|$, the full picture is revealed (cf. Fig. 2.3b): The smaller the truncation parameter R_c, the larger the contribution of the full coupling term to the overall potential is, or in other words, the larger R_c, the more shrouded the electron is from the mobile nucleus' pull.

2.1.3 Potential Energy Surfaces for Weak and Strong Coupling

The system's potential energy surfaces (PES) $V_n^{1\mathrm{e}}(R)$ describing the potential energy for a given electronic state n and a nuclear position of R are retrieved

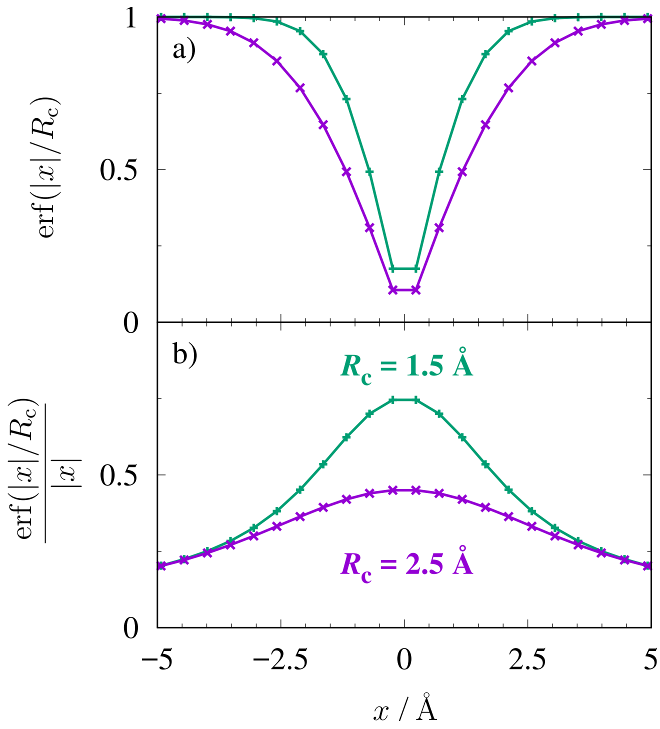

Figure 2.3. a) Error function, $\mathrm{erf}(|x|/R_\mathrm{c})$, and b) full coupling term, $\mathrm{erf}(|x|/R_\mathrm{c})/|x|$, for different values of the truncation parameter, R_c, describing the coupling between the system's electron and mobile nucleus.

from the eigenvalue problem

$$\hat{\mathcal{H}}_\mathrm{el}\psi_n(x;R) = V_n^\mathrm{1e}(R)\,\psi_n(x;R), \tag{2.2}$$

where R acts as a parametric variable and $V_n^\mathrm{1e}(R)$ is the corresponding eigenvalue/-energy. Numerically, the PES is calculated alongside the electronic eigenfunctions $\psi_n(x;R)$ via imaginary-time propagation (Chapter 1.1.4). Within the Born-Oppenheimer approximation (BOA), Chapter 1.2, these curves are utilized for propagation assuming instantaneous electron reorganization after changes of the nuclear position. While the accuracy of the dynamics described by the BOA depends on any given system, the potential energy surfaces illustrate nuclear dynamics in general quite well.

Fig. 2.4a shows $V_n^\mathrm{1e}(R)$ for the four lowest electronic states n for a configuration with parameters $R_\mathrm{f} = R_\mathrm{c} = 1.5\,\text{Å}$. Note in particular, the double-well structure for the electronic ground state, as well as the separation of at least 1.28 eV from the next higher electronic state, $n = 1$. In general, the closer two electronic states are energetically, the more likely population transfer between these states, if they are coupled. Consequently, the case of $R_\mathrm{f} = R_\mathrm{c} = 1.5\,\text{Å}$ with a rather big energy gap is coined "weak coupling" case [71].

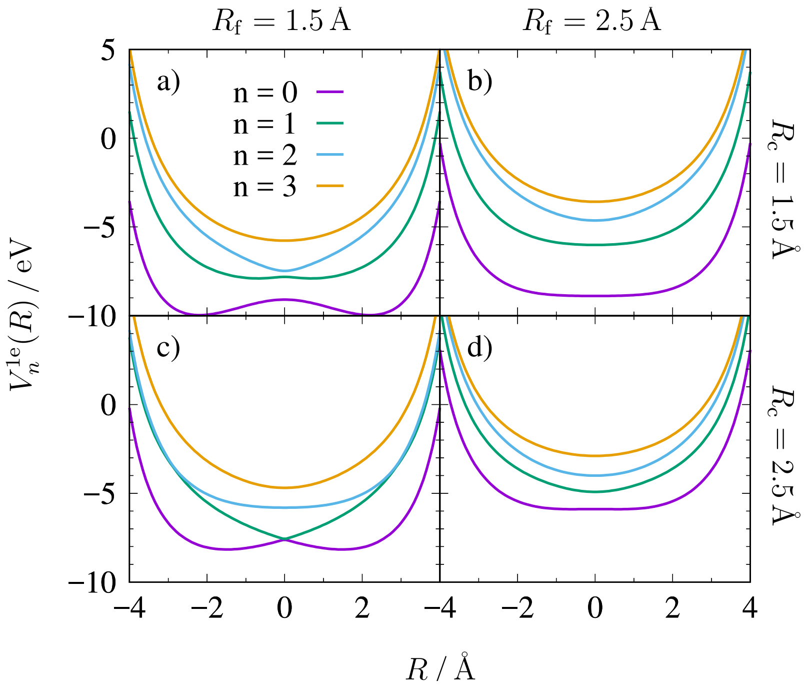

Figure 2.4. Potential energy surfaces $V_n^{1\mathrm{e}}(R)$ for the single-electron Shin-Metiu model. Coupling parameters R_f and R_c are as indicated. Chapter 3 will study the weak and strong coupling cases for the interaction between the electron and the mobile nucleus, a) and c).

The "strong coupling" case, on the other hand, is displayed in Fig. 2.4c, where the truncation parameter R_c has been set to $2.5\,\mathrm{Å}$[2]. While the double-well structure is retained for the electronic ground state, at the nuclear center position of $R = 0\,\mathrm{Å}$ the potential energy surfaces of two lowest states are merely separated by 0.05 eV making non-adiabatic transitions highly likely.

The influence of R_f corresponding to the coupling of the electron and each of the two fixed outer nuclei is shown in Fig. 2.4b and d. Here, the electronic states remain well separated for various R_c values, while at the same time the double-well structure is lost.

For the purpose of the research presented in this work, the investigation will focus on the weak and strong coupling cases (Fig. 2.4a and c).

Fig. 2.5 shows the adiabatic electronic ground state $\varphi_0(x; R)$ for the two coupling cases. While electronic density adiabatically adjusts to a change in nuclear position for the weak coupling case (a), the density remains mostly stationary for the strong coupling case (b) until the molecular center at $R = 0\,\mathrm{Å}$ is passed. There, the ground state abruptly has to have a density distribution on

---

[2] Note that the nomenclature of the "weak" and "strong" case corresponds to the non-adiabatic transition occurring. The potential energy terms are actually larger for the "weak" case, and smaller for the "strong" case.

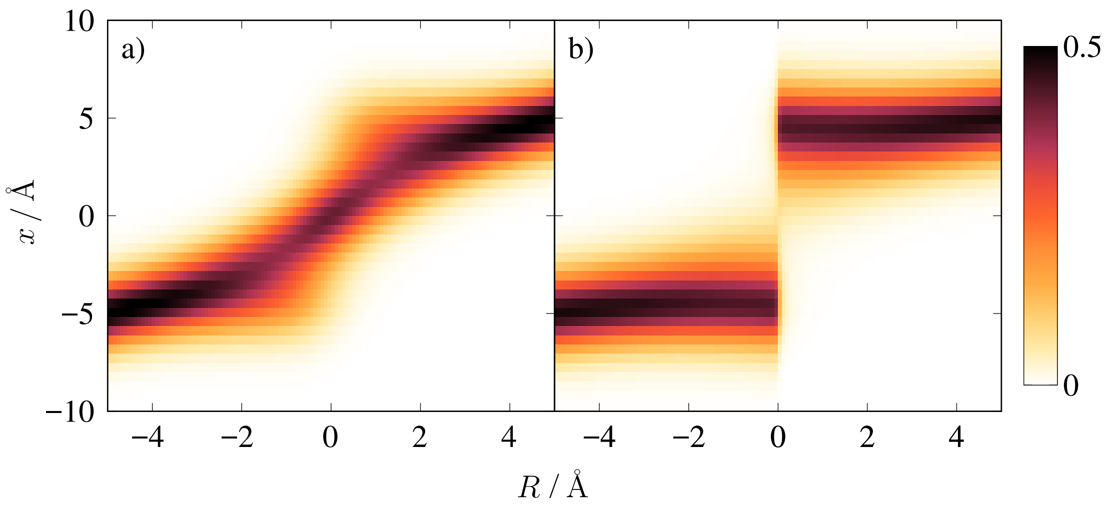

Figure 2.5. Electronic ground states $\varphi_0(x;R)$ for a) $R_\mathrm{c} = 1.5\,\text{Å}$ and b) $R_\mathrm{c} = 2.5\,\text{Å}$. While the electronic wave function adjust adiabatically to a change in nuclear geometry for the weak coupling case (a), the strong coupling case exhibits an avoided crossing at $R = 0\,\text{Å}$.

the molecule's other side. Dynamics involving the avoided crossing at $R = 0\,\text{Å}$ thus exhibit a population transfer from the electronic ground state, $n = 0$, to the first excited state, $n = 1$, which has its localization of electronic density as the ground state, however, for the new nuclear orientation (not shown here).

2.2 Two-electron Version

The natural extension to the original Shin-Metiu model consists of the addition of a second electron as has been done first by the group of Engel [68]. This new degree of freedom, which is typically described by the coordinate y or x_2, introduces electron correlations to the system, i.e. Coulomb repulsion (Sec. 2.2.1) and spin dynamics, if accounted for a spin-coupling mechanism (Sec. 2.2.2). Fig. 2.6 displays the particle configuration of the extended system.

2.2.1 Potential

The potential of the two-electron Shin-Metiu model, $V(x,y,R)$, comprises of the one-electron potential, $V(x,R)$, extended by a second set of Coulomb attraction terms for coupling of the new electron with the existing nuclei, as well as a new term describing the Coulomb repulsion between the two electrons.

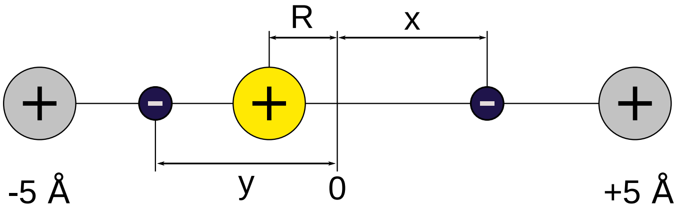

Figure 2.6. Particle configuration of the extended Shin-Metiu model, where another electron, described by coordinate y, is added.

Coordinate y corresponds to the new electronic degree of freedom:

$$\begin{aligned} V(x,y,R) = {} & \frac{Z_1 Z}{|L/2-R|} + \frac{Z_2 Z}{|L/2+R|} + \frac{\operatorname{erf}(|x-y|/R_e)}{|x-y|} \\ & - \frac{Z_1 \operatorname{erf}(|L/2-x|/R_f)}{|L/2-x|} - \frac{Z_2 \operatorname{erf}(|L/2+x|/R_f)}{|L/2+x|} \\ & - \frac{Z_1 \operatorname{erf}(|L/2-y|/R_f)}{|L/2-y|} - \frac{Z_2 \operatorname{erf}(|L/2+y|/R_f)}{|L/2+y|} \\ & - \frac{Z \operatorname{erf}(|R-x|/R_c)}{|R-x|} - \frac{Z \operatorname{erf}(|R-y|/R_c)}{|R-y|}. \end{aligned} \tag{2.3}$$

Like before, the Coulomb interaction is for numerical reasons implemented via the error function. The truncation parameter further describing the electronic repulsion is denoted as R_e.

Fig. 2.7 shows the potential $V(x,y,R_0)$ for the nuclear configuration of $R_0 = -2.05$ Å, which corresponds to the left minimum of the potential energy surface $V_0^{2\mathrm{e}}(R)$ (see Sec. 2.2.3). It is this configuration which will be used to initialize the system's dynamics during the investigations presented in Chapter 4.

The potential's minima are symmetric around the $x = y$-diagonal and are located such that the most likely electronic distribution corresponds to one electron sitting between the two left nuclei, while the other resides close to the right-hand side nucleus. Other minima with slightly less binding energy are found for both electrons located on the left-hand side with one electron at each nucleus from that side.

2.2.2 Spin-Implementation

If the electronic spin does not change over time, i.e. no spin-coupling, for example, in the shape of a magnetic field, occurs, it suffices to choose the spin when setting up the system' initial state. A simple solution can be employed for a two-electron wave function:

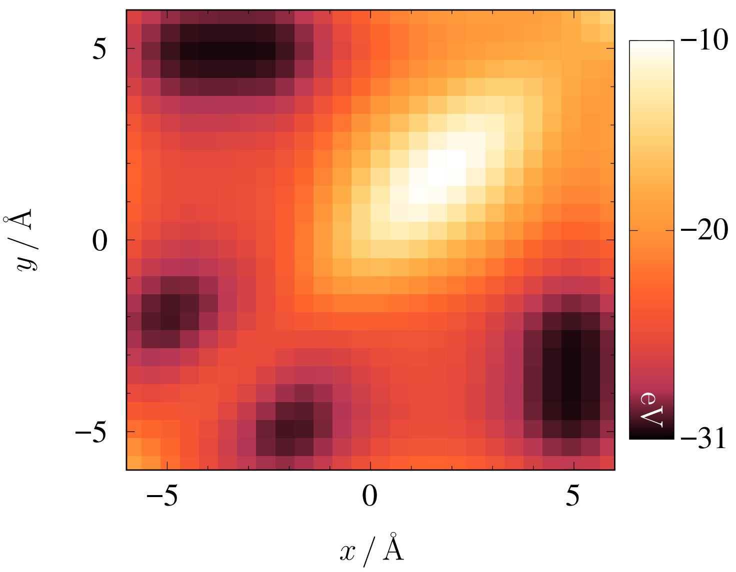

Figure 2.7. Potential $V(x, y, R_0 = -2.05\,\text{Å})$ for the two-electron Shin-Metiu model. Nuclear charges are chosen homogeneously as $Z = Z_1 = Z_2 = 1$ with truncation parameters $R_\text{f} = R_\text{c} = R_\text{e} = 1.5\,\text{Å}$. The outer nuclei are positioned at $\pm L/2 = \pm 5\,\text{Å}$. The nuclear configuration corresponds to a minimum of the potential energy surface $V_n^{2\text{e}}(R)$ in the electronic ground state ($n = 0$).

As the total wave function of a fermionic system has to be antisymmetric, the spin configuration can be enforced to be symmetric (parallel spins) or anti-symmetric (anti-parallel spins) by forcing the spatial wave function to be anti-symmetric or symmetric, respectively. This is done during the imaginary-time propagation (ITP), introduced in Chapter 1.1.4.

While the "natural" symmetry of the spatial wave function during the ITP depends on the chosen initial wave function, symmetry can be enforced manually. For this the spatial wave function is built symmetric (+1) or antisymmetric (-1) after each iteration step by separating the wave function along the $x = y$-diagonal and defining the other half as

$$\varphi_n(x, y; R)|_{x>y} := \pm 1 \cdot \varphi_n(x, y; R)|_{x<y}. \tag{2.4}$$

Fig. 2.8 shows the spatial wave function for an antisymmetric spatial, hence symmetric spin configuration (a, triplet state), and for a symmetric spatial and thus antisymmetric spin configuration (b, singlet state). Here, the illustration corresponds to the electronic ground state at the aforementioned potential minimum.

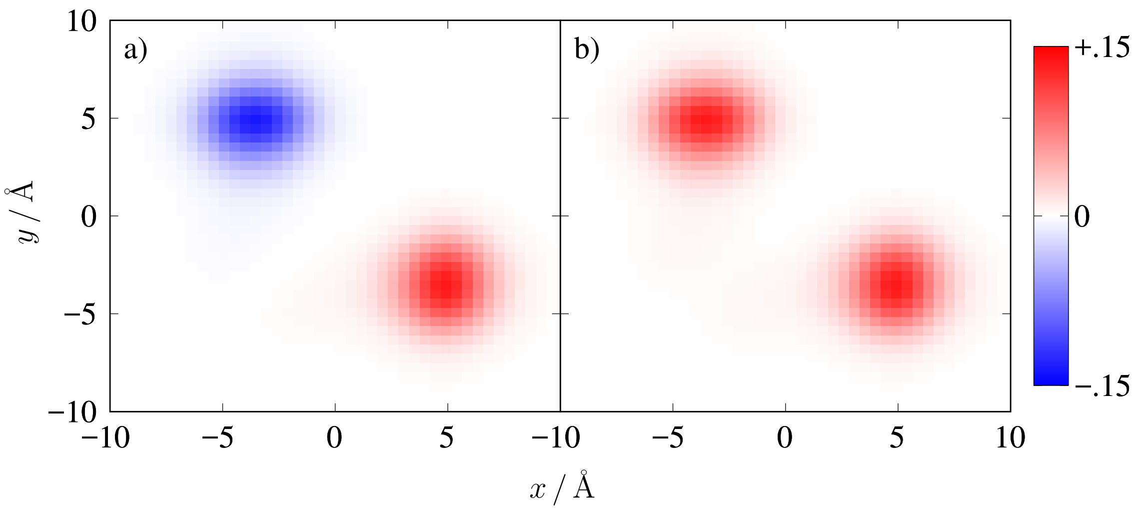

Figure 2.8. Spatial wave function $\varphi_0(x, y; R_0)$ for parallel (a) and anti-parallel spins (b). The nuclear position represents the left-hand side's potential minimum at $R_0 = -2.05\,\text{Å}$.

2.2.3 Potential Energy Surfaces for Various Configurations

The potential energy surfaces (PES) $V_n^{2e}(R)$ of the two-electron system are calculated like their one-electron counterpart in Sec. 2.1.3, with the difference of additionally considering spin property as introduced in the last section. Fig. 2.9 shows the various parameter configurations of R_c and R_e, while keeping $R_f = 1.5\,\text{Å}$ as a constant. The solid (dotted) lines correspond to anti-parallel (parallel) spins.

As can be seen in all but panel e, the electronic ground state is nearly degenerate for $R_c \geq R_e$, but separates in energy for $R_c < R_e$. Most interestingly, a switch from anti-parallel to parallel spins can lead to electronic states, whose PES is comprised of two different curves from the anti-parallel configuration. For example in Fig. 2.9e, the second excited state of the parallel spin system (dotted line) has an energy curve of the $n = 3$ state of the anti-parallel configuration (solid line) for nuclear coordinates $|R| > 1.8\,\text{Å}$, and a curve of the $n = 2$ state otherwise.

Chapter 4 will focus on the parameter choice of $R_c = R_e = 1.5\,\text{Å}$ with an anti-parallel spin configuration, Fig. 2.9c (solid lines). There, a wave packet located in the vibrational minimum of the electronic ground state (left-hand side, $R_0 = -2.05\,\text{Å}$) will initiate the dynamics.

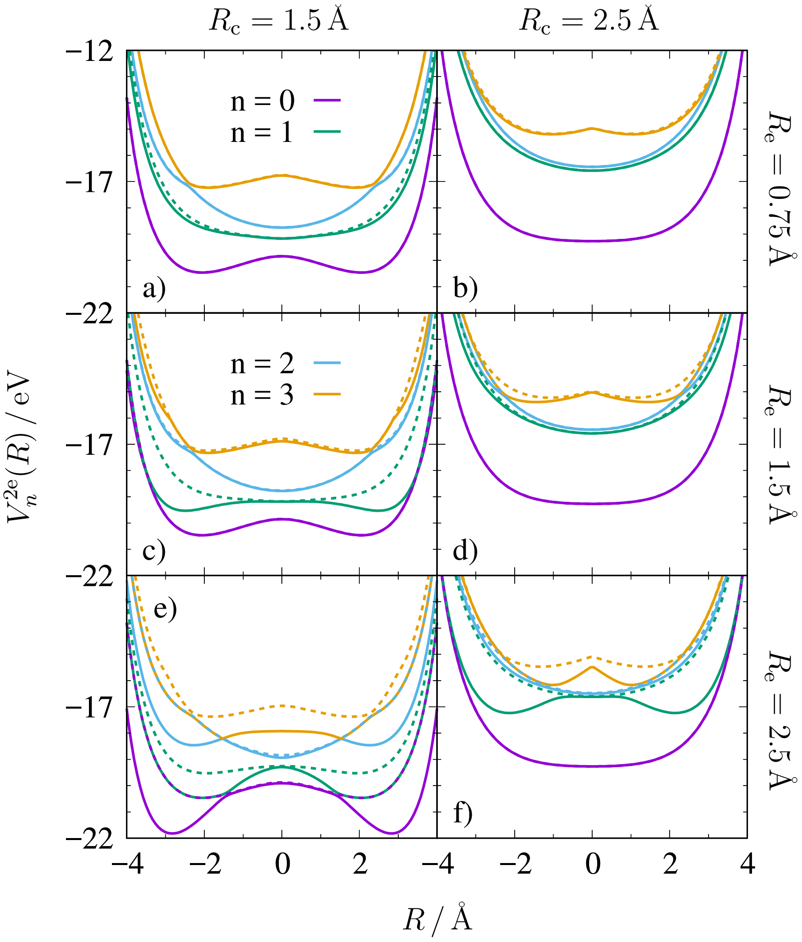

Figure 2.9. Potential energy surfaces $V_n^{2\mathrm{e}}(R)$ for the two-electron Shin-Metiu model. Coupling parameters R_c and R_e are as indicated. Solid (dotted) lines correspond to an anti-parallel (parallel) spin configuration. Chapter 4 will study the configuration from panel c in detail.

CHAPTER

Time-resolved Photoelectron Spectroscopy of IR-driven Electron Dynamics

3

Spectroscopy, as the study of light-matter interaction, has become one of the primary tools for investigating atomic and molecular systems, both in stable but also transient states. To resolve electronic dynamics, which are vital to any chemical reaction, ultra-short laser pulses on the attosecond time-scale are required [102]. As the probing pulses get temporally shorter, their central wavelengths have to become smaller as well, leading to operation in the extreme ultraviolet (XUV). Typically, these XUV measurements employ a second electromagnetic field from the near-infrared (NIR), which acts as a time ruler for the attosecond resolution of the probing (XUV) pulse [103–106]. However, even weak fields induce electron dynamics, which can overshadow the system's intrinsic dynamics, i.e. dynamics that occurs in the absence of external fields. [107–109]. The question arises, whether experiments employing an XUV+NIR excitation scheme allow to make genuine statements about the dynamics of unperturbed systems.

In molecules, intrinsic electronic motion is highly correlated with nuclear motion due to the strong Coulomb-interaction of charged particles. Two "limiting cases" can be distinguished [110]: In one case, electrons follow the nuclear motion adiabatically. That means that upon a change in the nuclear geometry, the electronic density adapts approximately instantaneously. In the other case, the electronic density is only weakly influenced by a geometry change and a diabatic motion arises. In terms of adiabatic electronic eigenstates, the diabatic case is characterized by strong non-adiabatic couplings, which manifest themselves in neighbouring potential energy surfaces approaching each other. Such diabatic motion then results in a population transfer between the two adiabatic states. In numerical simulations, asymmetries in time-resolved photoelectron spectra can serve as a tool to distinguish the two cases [66]. Extensive studies from the past years provide good experimental [111–121] and theoretical [122–126] understanding, even though a fully quantum mechanical description of correlated electron-nuclear dynamics remains challenging. This stems from the task of solving the time-dependent Schrödinger equation for the coupled motion of several particles, each with several degrees of freedom (DOF). Currently the biggest systems solved employ the **M**ulti-**C**onfiguration **T**ime-**D**ependent **H**artree theory (short: MCTDH) and cover up to 24 degrees of freedom, but require a factorization of the individual DOF [127]. Using a multi-layer MCTDH variant, it is even possible to treat systems with thousands of DOF [128]. However, due to the requirement of factorization, systems, where factorization is not possible[1], cannot be be described accurately. To answer specific questions about the coupled electron-nuclear motion in the presence of external NIR fields, it is thus necessary to choose reasonable models. One such model is the Shin-Metiu model [97, 98], introduced in Chapter 2.

Its low dimensionality, the main advantage of the Shin-Metiu model is its versatile adaptation for adiabatic and diabatic configurations by means of a parameter switch. Many such configurations have been used to mimic different types of coupled electronic and nuclear dynamics and to simulate spectroscopic observables [63, 64, 66, 67, 69–71, 129–132].

In this chapter, the focus lies on an accurate description of a photoelectron angular distribution (PAD) for coupled electronic nuclear degrees of freedom as it can be realized by the linear Shin-Metiu model: In this linear configuration, the emission of a photoelectron during ionization shows a forward/backward preference reflecting the electronic dynamics prior to the interaction with the ionizing pulse. By introduction of an IR pulse, which precedes an XUV pulse, the possibility of enhancing weak photoelectron signals stemming from intrinsic dynamics is investigated. This chapter is based on Ref. [133].

The chapter is organized as follows: In Section 3.1 the model's implementation and the computation of the photoelectron asymmetries are described. Numerical results for an adiabatic (Sec. 3.2) and a diabatic setting (Sec. 3.3) are given, together with section 3.4 investigating superpositions of electronic states. A discussion concludes the chapter (Sec. 3.5).

3.1 Model Setup

For investigating the coupled dynamics of electrons and nuclei, the single-electron version of the Shin-Metiu model [97, 98] as introduced in Chapter 2.1 is employed. Here, the fixed nuclei are positioned at $\pm 5\,\text{Å}$. The truncation parameter describing the Coulomb-interaction between nuclei is chosen as constant $R_\mathrm{f} = 1.5\,\text{Å}$, while the one for electron-nuclei interaction, R_c, is modified

---

[1] e.g. Coulomb interaction terms cannot be factorized

for strong and weak coupling. Weak coupling, resulting in a setting dominated by adiabatic dynamics, is realized by choosing $R_\mathrm{c} = 1.5\,\text{Å}$, whereas $R_\mathrm{c} = 2.5\,\text{Å}$ leads to non-adiabatic coupling and mostly diabatic dynamics. The potential energy curves are calculated via imaginary time-propagation [82] (see Fig. 2.4, p. 35).

Numerical representation spans a two-dimensional grid for the moving electronic (x) and nuclear (R) coordinate, respectively. The electronic grid covers a range of $x \in [-240, 240]\,\text{Å}$ with a resolution of $N_x = 1024$ points, resulting in a spacing of $\mathrm{d}x = 0.47\,\text{Å}$. The nuclear grid is restricted to the range of $R \in [-6, 6]\,\text{Å}$ as the mobile nucleus is securely confined by the fixed, outer nuclei. The nuclear resolution is $N_R = 256$ points with a spacing of $\mathrm{d}R = 0.047\,\text{Å}$. These spatial grids correspond to momentum grids of $p_x \in [-3.54, 3.54]$ atomic units (a.u.) for the electronic momentum with spacing $\mathrm{d}p_x = 6.9 \times 10^{-3}$ a.u., and nuclear momentum in the range of $P_R \in [-35.5, 35.2]$ a.u. with spacing $\mathrm{d}p_R = 0.28$ a.u.. As the electron's mass is low, it moves fast, and lower spatial, but higher momentum resolution is required for an accurate description. The opposite is true for the mobile nucleus.

Table 3.1. Simulation parameters for the 1e-Shin-Metiu system.

Parameter	**Number of Points**	
N_R	256	
N_x	1024	
	Value	
$\mathrm{d}t$	1 as	
R_f	1.5 Å	
R_c	1.5 Å (weak) & 2.5 Å (strong)	
	Range / Å	**Spacing / Å**
R	$[-6, 6]$	0.047
x	$[-240, 240]$	0.47
	Range / a.u.	**Spacing / a.u.**
P_R	$[-35.5, 35.2]$	0.28
p_x	$[-3.54, 3.54]$	6.9×10^{-3}

For propagation the time-dependent Schrödinger equation (1.1) is solved numerically by usage of the split-operator technique, Sec. 1.1.3, and the FFTW 3 library [96]. The Hamiltonian is applied in velocity gauge, Eq. (1.69), with potential $\hat{V}$ from Eq. (2.1) and fields as described in the following section. The employed time step is set to $\Delta t = 1$ as.

In order to avoid reflections at the end of the electronic grid, it is partioned

Table 3.2. XUV and IR pulse parameters. The values in bold notation are employed, if not explicitly stated otherwise.

Parameter	**IR**	**XUV**		
E_0 / W cm^{-2}	$\{0.25, \mathbf{1}, 4\} \times 10^{11}$	1×10^{13}		
λ / nm	1200	**60**	75	90
λ / eV	1.03	**20.7**	16.5	13.8
τ / fs	14.7	**2.30**	1.21	0.24
σ / eV	0.12	**0.79**	3.42	17.2
T / fs	24	scanned in $\mathrm{d}t = 0.1\,\mathrm{fs}$ increments		

into an inner and outer, asymptotic region via an absorbing cut-off function, as described in Chapter 1.3.3.

3.1.1 Pump- & Probe-fields

For probing an ionizing ultrashort XUV-field is employed, while for pumping an IR-field is used. The pulses' electric fields read:

$$E_{\mathrm{XUV}}(t) = E_{0,\mathrm{XUV}}\, f_{\mathrm{XUV}}(t-T)\, \cos\left[\omega_{\mathrm{XUV}}(t-T)\right], \tag{3.1}$$

$$E_{\mathrm{IR}}(t) = E_{0,\mathrm{IR}}\, f_{\mathrm{IR}}(t-T_{\mathrm{IR}})\, \cos\left[\omega_{\mathrm{IR}}(t-T_{\mathrm{IR}}) + \phi_{\mathrm{IR}}\right]. \tag{3.2}$$

Here, $E_{0,i}$ is the field strength, $f_i(t-T)$ a Gaussian pulse envelope function centered around time T_i, while ω_i is the pulses central frequency and $\phi_{\mathrm{IR}} \in \{0, \pi\}$ the carrier-envelope phase (CEP) of the IR-field. To avoid confusion with the photoelectron asymmetry induced by the IR-field, A_{IR}, the notation in terms of the electric field was used here.

For the probing pulse the central frequency corresponds to a wavelength of $\lambda_{\mathrm{XUV}} = 60\,\mathrm{nm}$ (20.7 eV) if not indicated otherwise. Its temporal full width at half maximum (FWHM) is set to $\tau_{\mathrm{XUV}} = 2.32\,\mathrm{fs}$ (corresponding to a spectral FWHM of $\sigma_{\mathrm{XUV}} = 0.79\,\mathrm{eV}$), while the temporal center T is variable and the field strength set as $E_{0,\mathrm{XUV}} = 1 \times 10^{13}\,\mathrm{W\,cm^{-2}}$.

The central frequency of the IR-field corresponds to $\lambda_{\mathrm{IR}} = 1200\,\mathrm{nm}$ (1.0 eV) with $\tau_{\mathrm{IR}} = 14.7\,\mathrm{fs}$ ($\sigma_{\mathrm{IR}} = 0.12\,\mathrm{eV}$) and is centered around $T_{\mathrm{IR}} = 24\,\mathrm{fs}$. Its field strength and CEP are set to $E_{0,\mathrm{IR}} = 1 \times 10^{11}\,\mathrm{W\,cm^{-2}}$ and $\phi_{\mathrm{IR}} = 0$ if not mentioned otherwise.

Fig. 3.1 shows the XUV- and IR-pulses next to each other, while Table 3.2 summarizes the pulse parameters.

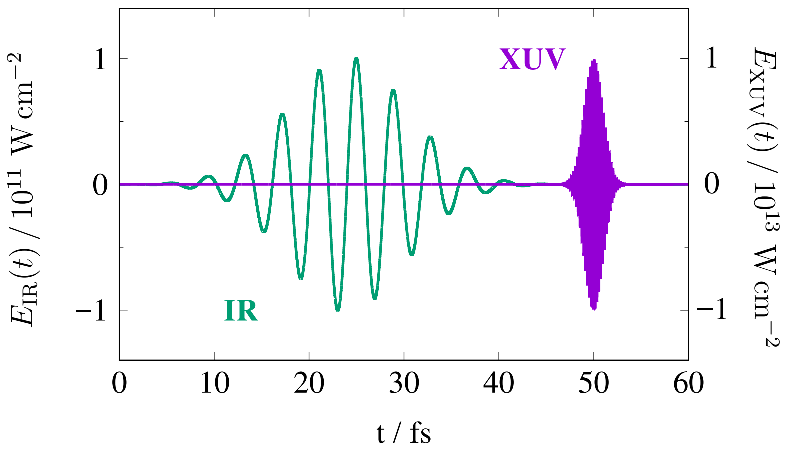

Figure 3.1. Pump- & probe-pulses as used during the calculations. The IR-field remains fixed at $T_{\mathrm{IR}} = 24\,\mathrm{fs}$, while the XUV-field "scans" the system for different times T, here $T = 50\,\mathrm{fs}$.

3.1.2 Photoelectron Spectrum

The photoelectron spectrum is calculated from the ionized part of the propagated wave function, ψ_{out}, following section 1.3.3, p. 23.

For times long after the ionizing XUV-pulse at time T, i.e. $t \to \infty$, the photoelectron spectrum is calculated as

$$\sigma(p_x, T) = \int \left|\psi_{\mathrm{out}}(p_x, R, T, t \to \infty)\right|^2 \mathrm{d}R. \tag{3.3}$$

When the norms of the inner and outer regions become stationary, the time convergence, $t \to \infty$, is assumed to be reached. For the employed system, this is the case for 20 fs after the XUV-pulse is gone.

An example of the photoelectron spectrum for a single ionization time T can be seen in Fig. 3.2. Here, the spectrum is expressed in terms of the electron's kinetic energy, $E_{\mathrm{kin}} = p_x^2/2m_e$, with solid (dotted) lines indicating the direction of emission. Note, that the distributions for *forward* and *backward* direction are very similar. This is true for most ionization times T, however, subtle differences can be revealed by inspection of the asymmetry, which is defined in the next section.

3.1.3 Resolved and Integrated Spectral Asymmetry

After measuring the photoelectron angular distribution (PAD) in an experiment, or calculating it in a simulation, the momentum-resolved asymmetry can be introduced. For the case of the linear Shin-Metiu model the PAD consists of only two possible directions of emission: forward and backward. Consequently, the photoelectron momentum distribution $\sigma(p_x, T)$ from Eq. (3.3) can be split

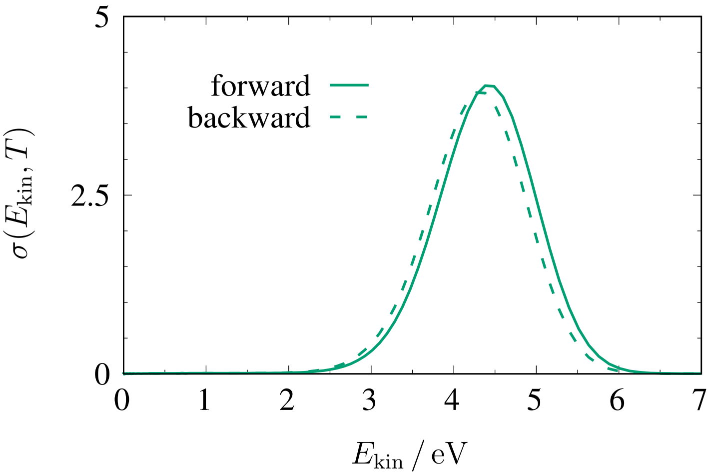

Figure 3.2. Sample photoelectron spectrum $\sigma(E_{\mathrm{kin}}, T)$ for a specific ionization time T. The solid (dotted) line corresponds to emission with positive (negative) momenta, i.e. in forward (backward) direction.

into parts with exclusively positive, σ^+ ($p_x > 0$), and negative momenta, σ^i ($p_x < 0$), respectively. The momentum resolved asymmetry is then calculated as

$$A(p_x, T) = \frac{\sigma^+(p_x, T) - \sigma^-(p_x, T)}{\sigma^+(p_x, T) + \sigma^-(p_x, T) + \epsilon}, \tag{3.4}$$

where $\epsilon = 10^{-10}$ is added to the denominator to avoid numerical instabilities. The integrated spectra,

$$\sigma^+(T) = \int_0^\infty \sigma(p_x, T)\,\mathrm{d}p_x, \tag{3.5}$$

$$\sigma^-(T) = \int_{-\infty}^0 \sigma(p_x, T)\,\mathrm{d}p_x, \tag{3.6}$$

where integration is limited to either positive (+) or negative (-) momenta, allow to define an integrated asymmetry as

$$A(T) = \frac{\sigma^+(T) - \sigma^-(T)}{\sigma^+(T) + \sigma^-(T) + \epsilon}. \tag{3.7}$$

Previous works by Falge, Engel & Gräfe [66] have shown that the integrated asymmetry carries information about the intrinsic electron dynamics in adiabatic and diabatic settings. Starting in Sec. 3.2, the integrated asymmetry will be used to investigate IR-driven electron dynamics and answer the question, whether intrinsic dynamics prior to the ionization is still reflected in the photoelectron angular distribution.

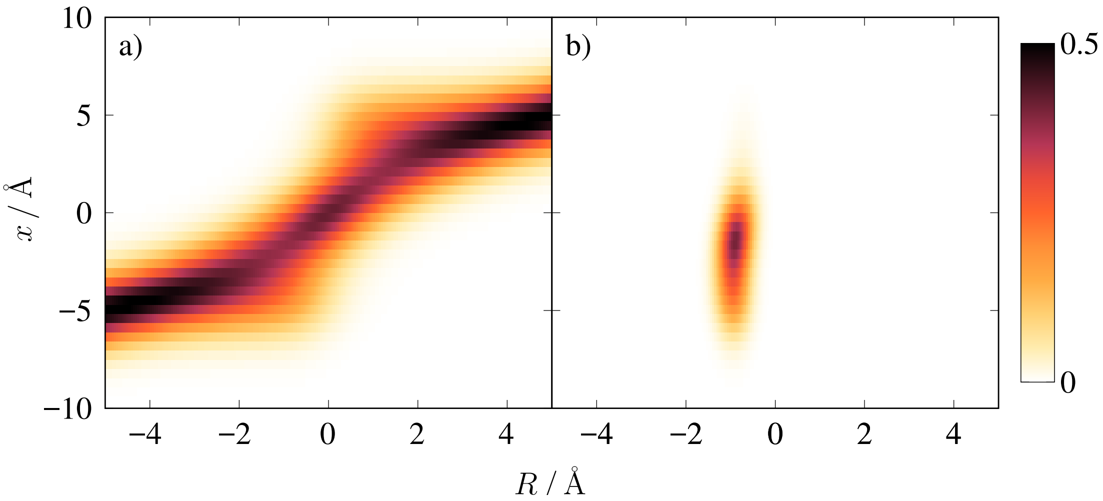

Figure 3.3. System initialization for the adiabatic case ($R_\mathrm{c} = 1.5\,\text{Å}$). a) Electronic ground state $\varphi_0(x; R)$. b) Initial wave packet setup as a vibrational wave packet in the electronic ground state.

3.1.4 System Initialization

Non-equilibrium initial conditions are chosen for the nuclear degree of freedom inducing a coherent wave packet dynamics that mimics common situations as encountered, for example, upon photoionization. To this end, a vibrational wave packet is placed at R_0 in the electronic ground state ($n = 0$) outside of its energetic minimum. In the adiabatic case ($R_\mathrm{c} = 1.5\,\text{Å}$), it is centered around $R_0 = -0.9\,\text{Å}$, initiating a dynamics initially towards negative coordinates and ensuring a dynamics confined to the left potential well. In the diabatic case ($R_\mathrm{c} = 2.5\,\text{Å}$), the vibrational wave packet is centered at $R_0 = -3.0\,\text{Å}$ so that a dynamics is initiated towards positive coordinates with a possible crossing to the first excited electronic state ($n = 1$) at $R = 0\,\text{Å}$, where non-adiabatic transitions will occur. The vibrational wave packets' widths are given by $\beta_\mathrm{R} = 7.14\,\text{Å}^{-2}$, respectively, so that the initial wave functions read

$$\psi(x, R, t = 0) = N_0\, \mathrm{e}^{-\beta_\mathrm{R}(R-R_0)^2}\, \varphi_0(x; R). \tag{3.8}$$

Here, N_0 serves as a normalization constant, and φ_0 is the electronic ground state calculated via imaginary time propagation (see Chapter 1.1.4). The adiabatic electronic ground state, φ_0, can be seen exemplarily for the adiabatic case ($R_\mathrm{c} = 1.5\,\text{Å}$) in Fig. 3.3a with Fig. 3.3b showing the initial wave packet $\psi(x, R, t = 0)$.

3.2 Dynamics in an Adiabatic Setting

3.2.1 Intrinsic Dynamics

By choosing the truncation parameter of the electron-nuclear coupling as $R_c = 1.5\,\text{Å}$, a system behaving predominately adiabatically is realized. Here, the *intrinsic* dynamics describes the case, when the driving field is absent. The integrated asymmetry for this IR-free case is denoted by $A_0(T)$. With a vibrational wave packet initially centered at $R_0 = -0.9\,\text{Å}$, dynamics within the left potential well are initiated and the electronic wave function adiabatically follows the nuclear motion. The potential energy surface from Fig. 2.4a can be used as an intuitive picture. Note, however, that in the picture of the Born-Oppenheimer approximation, Chapter 1.2, the electron is assumed to instantaneously adapt to a varying nuclear geometry, neglecting non-adiabatic coupling of the kind $\langle\varphi_n|\frac{\partial}{\partial R}|\varphi_{m\neq n}\rangle$ and $\left\langle\varphi_n\middle|\frac{\partial^2}{\partial R^2}\middle|\varphi_{m\neq n}\right\rangle$.

When propagating with the full time-dependent Schrödinger equation, both the mobile nucleus and the electron are accelerated towards negative coordinates, as seen in Fig. 3.4a+b. The momentum expectation value of both particles is calculated as

$$\langle p_\text{x}\rangle(t) = \iint p_\text{x} \cdot |\psi(p_\text{x}, R, t)|^2 \,\text{d}p_\text{x}\,\text{d}R, \tag{3.9}$$

$$\langle P_\text{R}\rangle(t) = \iint P_\text{R} \cdot |\psi(x, P_\text{R}, t)|^2 \,\text{d}x\,\text{d}P_\text{R}. \tag{3.10}$$

After approximately 20 fs, the mobile nucleus passes through the potential minimum and exhibits its maximum momentum. At around 35 fs, the turning point is reached, indicated by $\langle p_\text{x}\rangle \approx \langle P_\text{R}\rangle \approx 0$ a.u.. From here, the oscillatory movement continues with the electron adiabatically following the nucleus.

It should be noted that $\langle p_\text{x}\rangle$ exhibits fast oscillations when close to $R = 0\,\text{Å}$, which are not present for the mobile nucleus. Even though the potential energy curves of the electronic ground ($n = 0$) and first excited state ($n = 1$) are separated by 1.28 eV at this position, tiny portions of the wave function are transferred to the higher state. The coupling between these states is responsible for the fast oscillations. Chapter 3.4 will go into more detail on oscillations induced by propagation of superposition states.

In Fig. 3.4c the integrated, IR-free asymmetry $A_0(T)$ is depicted. As can be seen, its shape represents that of the electron's momentum expectation value. Within a classical, intuitive picture this is explained as follows: Upon ionization by the ultrashort XUV-pulse, the electron is nearly instantaneously yanked from its bound state and thus retains its average momentum. Consequently, it is emitted preferentially towards the direction it moved at the instant of ionization, hence creating a time-dependence within the asymmetry of the

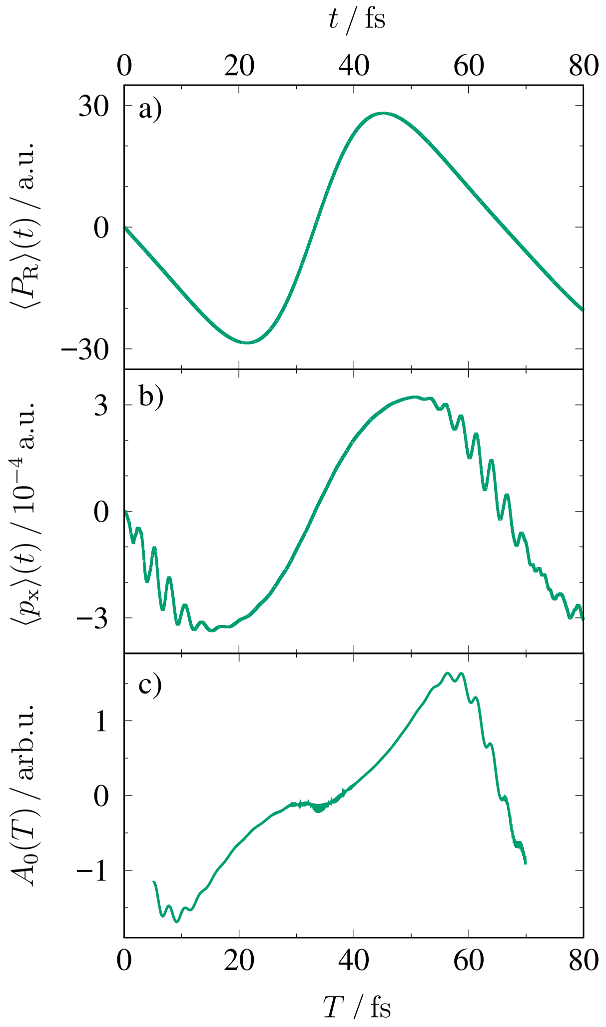

Figure 3.4. Intrinsic dynamics in the adiabatic setting ($R_{\mathrm{c}} = 1.5\,\text{Å}$). a+b) Momentum expectation value of the electron and mobile nucleus calculated via Eqs. (3.9) and (3.10), respectively. c) Integrated asymmetry $A_0(T)$.

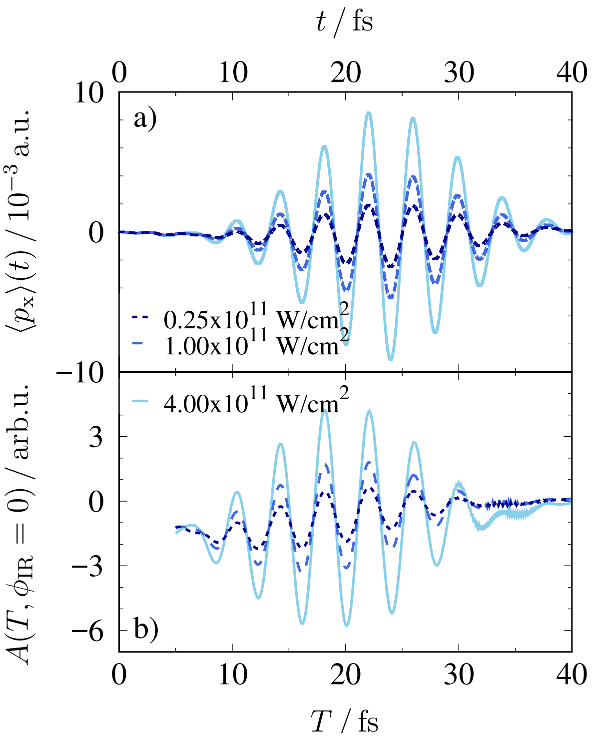

Figure 3.5. Driven dynamics in the adiabatic setting ($R_\mathrm{c} = 1.5\,\mathrm{Å}$). a) Momentum expectation value for the electron at different intensities of the driving IR-field. b) Integrated asymmetry for a driving field with fixed CEP, ϕ_IR.

photoelectron momentum distribution.

3.2.2 Driven Dynamics

To investigate how the adiabatic system behaves when driven by an external field, a moderately intense IR-laser field with $\lambda_\mathrm{IR} = 1200\,\mathrm{nm}$, $\tau_\mathrm{IR} = 14.7\,\mathrm{fs}$, field strengths $E_{0,\mathrm{IR}} \in \{0.25, 1, 4\} \times 10^{11}$ W cm^{-2}, centered around $T_\mathrm{IR} = 24\,\mathrm{fs}$, is applied. The vector potential of the IR-field accelerates the bound electron in addition to its intrinsic dynamics. As can be seen in the instantaneous average moment $\langle p_\mathrm{x} \rangle$, Fig. 3.5a, the driven dynamics is heavily dominated by the external field, and the more intense the field, the larger the acquired momentum.

Turning to the integrated asymmetry, Fig. 3.5b, the shape of the electron's average momentum is clearly in the same manner as for the field-free case discussed in the last section. An increase in field intensity of the driving pulse is also reflected in an increase in the measured asymmetry.

The photoelectron spectra and energy-resolved asymmetries $A(E_\mathrm{kin}, T)$ with $E_\mathrm{kin} = p_\mathrm{x}^2/2m_\mathrm{e}$ are shown in Fig. 3.6. The overall shape of the spectra shows trend towards lower kinetic energies until approximately 35 fs with an increase

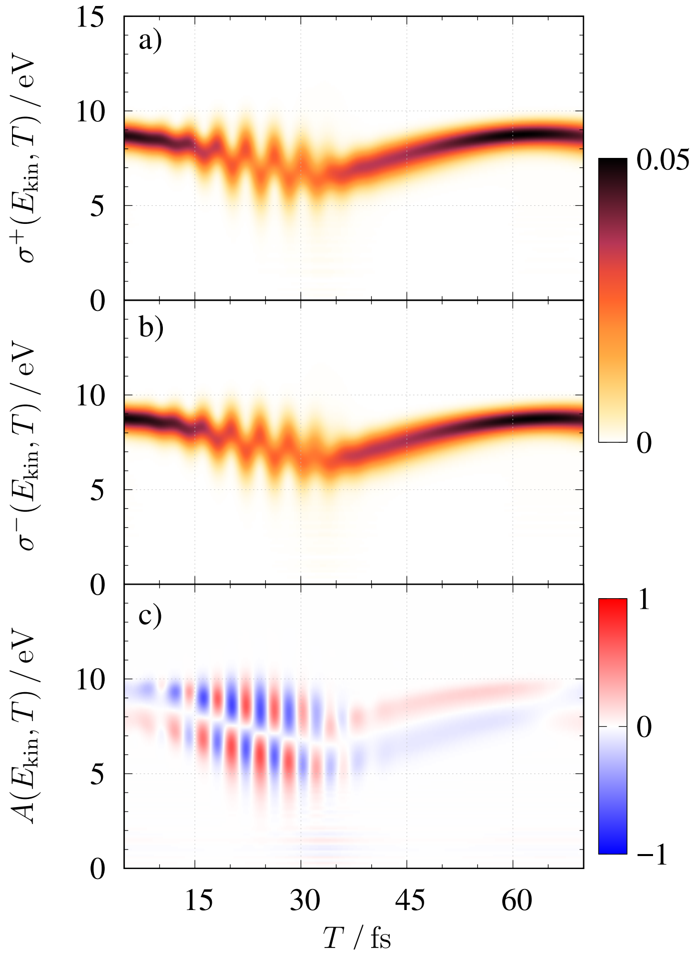

Figure 3.6. Photoelectron spectra $\sigma^{\pm}(E_{\mathrm{kin}}, T)$ (a+b) and energy-resolved asymmetries $A(E_{\mathrm{kin}}, T)$ (c) for the driven adiabatic setting ($R_{\mathrm{c}} = 1.5\,\text{Å}$).

afterwards. Considering intrinsic dynamics alone, 35 fs mark the moment, when the electronic motion changes direction. The dynamics induced by the IR-field centered around $T_{\mathrm{IR}} = 24\,\mathrm{fs}$ manifest itself by accelerating or decelerating the electron resulting in the asymmetry quickly varying in the region of 15 to 35 fs, i.e. when the IR-field is strongest.

Further information is found in the resolved asymmetry shown in Fig. 3.6c: For ionization times $T < 10\,\mathrm{fs}$, i.e. prior to the onset of the IR-field, the asymmetry is negative for kinetic energies above 10 eV, and positive for energies below that. As the electron has a negative intrinsic momentum at these times, emission in backward direction is accelerated, while kinetic energies in forward direction are lowered. During the IR-pulse, the electron's average momentum changes with the field leading to the characteristic streaking features [103]. Here, the kinetic energy of the emitted electron is shifted according to the vector potential of

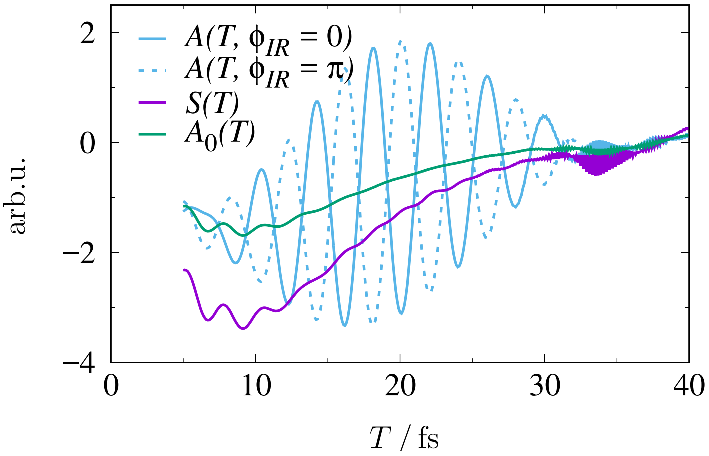

Figure 3.7. Integrated asymmetry for phase-shifted driving fields. The field-driven asymmetries oscillate around the field-free values A_0. The summation of the asymmetries derived from fields with CEP phases $\phi_{\mathrm{IR}} \in \{0, \pi\}$, $S(T)$, yields a value twice that of the field-free asymmetry as the IR-induced contributions cancel each other.

the driving IR-field [104, 105]. It should be noted, however, that the transition region from negative to positive asymmetries follows the energy distribution of the system, when no IR-pulse is present. After 40 fs the influence of the IR-field is gone and dynamics dominated by nuclear motion take over, with the electron's average momentum now leading to positive asymmetries for higher kinetic energies and vice versa for negative asymmetries.

3.2.3 Reconstruction Technique

In the last section, the system's dynamics was driven by a moderately intensive IR-field, and it was shown, that the induced acceleration dominated heavily over the electron's intrinsic momentum. As a consequence, the measured asymmetry in the photoelectron spectrum is affected accordingly. Fig. 3.7 (light blue curves) shows the integrated asymmetry for two driving fields with a carrier-envelope-phase shift of π. As expected, the change in field orientation "flips" the asymmetry. The two asymmetries intersect, when the IR-fields' vector potential is zero and match exactly the asymmetry of the non-driven case, $A_0(T)$ (green curve). This means that the driving field does not alter the system's electronic state and consequently the intrinsic dynamics, but simply linearly adds to them, so that the intrinsic dynamics should still be observable – although overlaid by the field-induced dynamics.

Considering the sum of the asymmetries, $S(T)$, obtained from the pump-probe

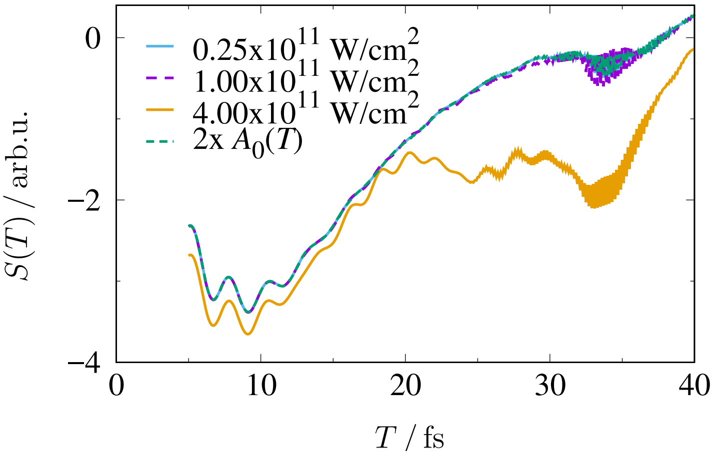

Figure 3.8. Reconstruction of intrinsic dynamics of the adiabatic system ($R_c = 1.5\,\text{Å}$) for different intensities. The field-free asymmetry (A_0, green line) is compared to the sum of asymmetries with phase-shifted CEPs. Higher intensities in the driving IR-field excite higher lying electronic states, which in turn alters the intrinsic dynamics.

arrangements with CEP phases $\phi_{\mathrm{IR}} \in \{0, \pi\}$,

$$\begin{aligned} S(T) &= A(T, \phi_{\mathrm{IR}} = 0) + A(T, \phi_{\mathrm{IR}} = \pi), \\ &= A_0(T) + A_{\mathrm{IR}}(T, \phi_{\mathrm{IR}} = 0) \\ &+ A_0(T) + A_{\mathrm{IR}}(T, \phi_{\mathrm{IR}} = \pi), \end{aligned} \tag{3.11}$$

a value of twice the intrinsic asymmetry, $A_0(T)$, is found, Fig. 3.7 (violet curve). This is explained by decomposing the total asymmetry into contributions which stem from intrinsic dynamics (A_0) and those from field-induced dynamics (A_{IR}). The latter shows a flip in sign when the CEP phase is changed by π, leading to a cancellation of the two terms.

For driving pulses of higher intensities, this reconstruction technique breaks down as the field-induced population transfer to higher lying electronic states starts to significantly alter the intrinsic system's dynamics. Fig. 3.8 shows a comparison of the summed asymmetries, $S(T)$, for different intensities of the driving IR-field and the non-driven asymmetry, A_0. While field strengths of up to $1 \times 10^{11}\,\mathrm{W\,cm^{-2}}$ allow for an accurate reconstruction, higher intensities lead to diverging results as the intrinsic dynamics are altered.

3.3 Dynamics in a Non-adiabatic Setting

The intrinsic dynamics of the one-electron Shin-Metiu model for strong coupling ($R_\mathrm{c} = 2.5\,\text{Å}$) is of diabatic character [66]. While the electronic motion adapts adiabatically to nuclear geometry changes for the weakly coupled setting ($R_\mathrm{c} = 1.5\,\text{Å}$), electronic density remains mostly stationary in the diabatic setting. The dynamics is initiated with a vibrational wave packet centered around $R_0 = -3.0\,\text{Å}$ in the electronic ground state. This positioning on the potential energy surface, see Fig. 2.4, provides just enough energy for the mobile nucleus to switch from one potential well to the other. Here, an avoided crossing of the lowest two electronic states ($n = 0$ and $n = 1$) is encountered at the central position $R = 0\,\text{Å}$. Fig. 3.9c and d show the momentum expectation value, $\langle p_\mathrm{x} \rangle(t)$, of the bound electron and the mobile nucleus during the field-free propagation.

The mobile nucleus passes the minimum of the left potential well at approximately 12 fs (Fig. 3.9a) and reaches the central position ($R = 0\,\text{Å}$) at $t = 24\,\text{fs}$. At 39 fs the turning point of the right potential well is reached and the average momentum acquires negative values (Fig. 3.9b). The central position is passed a second time around $t = 54\,\text{fs}$.

During this time, the electronic average momentum increases alongside the nuclear average momentum only during the first 10 fs. At $t = 24\,\text{fs}$ the diabatic transition from the electronic ground state to the first excited state occurs and the electron's average momentum spikes. Afterwards, the electronic average momentum ceases, as the electron's density remains mostly stationary and no transition between states occurs. At $t = 54\,\text{fs}$ the nucleus passes the central position once more and another spike in the electronic average momentum can be seen.

While the increases of the electronic average momentum are positive, the integrated asymmetry (A_0) shows negative spikes at the times of transition, remaining nearly zero during other periods. This results from interference of the emitted signals stemming either from the electronic ground or first excited state, see Ref. 66 for details.

As for the adiabatic case ($R_\mathrm{c} = 1.5\,\text{Å}$), an IR-field centered around $T_\mathrm{IR} = 24\,\text{fs}$ with different ϕ_IR is applied. Like before, a reconstruction of the non-driven asymmetry A_0 by summation of phase-shifted calculations is attempted. Fig. 3.10 shows the calculated values for different intensities of the driving IR-field. While the intrinsic dynamics remain observable, accuracy decreases for higher intensities as for the adiabatic setting.

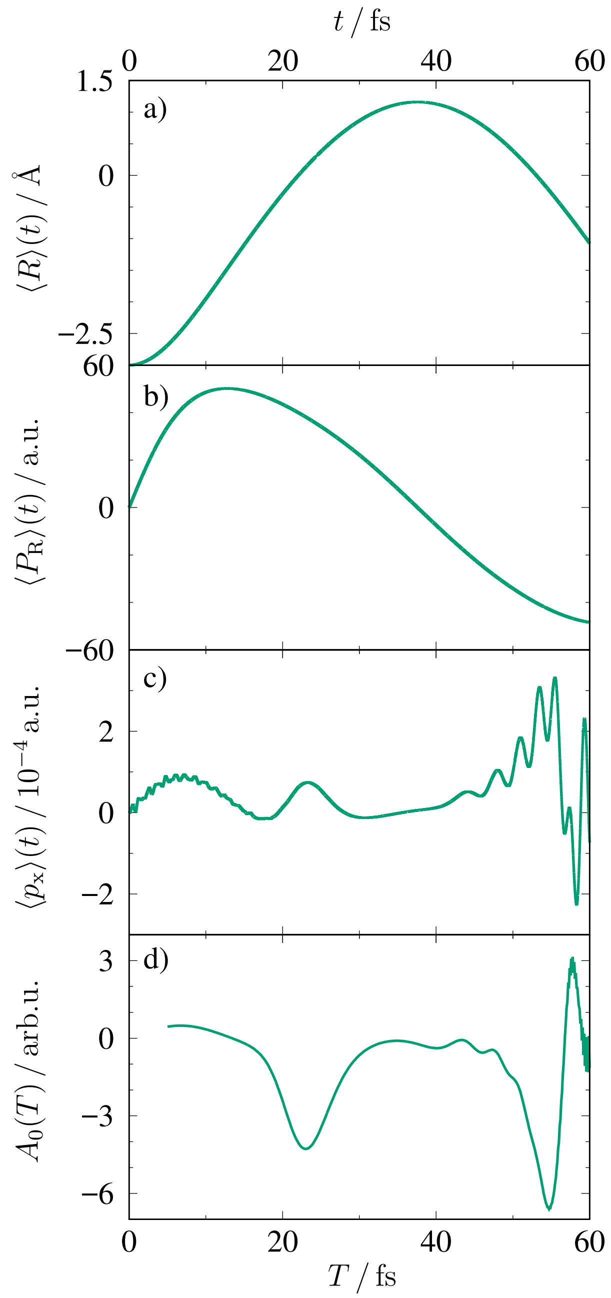

Figure 3.9. Intrinsic dynamics for the diabatic setting ($R_\mathrm{c} = 2.5$ Å). a) Instantaneous average position $\langle R\rangle(t)$ of the mobile nucleus. b+c) Instantaneous average momentum of the electron, $\langle p_\mathrm{x}\rangle(t)$, and mobile nucleus, $\langle P_\mathrm{R}\rangle(t)$. d) Non-driven asymmetry A_0.

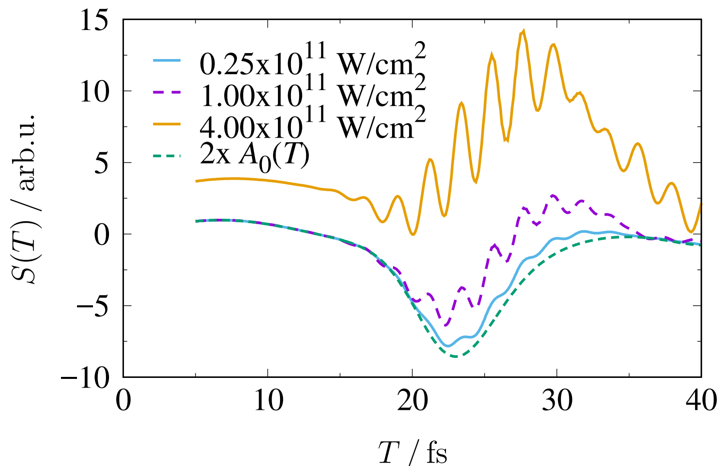

Figure 3.10. Reconstruction of intrinsic dynamics of the diabatic system ($R_c = 2.5\,\text{Å}$) for different intensities. The field-free asymmetry (A_0, green line) is compared to the sum of asymmetries with phase-shifted CEPs. Compared with the adiabatic case, reconstruction is successful as well (blue curve), but starts to break down at higher intensities of the driving field (violet and orange curves).

3.4 Superposition States

3.4.1 Intrinsic Dynamics

In the last two sections, an adiabatic (Sec. 3.2) and a diabatic setting (Sec. 3.3) were investigated. There the dynamics was initiated in a single adiabatic state. In the adiabatic case, the system remained in that state, for the diabatic setting, however, a nearly complete non-adiabatic population transfer to the next higher state, $n = 1$, occurred. This sections considers the case of multiple electronic states contributing to the system's dynamics at the same time. For this, the model is prepared for weak electron-nuclear coupling ($R_c = 1.5\,\text{Å}$) with a normalized initial wave packet created as a superposition of the two lowest electronic states, φ_0 and φ_1:

$$\psi_\pm(x, R, t = 0) = N_{0,\pm} \mathrm{e}^{\beta_\mathrm{R}(R-R_0)^2} [\varphi_0(x; R) \pm \varphi_1(x; R)]. \tag{3.12}$$

Here, ± denotes a positive and negative superposition, respectively, with the vibrational wave packet initially centered around $R_0 = -2.5\,\text{Å}$ with a width of $\beta_\mathrm{R} = 7.14\,\text{Å}^{-2}$, see Fig 3.11. $N_{0,\pm}$ serves as a normalization constant for the two superpositions.

As can be seen in Fig. 3.12, the superposition leads to rapid oscillations in the instantaneous average momenta, $\langle p_\mathrm{x}\rangle(t)$ and $\langle P_\mathrm{R}\rangle(t)$. While initial expectation values are positive for the positive superposition (ψ_+), they are phase-shifted by

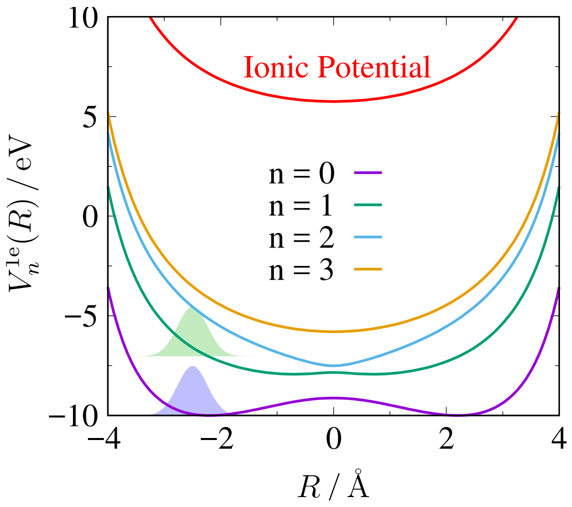

Figure 3.11. Construction of superposition states $\psi_\pm$. Potential energy surfaces $V_n^{1\mathrm{e}}(R)$ with vibrational wave packets in the ground and first excited state.

π for the negative superposition (ψ_-). The oscillation period is approximately 1.2 fs, which corresponds to the energy difference $\Delta E = V_1(R = -2.5\,\text{Å}) - V_0(R = -2.5\,\text{Å}) = 3.4\,\mathrm{eV}$ of the two electronic states involved. For the nuclear momentum, the same oscillatory behaviour is found, however, with a precession of both superposition states around a common overall value.

Additionally, a decrease in amplitude occurs within the first 10 fs for the oscillations. This is explained by the individual movement of the vibrational wave packets of the two states involved: While the wave packet of the electronic ground state starts close to a local minimum and is barely accelerated, the wave packet of the first excited state experiences a strong energy gradient towards positive nuclear coordinates. Assuming that only the two states from each superposition contribute to the dynamics, the wave function can be separated into an electronic (ϕ) and nuclear part (χ):

$$\psi_\pm(x, R, t) = \chi_0(R, t)\,\phi_0(x, t; R) \pm \chi_1(R, t)\,\phi_1(x, t; R). \tag{3.13}$$

Consequently the instantaneous average momentum can be expressed as

$$\langle p_\mathrm{x}\rangle(t) = \int \mathrm{d}R\,\chi_0^*(R, t)\chi_1(R, t) \int \mathrm{d}x\,\phi_0^*(x, t; R)p_\mathrm{x}\phi_1(x, t; R) + \text{c.c.}, \tag{3.14}$$

where the expectation value of a single state vanishes. Here, $\phi_n(x, t; R)$ represents the nth electronic state, $\varphi_n(x; R)$, after it evolved according to Eq. (1.7). Since the different eigenstates have different eigenenergies, their phases, $\mathrm{e}^{-\mathrm{i}E_n(R)t}$, evolve differently and their phase relation is changed. As the first part of Eq. (3.14) describes nuclear correlation and the nuclear part of both superposition states is identical, it can be concluded that the fast oscillations stem from

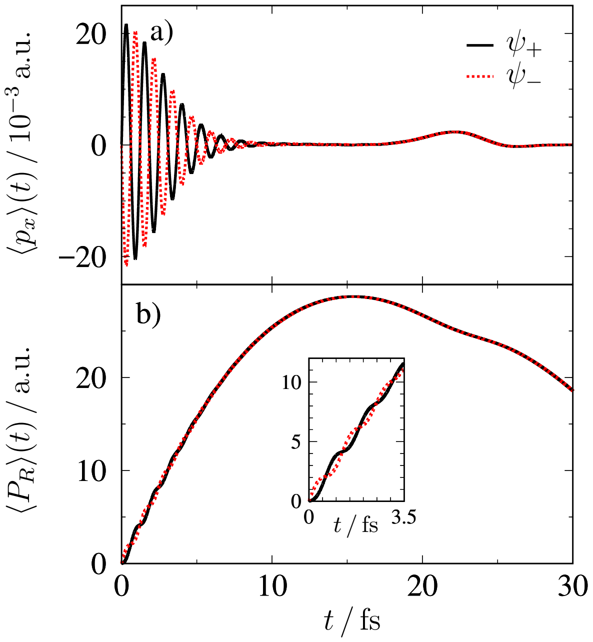

Figure 3.12. Instantaneous average momenta for superposition states. a) Electronic momentum $\langle p_\mathrm{x} \rangle(t)$ for positive (black) and negative (red) superposition of the electronic ground and first excited state. b) Nuclear momentum $\langle P_\mathrm{R} \rangle(t)$. Inset: Zoom of $\langle P_\mathrm{R} \rangle(t)$ for early times.

the different phases of the wave packets in their respective electronic states. However, only when the nuclear wave packets of both states spatially overlap, $\langle p_\mathrm{x} \rangle(t)$ can assume non-zero values. This overlap is measured by the nuclear correlation function c_{nm},

$$c_{nm}(t) = |\,\langle \chi_n(t) | \chi_m(t) \rangle\,|, \tag{3.15}$$

where $n = 0$ and $m = 1$ for the first two electronic states. The function $c_{01}(t)$ is depicted in Fig. 3.13 with a decay in the first 10 fs leading to the decrease of the the electron momentum.

The electron momentum expectation $\langle p_\mathrm{x} \rangle(t)$, Fig. 3.12a, displays another feature between 20 and 25 fs, when a positive increase occurs in both superposition states. In contrast to the initial dynamics, this increase exhibits no oscillations. Inspecting the relative populations of the different electronic states,

$$P_n(t) = |\,\langle \varphi_n | \psi_\pm(t) \rangle\,|^2, \tag{3.16}$$

a non-adiabatic population transfer of approximately 10% from the first to the second excited state is found, see Fig. 3.13b[2]. Simultaneously the nuclear

---

[2] Note, that the relative population $P_n(t)$ is identical for both superposition states.

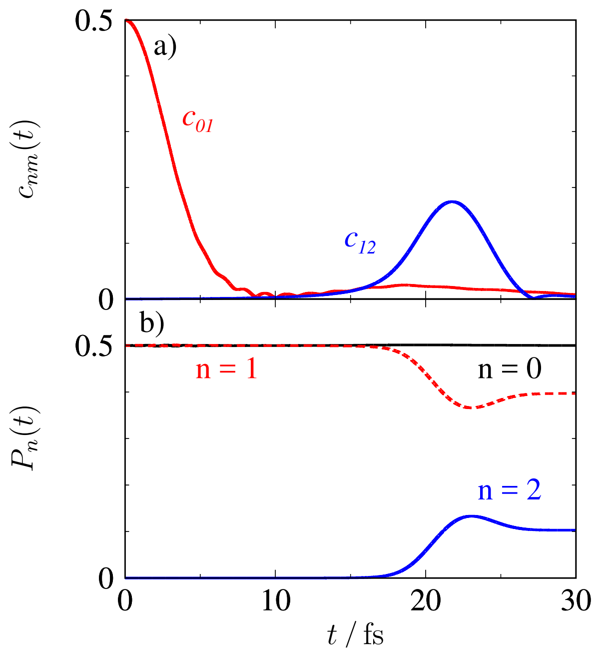

Figure 3.13. Nuclear correlation functions and relative populations for both superposition states. a) Nuclear correlation functions $c_{nm}(t)$ for the ground and first excited states (red) & first and second excited states (blue). b) Relative populations $P_n(t)$ of the three lowest states.

correlation function $c_{12}(t)$ between these two states rises. As the phase of the first excited state is not important for the non-adiabatic transition, each individual configuration retains the same phase relation between the electronic states φ_0 and φ_1, resulting in the same sign in the asymmetry.

Note that the electronic coherences are also present for the system prepared with a single electronic state, cf. Chapter 3.2. As the population transfer is much smaller for the ground and first excited state in the adiabatic setting $(R_c = 1.5)$ Å, oscillations are much smaller as well.

3.4.2 Pulse Width Dependence

In the last section, it was shown how population of two spatially overlapping electronic states leads to fast oscillations in the electronic average momentum $\langle p_x \rangle(t)$. To resolve such fast changes in the asymmetry, it is necessary to employ an ionizing XUV pulse short enough in time domain, or spectrally broad enough to address both states φ_0 and φ_1. Fig. 3.14 compares the acquired asymmetry A_0 for different pulse lengths.

The longest pulse with a full width at half maximum (FWHM) of 2.32 fs results in an asymmetry with a maximum amplitude of only 0.001 within the first 10 fs, i.e. when the rapid oscillations in $\langle p_x \rangle(t)$ occur. Shorter pulses with widths of

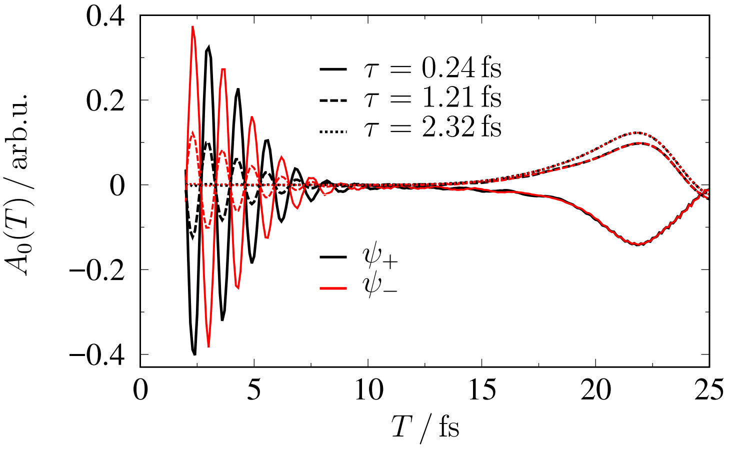

Figure 3.14. Integrated asymmetry A_0 of superposition states for different pulse widths. Black lines correspond to ψ_+, while red lines represent ψ_-. Values for the oscillations of the long pulse ($\tau_{\mathrm{XUV}} = 2.32\,\mathrm{fs}$) have an amplitude of up to 0.001.

1.21 fs and 0.24 fs, respectively, display much larger values during this time. This can be explained in two ways: The longer the pulse in time domain, the more the average of the fast oscillations gets reflected in the asymmetry. Or, viewing the fast oscillations as a result from the interference of ionization signal from different electronic states [126], the longer the pulse, the smaller the spectral overlap of different states with the ionizing field.

An interesting behaviour is found for the asymmetry during later times: While the longest pulse ($\tau_{\mathrm{XUV}} = 2.32\,\mathrm{fs}$, corr. to $\sigma_{\mathrm{XUV}} = 0.78\,\mathrm{eV}$) cannot resolve the rapid oscillations, the asymmetry increase of $\langle p_{\mathrm{x}} \rangle(t)$ between 20 and 25 fs is well represented. For a pulse width of 1.21 fs ($\sigma_{\mathrm{XUV}} = 1.50\,\mathrm{eV}$) the same behaviour is found, however, with slightly decreased amplitude. In contrast, the shortest pulse ($\tau_{\mathrm{XUV}} = 0.24\,\mathrm{fs}$, $\sigma_{\mathrm{XUV}} = 7.58\,\mathrm{eV}$) leads to a sign change in the asymmetry. This can be traced back to its spectral width, which is the only one sufficient to probe all three populated states. The resulting photoelectron spectrum is therefore comprised of the interference of the three, which – in this specific case – leads to a negative asymmetry.

3.4.3 Wavelength Dependence

The last section covered the influence of the ionizing pulse's spectral width on the measured asymmetry. In this section the wavelength dependence is investigated. For this XUV pulses of fixed width ($\tau_{\mathrm{XUV}} = 0.24\,\mathrm{fs}$, $\sigma_{\mathrm{XUV}} = 7.58\,\mathrm{eV}$) are employed for central wavelengths of $\lambda_{\mathrm{XUV}} = 60$, 75 and 90 nm, corresponding to (central) photon energies of 20.66, 16.53, and 13.78 eV, respectively. Ad-

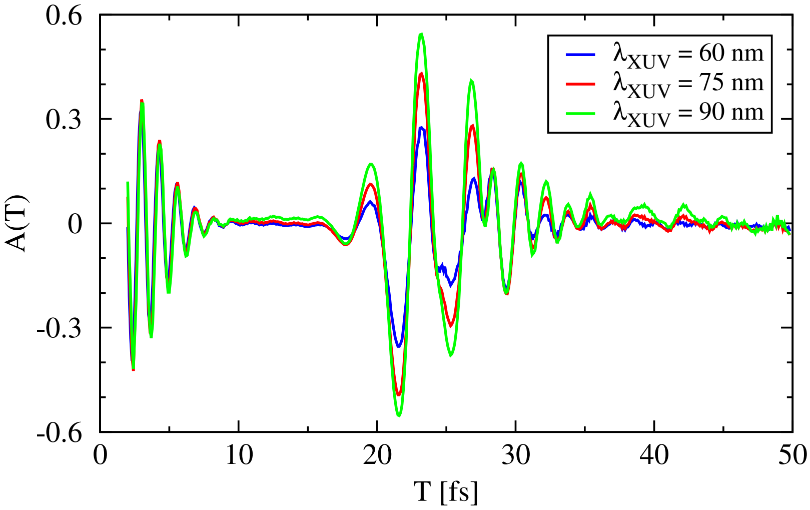

Figure 3.15. Measured asymmetry $A(T)$ for different wavelengths λ_{XUV} of the ionizing pulse, with a driving few-cycle IR-field centered around $T_{\mathrm{IR}} = 24\,\mathrm{fs}$.

ditionally, the same IR-field from earlier sections is applied ($\lambda_{\mathrm{IR}} = 1200\,\mathrm{nm}$, $\tau_{\mathrm{IR}} = 14.7\,\mathrm{fs}$, $T_{\mathrm{IR}} = 24\,\mathrm{fs}$, $E_{0,\mathrm{IR}} = 1 \times 10^{11}\,\mathrm{W\,cm^{-2}}$). Calculated asymmetries $A_{\mathrm{IR}}(T)$ are displayed in Fig. 3.15.

The characteristics of $A_{\mathrm{IR}}(T)$ remain the same for all wavelengths, with a good agreement for the fast oscillations at early times ($t \leq 15\,\mathrm{fs}$). For the oscillations induced by the IR-field, absolute asymmetry values are increased for longer wavelengths.

Assuming plane waves for the continuum states, i.e. $\mathrm{e}^{\mathrm{i}kx}$, where k is the wave vector, this can be explained as follows: While the shortest wavelength (60 nm) corresponds to the largest photon energy, spectral overlap with the continuum states is reduced as high-lying continuum states (large k) vary quickly in the spatial domain. This then leads to smaller values of $A_{\mathrm{IR}}(T)$ as the relative spectral overlap is reduced. Therefore, the closer the wavelength of the XUV-pulse to the ionization threshold, the larger the measured asymmetry.

It should be noted that wavelengths closer to the ionization threshold – but still above it – exhibit lower total emission signal stemming from single-photon processes as larger parts of the pulse lack the required photon energy to ionize the system. However, while this absolute spectral overlap decreases, the relative value of the overlaps increases, and the asymmetry along with it.

3.5 Discussion

In this chapter, the single-electron Shin-Metiu model [97, 98] was employed as a charge-transfer model to investigate the effects of correlated electron-nuclear dynamics on photoelectron spectra when driven by a moderately intense IR-field. It was shown, that the intrinsic dynamics, i.e. the system's dynamics in the absence of a driving field, are visible within the *forward/backward* asymmetry of the photoelectron spectrum. Furthermore, dynamics induced by an IR-field can also be seen within the asymmetry as they are typically larger than the intrinsic dynamics. However, it was found that by performing two measurements with driving fields that are phase-shifted by π, the intrinsic dynamics can be recovered as long as the driving fields are weak enough.

These findings were shown to persist for systems, which behave mainly adiabatic, as well as predominantly diabatic.

Furthermore, an investigation of superposition states showed that the asymmetry of the photoelectron spectrum is sensitive to even small details of the momentum distribution of the electron wave packet.

Lastly, comparison of results achieved from varying different parameters of the ionizing pulse revealed, that longer wavelengths and temporally shorter pulses lead to an enhancement of the asymmetry.

CHAPTER

Attosecond Ionization Dynamics with Correlated Electrons

4

The photoionization from the last chapter included coupled electron-nuclear dynamics for a charge-transfer model, naturally, the Shin-Metiu model [97,98] is extended by the addition of a second electron [64] and the study of electron-electron correlation dynamics.

Many processes in multi-electron systems involve relaxation of electron shells, e.g. photoionization, electron-impact ionization, Auger and other radiative processes [134,135]. To describe these effects, the single-active electron approximation (SAE) is commonly applied, however, it requires that the dynamics are sufficiently slow so that the electrons remaining bound can adjust to the altered environment [136]. In contrast, for fast interactions of multi-electron systems with ultrashort XUV or x-ray fields, electron correlation plays a crucial rule, and the SAE cannot necessarily be applied reliably. Not only the photoelectron angular momentum distribution is affected by the electron correlation, but the state of the residual cation as well. As such, the remaining (bound) electron can be excited to higher states (shake-up process) or even emitted subsequently in an Auger process. With the advent of ultrashort femto- or even attosecond XUV pulses being available either via table-top high-order harmonic generation or the newest generation of (X)FEL sources, these processes can be observed in real time, e.g. employing the attosecond streaking technology [59,137–140].

Ionization dynamics of multi-electron atoms with attosecond time resolution have been heavily investigated in experimental and theoretical studies during the past few years [141]. There, most theoretical studies focused on the simplest two-electron atom, helium. Studied effects include the Wigner-Smith time delay, field-dressing of bound and continuum states, as well as electron-electron correlation in the presence of an (infrared) laser field in the context of streaking spectroscopy [141–145]. Moving to molecules, the physics becomes even more complex due to the multi-center structure. For example, Ning et al. examined the simplest, prototypical molecule, H_2^+, and found that the two scattering centers led to pronounced interference effects [146] (Cohen-Fano interferences [147]). This prototype molecule, however, inherently does not involve any multi-electron effects. Other theoretical studies include larger model molecules, e.g. endohedral complexes of type A@C_{60} [148,149], or small amino acids, where ionization with subsequent charge migration was investigated employing multi-configurational approaches [150–155]. Few works, however, have considered both, correlated electron dynamics and nuclear motion [156–159].

In the following, the molecular model system originally suggested by Shin and Metiu [97,98], and extended by the group of Engel to include two electrons [65, 69], is employed to investigate correlated ultrafast attosecond photoionization. To accurately describe the interaction of multiple electrons and of electrons with nuclei, two electronic and one nuclear degree of freedom are realized. The system is setup in an anti-parallel spin configuration with an asymmetric nuclear distribution, leading to different (weak and strong) binding energies of the two electrons.

Several pathways will be observed: a) "direct" emission of one of the electrons away from the other electron, and b) "indirect" emission with acceleration towards the other electron. While the former process involves only minor electron-electron interaction, the latter is strongly characterized by inelastic and elastic scattering. Depending on the type of scattering, the second electron is either excited to higher bound states, known as shake-up, or adopts the momentum of the electron primarily accelerated by the electric field, and is emitted in its stead.

As a consequence, not only is the photoelectron spectrum heavily dependent on the exact ionization pathway occurring, but the final state of the residual ion as well. To break down the complexity of the ionization process, emission is analyzed separately for the weakly and strongly bound electron, as well as its exact pathway during the process. Additionally, nuclear dynamics is shown to drive non-adiabatic transitions in the residual ion, as the potential energy curves of the excited molecule differ substantially from its initial configuration.

This chapter is based on Ref. [135] and structured as follows: First, a description of the employed model and its initialization is given in sections 4.1 and 4.1.1, while a separation approach for distinguishing the weakly and strongly bound electron is introduced in section 4.1.2. The ionizing attosecond pulse is discussed next, 4.1.3. Afterwards the full fermionic system is investigated, 4.2, followed by the subsystems of distinguishable electrons, 4.3, and the photoelectron momentum distribution, 4.4. A discussion concludes the chapter, 4.5.

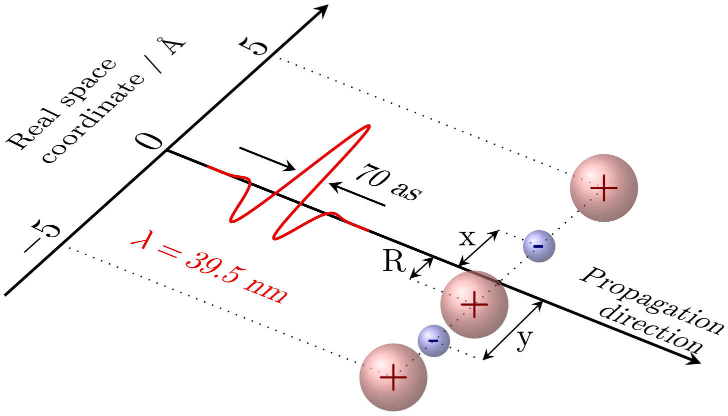

Figure 4.1. Configuration of the extended Shin-Metiu system: An ultrashort XUV pulse is used to ionize a linear molecule aligned with the pulse's polarization axis. The molecule consists of two fixed nuclei at ±5 Å, two mobile electrons with coordinates x and y, and a movable central nucleus at R. A pulse of wavelength $\lambda = 39.5$ nm and temporal width of 70 as provides sufficient energy for single and even double ionization. Note, that here the mobile nucleus is initially localized at negative R values, whereas the two electrons reside on both sides. Thus, in the electronic ground state, the electron at negative coordinates is stronger bound than the electron located at positive values. Source: Ref. [135]

4.1 Model Setup

The employed setup in this chapter represents an extension to the one from the last chapter (4.1), the original Shin-Metiu model [97, 98], discussed in length in chapter 2.2. Extended by addition of a second electron, electron-electron correlation dynamics during ionization with an attosecond XUV pulse can be studied. Fig. 4.1 shows a schematic of the system: Particles are lined up in one dimension with two fixed nuclei of charge Z_1 and Z_2 at positions $\pm L/2$. In between, one nucleus (charge Z, coordinate R) and two electrons (coordinates x and y) are mobile. The former is described on a grid from $R \in [-4.99, 4.99]$ Å with 128 points, while the two electrons require bigger grids in the range of $\{x, y\} \in [-240, 240]$ Å with 1024 points each, as ionization leads to emission to large coordinates. The mobile nucleus remains well confined between the fixed outer nuclei during this process, and its grid size was chosen so that numerical singularities at the points of overlapping nuclei is avoided. The distance of the fixed nuclei is chosen as $L = 10$ Å and represents the molecule's size. By defining the spatial grid sizes in that manner, momentum resolutions of $\mathrm{d}p_{\mathrm{x,y}} = 6.9 \times 10^{-3}$ a.u. for the electronic grids, and $\mathrm{d}P_{\mathrm{R}} = 0.33$ a.u. for the nuclear grid are achieved, which is more than sufficient for an accurate description.

The system's potential is given by Eq. (2.3), where nuclear charges are chosen as $Z = Z_1 = Z_2 = 1$. The truncation parameters specifying the interaction strength between electrons and the fixed nuclei (R_f), the mobile nucleus (R_c), and among each other (R_e) are set as $R_\mathrm{f} = R_\mathrm{c} = R_\mathrm{e} = 1.5\,\text{Å}$, which corresponds to the weak-coupling regime [133]. The resulting potential energy surfaces $V_n^{2\mathrm{e}}(R)$ are displayed in Fig. 4.2 for the first four electronic eigenstates, which have been calculated via imaginary time propagation (ITP) using a time step of 10 as (see chapter 1.1.4). Here, forcing a symmetric spatial wave function during the ITP results in an anti-symmetric spin configuration. As during ionization single- and double ionization occur, the potential energy surfaces for the one-electron system, $V_n^{1\mathrm{e}}(R)$, and the ionic potential are given as well.

Table 4.1. Simulation parameters for the 2e-Shin-Metiu system.

Parameter	**Number of Points**	
N_R	128	
$N_x,\ N_y$	1024	
	Value	
dt	10 as	
$R_\mathrm{f},\ R_\mathrm{c},\ R_\mathrm{e}$	1.5 Å	
	Range / Å	**Spacing / Å**
R	$[-4.99, 4.99]$	0.079
x, y	$[-240, 240]$	0.47
	Range / a.u.	**Spacing / a.u.**
P_R	[-21.2,20.8]	0.33
$p_\mathrm{x},\ p_\mathrm{y}$	[-3.54,3.54]	6.9×10^{-3}

The time-dependent Schrödinger equation for the Hamiltonian $\hat{\mathcal{H}}(t)$ defined in Eq. (1.69) is solved iteratively with a time step of 10 as using the split-operator technique [76] (chapter 1.1.3) and the FFTW 3 library [96] for Fourier transforms. The length of the time step has been confirmed sufficient, with details given in section 4.1.3. The simulation is set to start at $t_0 = -10\,\mathrm{fs}$ with the ionizing pulse centered around $T = 0\,\mathrm{fs}$.

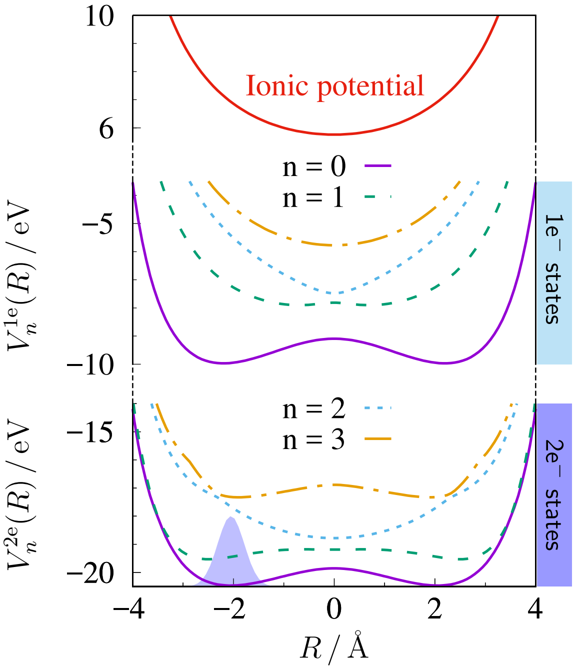

Figure 4.2. Potential energy surfaces $V_n^{2e}(R)$ of the extended (lower third) Shin-Metiu system. The Gaussian distribution (blue-shaded) in the electronic ground state represents the initial vibrational wave packet. The curves in the middle, $V_n^{1e}(R)$ correspond to the original, one-electron Shin-Metiu model, and apply after emission of one electron.

4.1.1 Asymmetric system Initialization

The initial state used during propagation is constructed as a product state of a vibrational wave packet, $\chi(R)$, in the electronic ground state, $\varphi_0^{2e}(x, y; R)$:

$$\Psi(x, y, R, t_0) = \chi(R)\, \varphi_0^{2e}(x, y; R). \tag{4.1}$$

The nuclear part of the initial wave function, $\chi(R)$, is described by a Gaussian distribution centered around one local minimum of the double-well potential at $R_0 = -2.05\,\text{Å}$ (see shaded area in Fig. 4.2). By this, intrinsic vibrational dynamics is reduced to a minimum. The nuclear wave function reads

$$\chi(R) = N_0\, \mathrm{e}^{-\beta_R (R-R_0)^2}, \tag{4.2}$$

where the Gaussian's width is defined by $\beta_R = 7.14\,\text{Å}^{-2}$ and N_0 serving as a normalization constant.

Initializing the system in this manner, an asymmetric nuclear geometry is obtained, where an increased nuclear charge density is found on the left-hand side of the molecule. This configuration corresponds to one of two energetically degenerate realizations. Systems, where the vibrational wave packet resides in one potential well, represent a common situation and can be encountered, for example, in NH_3 inversion or isomerization processes.

As a consequence of this asymmetric geometry, the electron localized between the fixed left and the mobile nucleus is bound stronger, while the other resides closely to the fixed right nucleus and has a lower binding energy. The later sections will present the impact of this asymmetry.

Note that the chosen initial state does not correspond to the absolute ground state of the system: While the assumed factorization of electronic and nuclear degrees of freedom is an assumption due to electron-nuclear correlations, placing the vibrational wave packet in only one of the two equal potential wells plays a far bigger role. The real ground state would be more similar to a symmetric superposition of this state and of its mirror image in the other potential well.

4.1.2 Artificial Systems of Distinguishable Electrons

The initial wave function presented in the last section has the electrons located on both sides of the molecule, one electron with a lower, one with a higher binding energy. The top two panels of Fig. 4.3 show the electronic density $\int |\Psi(x,y,R,t_0)|^2 \mathrm{d}R$ at the beginning of the propagation. As the starting configuration barely induces vibrational dynamics, this density distribution is mostly maintained until the ionizing pulse interacts with the system. During the ionization, but especially after the ultrashort pulse, signal can be detected at large coordinates in one (single ionization) or both coordinates (double ionization).

As fermions are indistinguishable particles and the distribution within the electronic wave function is identical for both electronic coordinates, evaluation of only one half of the system, i.e. split along the $x=y$-diagonal, suffices. This property, however, also has an inherent drawback: The origin of any emission signal cannot be traced back to a single electron, i.e. answering the question of which electron – the weakly or strongly bound one – was emitted.

In order to distinguish the different ionization channels, two desymmetrized subsystems are created from the full wave function defined in Eq. (4.1):

$$\text{(A)} \quad \psi_A(x,y,R,t_0) \equiv \Psi(x,y,R,t_0)\,\Theta(x-y), \tag{4.3a}$$

$$\text{(B)} \quad \psi_B(x,y,R,t_0) \equiv \Psi(x,y,R,t_0)\,\Theta(y-x). \tag{4.3b}$$

Here, $\Theta(x)$ is the Heaviside step function, which splits the full (fermionic) system along the $x=y$-diagonal into two partial wave functions, each describing half of the original system. By doing so, the symmetry of x and y is broken, resembling a wave function in Hartree-type product form. As a consequence,

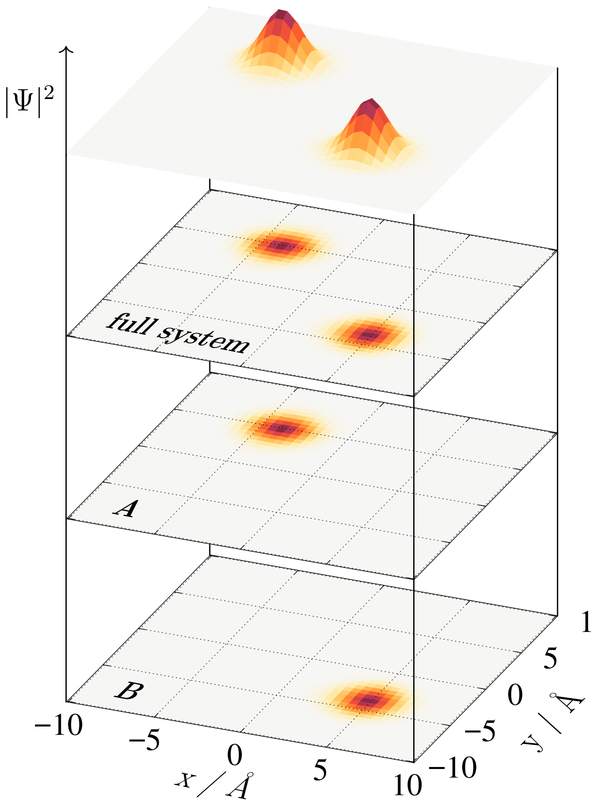

Figure 4.3. Initial wave function, $\int |\Psi(x, y, R, t_0)|^2 \,\mathrm{d}R$, entering the propagation. Top plane: fully symmetric spatial wave function calculated via the relaxation method. Descending from top to bottom: Projection onto the 2D plane of the full system, reduced system with $x \leq y$ (A), and $x \geq y$ (B), respectively. By splitting the full system along the $x = y$-diagonal, the symmetry of electronic coordinates is artificially broken and electrons become distinguishable. Source: Ref. [135]

---

x and y effectively describe identical, yet *distinguishable* electrons in the artificial subsystems A and B. The different ionization pathways revealed by these subsystems' dynamics are discussed in section 4.3.

4.1.3 XUV Field, Temporal Resolution & Phase Dependence

Ionization of the full fermionic system, as well as the subsystems A and B is achieved by employing an attosecond XUV pulse. As the propagation is conducted with a Hamiltonian in velocity gauge (see chapter 1.3.2), the electric field is described via its vector potential $A(t)$, whose polarization is aligned with the molecular axis:

$$A(t) = -\frac{E_0}{\omega}\, f(t-T)\, \sin\big(\omega(t-T)+\phi\big). \tag{4.4}$$

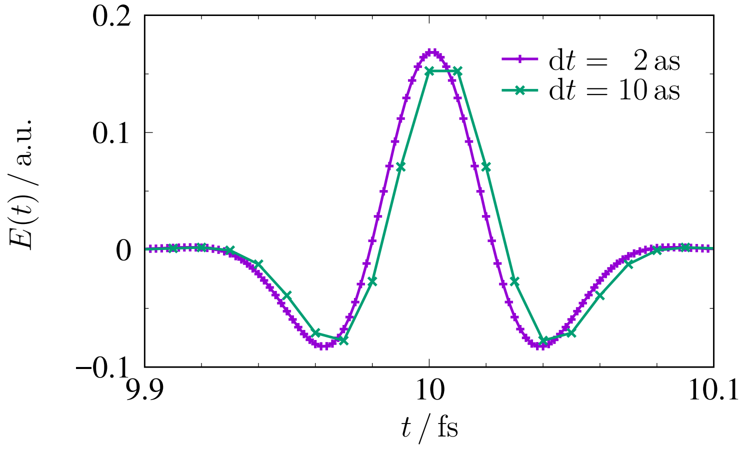

Figure 4.4. Cosine-shaped electric field of the attosecond XUV pulse employed for ionization. Electric field strength $E_0 = 8.7\,\mathrm{V/Å}$ corresponds to $1.0{\times}10^{15}$ W/cm^2, $\lambda = 39.5\,\mathrm{nm}$, FWHM= 70 as. Comparison of temporal grid spacing of dt = 2 as and dt = 10 as. Note that the description of the electric field $E(t)$ in terms of the vector potential $A(t)$ results in an temporal offset between the two time resolutions.

Here, $E_0 = 8.7\,\mathrm{V/Å}$ is the electric field strength (corresponding to an intensity of $1.0{\times}10^{15}$ W cm^{-2}), ω the field's angular frequency, and $f(t-T)$ a Gaussian pulse envelope function centered around $T = 0$ fs with a full-width half-maximum (FWHM) of 70 as. The angular frequency chosen corresponds to a wavelength of $\lambda = 39.5\,\mathrm{nm}$ ($\hat{=}$ 31.4 eV), which is sufficient to doubly ionize the molecule through single photon absorption, cf. Fig. 4.2. The spectral width of this attosecond pulse corresponds to $\sigma = 25.97\,\mathrm{eV}$ and is as such very broad. The carrier-envelope phase (CEP) ϕ of this nearly single-cycle pulse is set to zero, corresponding to a sine-shaped vector potential or an approximately cosine-shaped electric field. Fig. 4.4 shows the electric field for different resolutions of the temporal grid.

Choosing the time step during propagation as dt = 10 as suffices for a pulse description including the main features: one large cycle with positive field values, two small cycles with negative field values. While the pulse is sufficiently resolved in the time domain, the same need not be true for the total description of the system's dynamics. A good measure for estimating the quality of the time step is the field-induced momentum of one of the electrons. For this, the case of single ionization is considered and the instantaneous average momentum $\langle p_\mathrm{y}\rangle(t)$ of the remaining bound electron inspected for a fixed nuclear geometry[1],

---

[1] The calculation of $\langle p_\mathrm{y}\rangle(t)$ is presented in section 4.2.2. For now, the point of Fig. 4.5a is

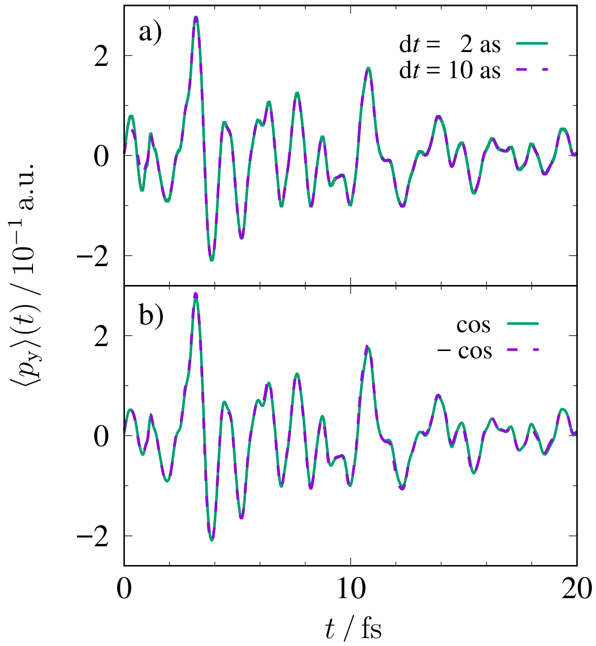

Figure 4.5. Analysis of pulse resolution and CEP via the momentum expectation value $\langle p_{\mathrm{y}}\rangle(t)$ of the electron remaining bound within the *forward-up* pathway. a) Calculations with time step $\mathrm{d}t = 2\,\mathrm{as}$ and $\mathrm{d}t = 2\,\mathrm{as}$ yield the same result indicating sufficient temporal resolution. b) Nearly identical values for $\phi \in \{0, \pi\}$ suggest that the molecular geometry dominates the emission direction during ionization.

see Fig. 4.5a. The nearly identical result for propagations with $\mathrm{d}t = 2\,\mathrm{as}$ and $\mathrm{d}t = 10\,\mathrm{as}$ indicate sufficient temporal resolution for the attosecond XUV pulse and the overall description of the system's dynamics. Hence, the larger time step will be employed.

With the field exhibiting one big half-cycle toward positive values, but only two weak half-cycles towards negative values, a strong accelerations towards positive x coordinates is to be expected. However, calculations employing a field with a CEP of $\phi = \pi$, resulting in a -cosine-shaped electric field, showed that the field orientation actually plays a minor role in determining emission direction. Fig. 4.5b shows the instantaneous average momentum $\langle p_{\mathrm{y}}\rangle(t)$ for a time step of $\mathrm{d}t = 10\,\mathrm{as}$, but with different CEP. This indicates that for the present system, the emission direction is almost exclusively decided by the molecular geometry. As such, the remainder of the investigation will be conducted employing only one CEP, in this case that of a cosine-shaped electric field.

---

to highlight the correct description employing a time step of 10 as.

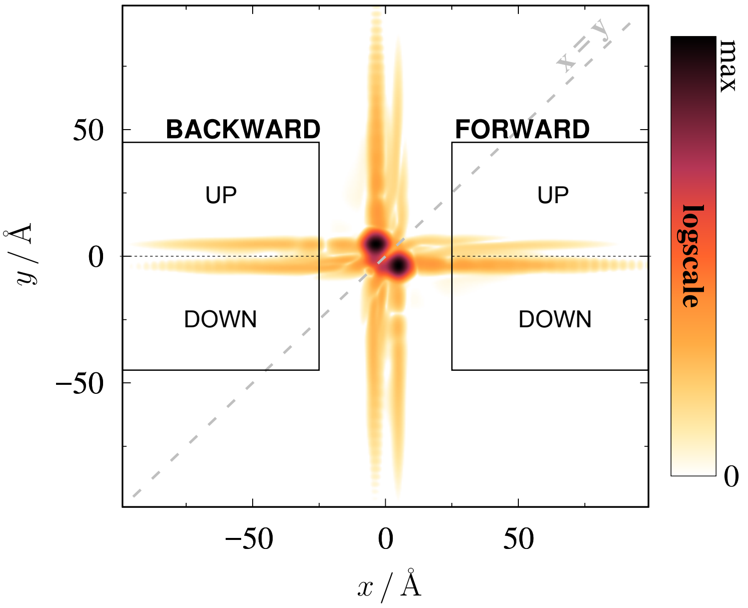

Figure 4.6. 2D electronic density, $\int |\Psi(x, y, R, t = 3\,\text{fs})|^2\,\mathrm{d}R$, of the fully antisymmetric system (reflection symmetry w.r.t. the $x = y$-diagonal) shortly after ionization with an XUV pulse centered at $T = 0\,\text{fs}$. Four different ionization channels can be distinguished, here illustrated for the x direction: Signals emerge either in *forward* ($x > 0$) or *backward* ($x < 0$) direction for positive (*up*) or negative y coordinates (*down*), respectively. The corresponding channels along the y-axis are equivalent. Source: Ref. [135]

4.2 Ionization of a Correlated Fermionic System

4.2.1 Identification of Single Ionization

Ionization of either the full fermionic system or the subsystems A and B is best visualized by the two-dimensional electronic density $\int |\Psi(x, y, R, t)|^2\,\mathrm{d}R$. As the molecule is located at the origin of the x–y-coordinate system, signal in regions with large values in one dimension correspond to single ionization, while large values in two dimensions indicates double ionization. Fig. 4.6 depicts a snapshot of the 2D electronic density at $t = 3$ fs after the ionizing pulse interacts with the system.

Most density remains unionized at the center of the coordinate system, with four double-stripe structures appearing along the coordinate axes. These stripes represent single ionization in *forward* and *backward* direction, where one electronic coordinate stays within ±10 Å. Here, *forward* stands for coordinate values greater zero, while *backward* indicates values smaller zero. Additionally, the symmetry feature along the $x = y$-diagonal axis can be seen.

It should be noted that in general signal corresponding to double ionization is of several magnitudes lower than that of processes, where only one electron is emitted[2]. This is due to the much smaller cross section of double ionization. Consequently, such contributions are not visible in Fig. 4.6. Also note, that no cutoff-function can be applied in the regions corresponding to double ionization due to the continued presence of a Coulomb-interaction partner. This entails an upper duration for the propagation until reflections at the grid ends start to significantly alter the measured signal. Therefore, analysis will focus on the first 20 fs after ionization, during which no grid reflections occur. Note, that slowly decaying excited states lead to auto-ionization at even later times. However, for the pulse properties presented in the next section, the levels of auto-ionization are of low intensity and hence not included in the following discussion.

An apparent feature of the single ionization channels is the occurrence of two emission pathways in every direction. This indicates the presence of two ionization processes, in which the remaining electron stays at different potential minima. Due to the mentioned symmetry property, analysis along one coordinate axis suffices; in this case the x axis is chosen. Here, four distinct channels can be found, which differ in shape and intensity from each other. The labels *forward/backward* are ascribed for positive/negative values in x, and *up/down* for positive/negative values in y, respectively.

As electronic density is driven to large coordinates, density representing ionization needs to be distinguished from that, which is not permanently emitted from the molecule. To isolate the parts of the wave function that correspond to single ionization, the photoelectron dynamics is analyzed solely in regions far from the molecule. To this end, during each time step of the propagation the mask

$$c(x,y) = c_x(x) \cdot \big[1 - c_y(y)\big] \tag{4.5}$$

is applied to the system's wave function. Here, $c_\xi(\xi)$ is defined as

$$c_\xi(\xi) = \begin{cases} 0 & \text{if } 0 \ < \ |\xi| \le \xi_c \\ \sin^2\left(\frac{|\xi|-\xi_c}{\Delta\xi}\frac{\pi}{2}\right) & \text{if } \xi_c < |\xi| \le \xi_c + \Delta\xi \\ 1 & \text{if } \xi_c + \Delta\xi < |\xi| \le 240\,\text{Å} \end{cases} , \tag{4.6}$$

where $\xi \in \{x, y\}$ with corresponding $x_c = 25\,\text{Å}$, $y_c = 45\,\text{Å}$, and $\Delta x = \Delta y = 10\,\text{Å}$. As such, the mask $c(x,y)$ selects parts of the wave function $\psi_{\text{out}}(x,y,R,t) \equiv c(x,y)\,\psi(x,y,R,t)$ at large x and low y coordinates, corresponding to the emission of a single electron along the x coordinate, whereas the other (y) electron remains bound at the parent molecular ion.

---

[2] In the depicted case, double ionization has a probability roughly four orders of magnitude lower than single ionization.

Note, that the mask function presented here is different from the cut-off function employed in chapter 3, Eq. (1.82): While the latter is used to convey the emitted part of the full dimensional wave function onto a smaller grid, which is then propagated separately, the mask function $c(x, y)$ solely determines the evaluation area.

Numerical Artifacts

It was noted, that the ionization signal is several orders of magnitude lower than the parts of the electronic density, in which both electrons remain bound. At these low signal levels, artifacts caused by the imperfect initial electronic wave function occur, which manifest themselves as artificial ionization. In the case of the subsystems A and B, the sharp separation along the $x = y$-diagonal leads to even stronger artificial ionization. To limit this background signal, portions of the wave function reaching large values in x or y until $t = -3$ fs, i.e. well before the attosecond pulse interacts with the molecule, are removed from the total wave function. This is done by truncating $\Psi(x, y, R, t < 3\text{ fs})$ through multiplication with the Heaviside step function product $\Theta(25\,\text{Å} - |x|)\,\Theta(25\,\text{Å} - |y|)$ before further propagation is performed.

4.2.2 Induced Pathway-dependent Dynamics

In this section, the ionization of the full fermionic system is investigated. Fig. 4.6 already showed a snapshot of the electronic density at $t = 3$ fs after ionization with emission of a single electron being the dominant channel. In order to analyze the electron-electron correlation, the dynamics of the electron remaining bound is inspected. For this the instantaneous average momentum, $\langle p_\mathrm{y} \rangle^S(t)$, of the y electron is calculated via its density distributions $\rho_S(p_\mathrm{y}, t)$, where the ionized wave function Ψ_out is separated into the individual emission channels S describing *forward/backward* and *up/down* regions, respectively (see Fig. 4.6). The density distribution of a given region is calculated as

$$\rho_S(p_\mathrm{y}, t) = \iint \left| \widetilde{\psi}^S_\mathrm{out}(p_\mathrm{x}, p_\mathrm{y}, P_\mathrm{R}, t) \right|^2 \, \mathrm{d}p_\mathrm{x}\, \mathrm{d}P_\mathrm{R}, \tag{4.7}$$

where $\widetilde{\psi}^S_\mathrm{out}$ is the Fourier-transformed single ionization wave function ψ^S_out. By normalization of the respective region's total signal with the time-dependent normalization constant N_S, the momentum expectation value is defined:

$$\langle p_\mathrm{y} \rangle^S(t) = N_S(t) \int p_\mathrm{y}\, \rho_S(p_\mathrm{y}, t)\, \mathrm{d}p_\mathrm{y}. \tag{4.8}$$

Fig. 4.7 shows $\langle p_\mathrm{y} \rangle^S(t)$ for each respective channel and illustrates, that in all four cases different dynamics is induced in the parent ion. As discussed in

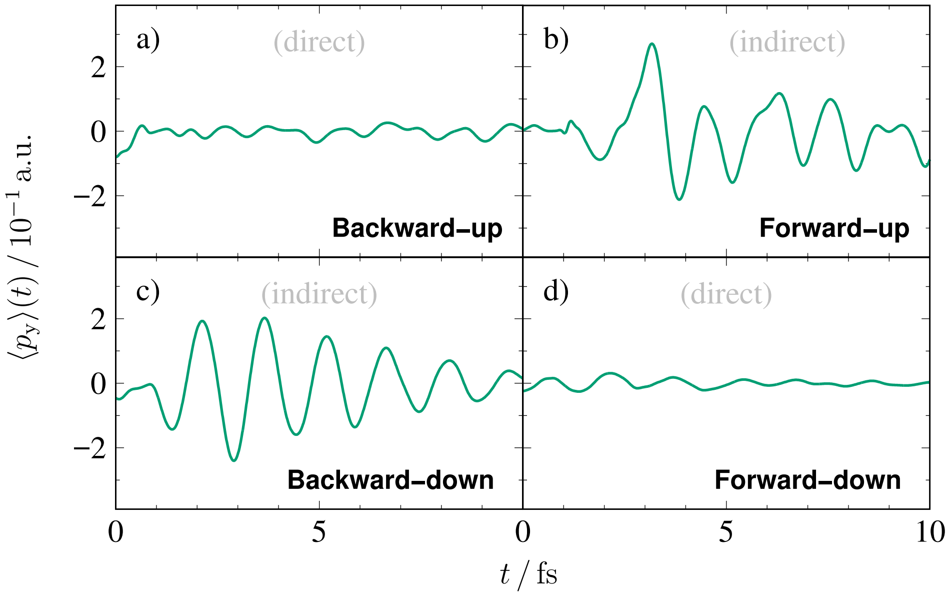

Figure 4.7. Time-resolved momentum expectation value $\langle p_\mathrm{y} \rangle(t)$ of the remaining y electron after ionization of the full system for the a) *backward-up* channel, b) *forward-up* channel, c) *backward-down* channel, and d) *forward-down* channel. The expectation value $\langle p_\mathrm{y} \rangle(t)$ of the remaining y electron serves as an indicator for electron scattering during the emission process. For the *forward-down* and *backward-up* channels, direct ionization processes do not involve electron-electron scattering and therefore show only weak dynamics. For the *forward-up* and *backward-down* channels, considerable scattering between the electrons occurs and therefore the remaining electron performs significant oscillations after the emission event.

the last section (4.1.3), a change of the carrier-envelope phase of the ionizing field by π bears almost no difference in the results. Consequently, all *forward/backward* asymmetries do not originate in the CEP of the electric field, but can be traced back to the asymmetric molecular geometry defined by the chosen initial conditions.

Inspecting the individual channels, Fig. 4.7a and d show only weak induced dynamics, while panels b and c exhibit clear oscillatory behaviour. These trends can be classified as "direct" and "indirect" emission with an interpretation as follows: In the *forward-down* channel, Fig. 4.7d, signal originates primarily from the emission of the weakly bound electron initially located on the molecule's right-hand side. During ionization, it is accelerated towards large x values and only passes the fixed right nucleus, and as such hardly affects the strongly bound electron at the molecule's other end. Therefore, this "direct" emission, where almost no interaction with the parent ion occurs, induces dynamics far weaker compared to the case of “indirect” emission.

The situation is similar for the *backward-up* channel, Fig. 4.7a, where it is the strongly bound electron, which gets accelerated towards large negative values in x and only scattering with the fixed left nucleus occurs. The remaining weakly bound electron on the other side of the molecule shows only a minor response, as barely any interaction took place. Note, however, that the average momentum $\langle p_{\mathrm{y}} \rangle^S(t)$ of the *backward-up* channel – although small – displays a more irregular dynamics than the *forward-down* channel. The origin of this is the induced nuclear dynamics of more than one electronic state, further investigated in section 4.3.2.

Looking at Fig. 4.7c, the *backward-down* channel displays a strong oscillatory behaviour starting 1 fs after the system interacts with the ionizing field. In this scenario, signal stems primarily from the weakly bound electron on the molecule’s right-hand side. However, in contrast to the *forward-down* channel, the emitted electron first passes the entire parent ion before reaching large negative spatial values[3]. Inelastic scattering with the strongly bound electron induces dynamics with the residual y electron remaining confined between the two left nuclei, resulting in a clean oscillatory dynamics. A Fourier analysis of this oscillatory between 0 and 10 fs reveals a periodicity of 1.47 fs, corresponding to an energy of approximately 2.8 eV, see Fig. 4.8. This matches with the energy gap of the electronic ground and first excited state of the one-electron system, thus indicating an excitation of an electronic wave packet in the residual cation.

Ionization leading to signal in the *forward-up* channel, Fig. 4.7b, relates to the strongly bound electron passing its parent ion before being emitted towards large positive x values and inelastically scattering with the weakly bound electron on the molecule’s right-hand side. Consequently, oscillatory dynamics are induced. As for the *backward-up* channel, Fig. 4.7a, nuclear dynamics is initiated, which further contribute to the total dynamics.

Lastly, note that the total amount of emitted electronic density varies heavily for the different channels: While total signal varies over time, at $t = 10$ fs the probability of emission in *backward* direction is almost equal for the *down* and *up* channels with a ratio of 3:2 (*down:up*). In *forward* direction, however, emission into the *down* channel strongly dominates over the *up* channel by a factor of 10.

---

[3] The point can be made, that this type of ionization is not “not direct”. However, to contrast it from the clearly “direct” emission process, the label “indirect” is assigned.

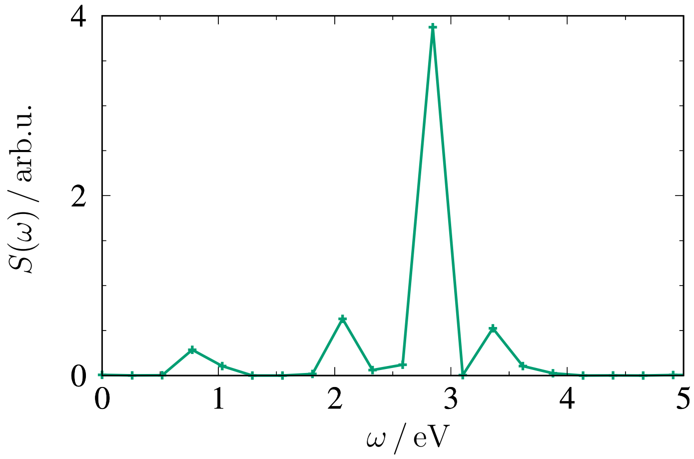

Figure 4.8. Energy spectral density $S(\omega) = |\mathcal{F}\langle p_y \rangle(t)|^2$ for the first 10 fs after ionization into the *backward-down* channel. The frequency of the oscillation matches with the energy gap of the ground and first excited state of the one-electron system.

4.3 Subsystem Ionization

The analysis of the previous chapter provided a first intuitive picture of the intramolecular scattering effects occurring in the full fermionic system during ionization. However, as the interacting electrons are indistinguishable the roles of emitted and remaining electrons during the scattering process cannot clearly be identified. To this end, the artificially truncated wave functions ψ_A and ψ_B, see Eqs. (4.3a) and (4.3b), are employed as initial conditions, thus rendering the two electrons distinguishable, see Sec. 4.1.2. This way, electron-electron correlation originating from the antisymmetry of the wave function and interference effects between the two distinct initial density distributions (localized near $x = \pm 5\,\text{Å}$ & $y = \mp 5\,\text{Å}$) are neglected. Fig. 4.9 compares the integrated ionization density of the full fermionic system to the sum of the subsystems A and B for the *forward* and *backward* directions. The good agreement in shape indicates that for the present system the neglected correlation effects are of minor importance in terms of total ionization, however, not necessarily negligible for the structure of emission.

Interpretation in 1D and 2D

While the employed model system is linear and can be visualized as pearls on a string, the antisymmetry property of the wave functions requires description in a two-dimensional plane. As of this, it is beneficial to consider the investigated processes always in these two pictures. To this end, in the following schematics

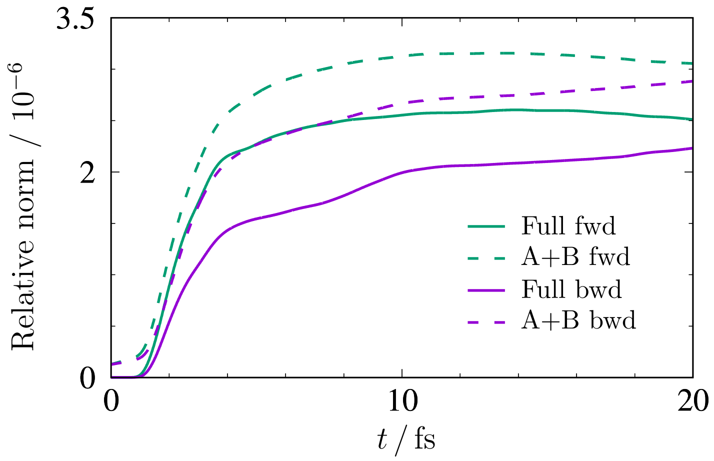

Figure 4.9. Integrated ionization signal of the full fermionic system (solid lines) and the summed signal of the two subsystems A & B (dashed lines). Green color indicates emission signal into the *forward* direction, while purple represents emission into the *backward* direction.

will illustrate the same processes twice – once in the one-dimensional coordinate space, and once in the x, y-configuration space representation.

4.3.1 Process Classification

Fig. 4.10 shows the time-dependent 2D electronic densities of the full system with two indistinguishable electrons (upper part) and the subsystems A (middle part) and B (lower part), in which electrons can be distinguished, for an area corresponding to the emission of electron x in *backward* (left panels) and *forward* direction (right panels), while electron y remains bound to the parent ion. Above the two lower panels, a schematic picture indicates different underlying processes (blue/green arrows) in the x, y-configuration space (left) and the one-dimensional coordinate space (right). The thick blue arrows correspond to the four main contributions discussed in Sec. 4.2.2, where either the strongly (A) or the weakly bound electron (B) is released to either side of the molecule.

At 1 fs after ionization, only the fastest part of the electron wave packet released from the molecule's side pointing towards the emission direction have reached the evaluation region at 25 Å. For this part, the remaining y electron stays in its initial position on the opposite side of the molecule (blue arrows, A: *backward-up*; B: *forward-down*). At 2 fs strong additional signals from the remote side of the molecule arise for an emission into the opposite direction (blue arrows, A: *forward-up*, B: *backward-down*). Here, another signal with a smaller but still significant probability appears in the *down* (A) channels and – to a smaller extent – in the *up* (B) channels. In these channels, the remaining y electron

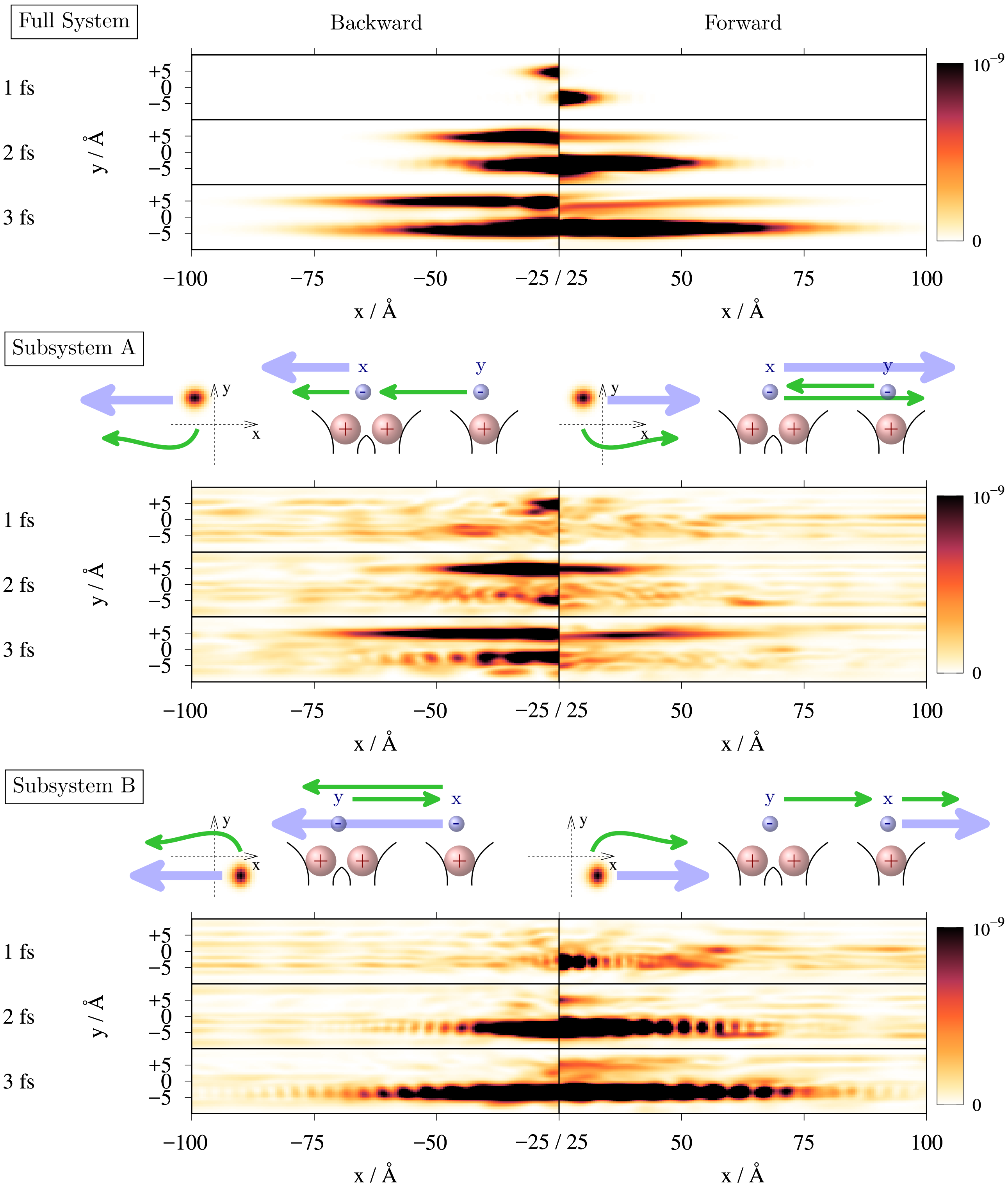

Figure 4.10. Snapshots of the integrated 2D electronic density $\int |\Psi(x,y,R,t)|^2 \,\mathrm{d}R$ at $t = 1$, 2, and 3 fs after ionization of the full system (top panel) and the two subsystems, ψ_A (middle panel) and ψ_B (bottom panel), with headers illustrating the ionization process (2D view of initial density distribution in the configuration space and 1D view in the real coordinate space). Source: Ref. [135]

is localized in regions which were originally occupied by the x electron (green arrows).

Furthermore, two features distinguish subsystems A and B from the full system: (i.) Minor background signal can be seen throughout the evaluation region, even at $t = 1\,\mathrm{fs}$ at large values of $|x|$, and (ii.) all *down* pathways of the subsystems exhibit a periodically structured pattern within the ionization signal. Both effects – which are absent in the full model – are attributed to the abrupt truncation of the subsystems' wave functions at the $x{=}y$-diagonal discussed in Sec. 4.2.1. However, both effects show only a minor impact on the observables discussed in this analysis and are therefore not included in the following discussion.

Comparing the overall intensities, a *forward*/*backward* asymmetry can be observed in both subsystems. It is most pronounced (with a ratio of up to three), when the strongly bound electron is emitted (electron x in subsystem A) and electron y remains at the weakly bound side (*up*-channel). This indicates a strong impact of intramolecular electron-electron scattering with the weakly bound electrons reducing the electron density emitted in the *forward* direction. In the case of the weakly bound electron being emitted (electron x in subsystem B, *down* channels), a ratio of up to two between the intensities of the *forward* and the *backward* channel is found. Comparing the overall intensities of the direct emission pathways, i.e. where intramolecular scattering is negligible, of both subsystems with respect to each other, it can be seen that the emission of the weakly bound electron (B, *forward-down*) is approximately two to three times more likely than that of the strongly bound electron (A, *backward-up*).

The four dominant contributions (blue arrows) are those, for which the x electron is emitted and the y electron stays where it was initially positioned. In addition, for both subsystems, A and B, electronic densities also increase at values of the y coordinate (*up*/*down*), that were initially vacant. This is traced back to secondary processes (green arrows), where the remaining electron y switches sides. Yet, it is not clear from Fig. 4.10 whether this y motion precedes or follows the emission of electron x.

This question is addressed in the following section, 4.3.2, by further dissecting the ionization pathways through restricting the electrons' interaction with the electric field. It is emphasized that in particular in the case of *backward* emission of the strongly bound electron in subsystem A, these secondary contributions reach an intensity within the same order of magnitude of the primary processes and therefore contribute significantly to the overall ionization signal.

4.3.2 Restricted Electron-field Interaction

This sections investigates the intramolecular dynamics during and after the electron emission process for the subsystems A and B, i.e. using distinguishable electrons, by limiting the interaction of the electromagnetic field to either the x or the y electron. For this, the system's total Hamiltonian $\hat{\mathcal{H}}(t)$ from Eq. (1.69) is truncated by dropping of one of the field-electron interactions terms, resulting in a modified Hamiltonian $\hat{\mathcal{H}}'(t)$ as

$$\begin{aligned}\mathcal{H}'(t) &= \frac{P_{\mathrm{R}}{}^2}{2M} + \frac{p_{\mathrm{x}}^2}{2m_e} + \frac{p_{\mathrm{y}}^2}{2m_e} + V(x,y,R) \\ &\quad + e\,A(t)\left(-\frac{Z}{M}P_{\mathrm{R}} + \frac{p_{\xi}}{m_{\mathrm{e}}}\right), \end{aligned} \tag{4.9}$$

where $\xi \in \{x, y\}$ refers to *either* the x *or* the y electron. This restriction allows identification of different effects due to electron-electron interaction during photoionization.

In contrast to the previous sections, where the 2D electronic density and the instantaneous average momentum were utilized for analysis, the electronic state of the remaining bound y electron will be investigated here. To this end, the ionization wave function $\psi^{S}_{\mathrm{out}}(x, y, R, t)$, i.e. the part of the wave function entering the different analysis regions defined via the mask function $c(x, y)$ and subsequent separation into *forward/backward* channels (Sec. 4.2.1) is projected onto the set of eigenfunctions $\{\varphi^{1\mathrm{e}}_n(y; R)\}, n \in \{0, \ldots, 3\}$ of the one-electron model, obtained via imaginary time propagation (Sec. 1.1.4). The relative population $P_n(t)$ of the nth state by the y electron ($n = 0$ corresponds to the ground state), is calculated as

$$P_n(t) = \iint \left| \int \varphi^{1\mathrm{e}}_n(y; R)\, \psi^{S}_{\mathrm{out}}(x, y, R, t)\ \mathrm{d}y \right|^2 \mathrm{d}x\ \mathrm{d}R, \tag{4.10}$$

where the domain S no longer separates between *up* and *down* channels, but only *forward* and *backward* direction as the eigenstates are defined over the entire coordinate space. Thus, $P_n(t)$ is the absolute population of the single-electron state n in the molecular cation after photoionization.

Fig. 4.11 shows the first four electronic eigenstates of the single-electron system for the nuclear geometry chosen to initiate propagation. As the initial state was setup to induce a minimum of vibrational dynamics, this geometry persists until interaction with the ionizing field. Calculating the relative population $P_n(t)$, it is these states onto which is projected as opposed to the two-electron eigenstates $\varphi^{2\mathrm{e}}_n(x, y; R_0)$.

As can be seen, the electronic ground and first excited state, i.e. the two lowest states, have their highest probability density at negative y coordinates and being located between the two left-hand side nuclei corresponding to the strongly

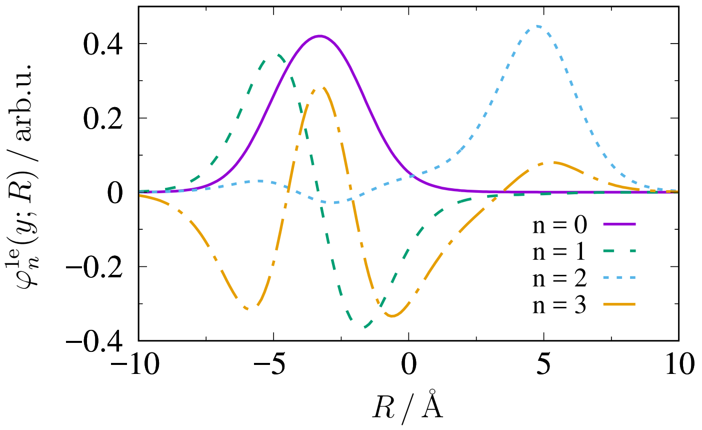

Figure 4.11. First four electronic eigenfunctions of the single-electron system at the initial, near-equilibrium nuclear geometry, $\varphi_n^{1e}(y; R_0)$. The corresponding potential energy surfaces, $V_n^{1e}(R)$, can be seen in Fig. 4.2.

bound electron. While the third excited state shows similar distributions between the positions outside of the fixed left nucleus, in between the two left nuclei, or close to the molecular center, the second excited state is located primarily on the molecule's right-hand end corresponding to the site of the weakly bound electron.

The populations after ionization are shown in Fig. 4.12 in *backward* (left panels, $x < 0$) and *forward* direction (right panels, $x > 0$) for the fully antisymmetric wave function (top panels, a and b) and the subsystems A and B as indicated (lower panels, c–h). The schematics next to the panels indicate the dominant ionization pathways. Note that the initial increase in Fig. 4.12 does not reflect the population evolution of the remaining electron, but is caused by the fact that the x electron enters the designated evaluation areas only after about 3 fs. The shaded areas illustrate the spurious background signal that is even obtained in field-free simulations due to the imperfect initial conditions.

Several processes can be identified. First the case is considered, in which the electron interacting with the electric field results in the emission of the very same electron (Fig. 4.12c–f). The strongest signal (panel f) corresponds to the emission of the weaker bound electron (subsystem B) in *forward* direction, i.e. away from the molecule. In this case, the stronger bound electron remains almost unaffected in its position located at the left-hand side, corresponding to the electronic ground state of the cation, $n = 0$ (see Fig. 4.11). Emitting the weaker bound electron in the opposite direction, Fig. 4.12e, such that inelastic scattering with the remaining strongly-bound electron occurs, entails a significant population of the first excited single-electron state[4], $n = 1$. This interaction corresponds to an intramolecular *shake-up* process.

A different situation is encountered, when the stronger bound electron (Fig. 4.12, panels c and d) interacts with the electric field and is ultimately emitted. If the electron emission occurs in the *backward* direction, Fig. 4.12c, the weaker bound electron remains initially in its place, corresponding to the second excited state, $n = 2$, which is localized on the molecule's right-hand side (see Fig. 4.11). In the *forward* direction, Fig. 4.12d, the second excited state is dominant too, but a slight increase in the population of the cation ground state, $n = 0$, above background signal levels (shaded areas) can be noted. Therefore, inelastic intramolecular scattering with the weaker bound electron must have taken place, resulting in a *shake-down* process during the electron emission from lower energy levels. Note, that the population change due to the shake-down is much lower than in the shake-up process discussed above. This is attributed to the additional process of the y electron having to switch sides, which might be further suppressed by excluding field-interaction with it.

After $t \gtrsim 15\,\mathrm{fs}$, a population decrease of the second excited state, $P_2(t)$, with a simultaneous increase in the first excited state, $P_1(t)$, can be seen for the case of the x electron being emitted from the strongly bound state (subsystem A, Fig. 4.12c and d), which is not present for the weakly bound state (subsystem B, Fig. 4.12e and f). This time-dependent feature can be traced back to the non-adiabatic nuclear reorganization dynamics induced by the ionization process. To verify this hypothesis, additional simulations have been performed with a nuclear geometry frozen at $R = R_0$, which are shown as dotted lines in Fig. 4.12c–h[5]. Here, such a population exchange does not occur and must therefore be a consequence of correlated non-adiabatic electron-nuclear dynamics in the cation. The potential energy surface of the second state, $V_2^{1\mathrm{e}}(R)$, see Fig. 4.2 middle panel, shows a large gradient towards the molecular center ($R = 0$), where an avoided crossing with the first excited state, $V_1^{1\mathrm{e}}(R)$, is found. Thus, upon ionization, nuclear dynamics is initiated, driving the system via non-adiabatic transition from the second to the first electronically excited state, $V_2^{1\mathrm{e}}(R) \longrightarrow V_1^{1\mathrm{e}}(R)$.

The induced nuclear geometry change is accompanied by a variation of the potential energy surface difference between the $n = 2$ state and lower states. This induced nuclear dynamics causes the instantaneous average electronic momentum $\langle p_{\mathrm{y}} \rangle(t)$ in the *forward-up* channel, Fig. 4.7b (which mainly originates in

---

[4] Recall, that the first excited state is still localized on the left-hand side of the molecule.

[5] Propagation with a frozen nuclear geometry is achieved by omitted every term from the Hamiltonian $\hat{\mathcal{H}}(t)$, which contains the nuclear momentum. Additionally, the initial wave packet is no longer described by a nuclear Gaussian wave packet, but by its central coordinate R_0 alone.

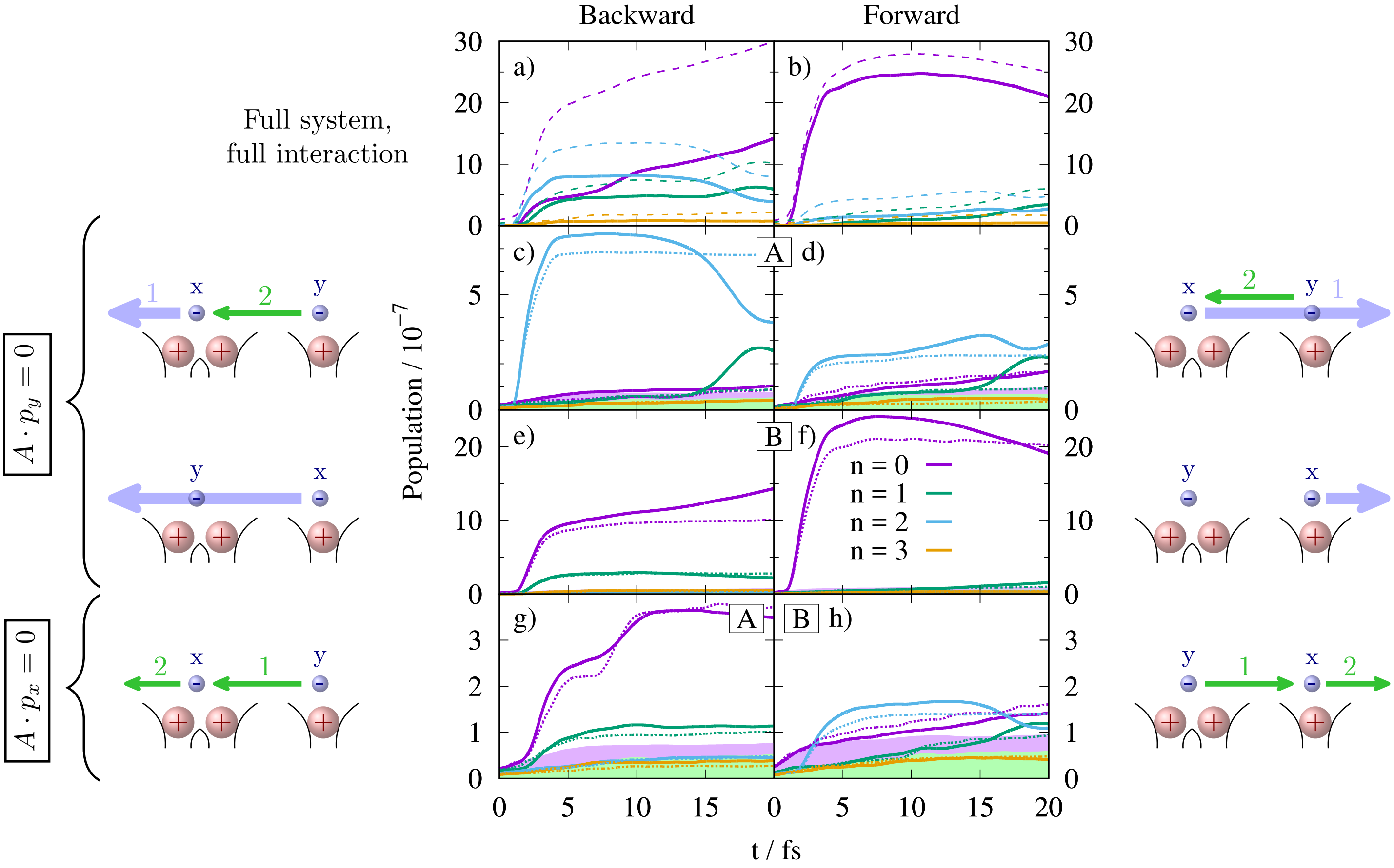

Figure 4.12. Population evolution of the electronic states occupied by the remaining bound y-electron calculated via Eq. (4.10), after the XUV pulse ionizes the two-electron system at $t = 0$ fs. The upper panels, (a) and (b), contain the dynamics of the full antisymmetric system, whereas lower panels, (d)–(h), show the dynamics of distinguishable electrons selectively interacting with the electric field as indicated. Such modifications allow for the identification of different ionization pathways. In particular, some pathways involve inelastic intramolecular scattering leading to shake-up, panel (e), and shake-down, panel (d), processes, whereas other relevant pathways involve elastic scattering, (g) and (h), preceding the electron emission. Dashed lines in panels (a) and (b) correspond to the sum of all individual pathways with restricted field interaction displayed throughout panels (c)–(h). The dotted lines in panels (c)–(h) represent evolution for a molecule with fixed core position. Shaded areas correspond to the dominating background signal, i.e. from the single-electron ground and first excited state, for field-free propagation. These signals are not visible in all panels due to their rather low amplitude. Source: Ref. [135]

the process illustrated in Fig. 4.12d) to show more complex oscillations than its counterpart in the *backward-down* direction, Fig. 4.7c (primarily originating in Fig. 4.12e) with only negligible nuclear dynamics.

Finally, the lowest panels, Fig. 4.12g and h, correspond to purely correlation-driven processes, in which the energy provided by the electric field is absorbed by electron y, but results eventually in the emission of electron x. Therefore, a nearly elastic collision between the two electrons must have occurred, in which the absorbing electron transfers most of its acquired kinetic energy to the electron originally unaffected by the field. The initially accelerated electron then takes the place of the subsequently emitted electron – similar to colliding billiard balls. Consequently, the resulting populations of the single-electron states of the remaining electron shown in panel g for subsystem A are very different from the ones in panel c, although ultimately the same electron is ejected. Instead, due to the originally accelerated electron (y) replacing the emitted one (x) during the ionization process, the population evolution of the parent ion strongly resembles the one of subsystem B, seen in panel e, where the residual electron is located at the strongly bound side.

The same applies for subsystem B's elastic collision process, panel h, which rather resembles the populations found in A's inelastic collision, panel d. Again, this is traced back to the accelerated y electron taking x's place *prior* to the emission. Note that population of $P_0(t)$ and $P_1(t)$ through elastic collision in subsystem A, Fig. 4.12g, corresponds to population of the (previously unoccupied) *down* channel, cf. Fig. 4.10 (green arrows). This happens immediately upon interaction with the XUV pulse. In contrast, the competing process, in which electron x is emitted first *followed* by electron y being attracted by the higher positive charge density, Fig. 4.12c, does not contribute to subsystem A's *down* channel before $t \approx 15$ fs. Only then, the first excited state state, $V_1^{1\mathrm{e}}(R)$, becomes populated via a non-adiabatic transition, which is accompanied by a density transfer of the remaining y electron to the left-hand side with $y < 0$. It is therefore concluded, that the strong early signals, seen in the subsystem A *backward-down* channel, correspond to the elastic collision process preceding the x electron's emission. The significant contribution of this pathway, which predominantly yields population of the $n = 2$ state, to the full system's ionization signal in *backward* direction can be clearly seen in Fig. 4.12a.

Similar, but with reversed roles, is the situation when the strongly bound electron (y, panel h) is accelerated towards the weakly bound one (x): Through elastic collision, the y electron takes the x electron's place preceding the emission process, where it is in the second excited eigenstate with the potential $V_2^{1\mathrm{e}}(R)$. This process thus contributes temporarily to subsystem B's *forward-up* channel, see Fig. 4.10. Having the electronically second excited state populated, again, nuclear dynamics is initiated, resulting in a non-adiabatic transition. Therefore, parts of the population of the second excited state $\varphi_2^{1e}(y;R)$ (being localized at positive y values) are transferred to the first excited state $\varphi_1^{1e}(y;R)$ (being localized at negative y values) via an avoided crossing, so that their density is then observable in subsystem B's *forward-down* channel[6].

It is emphasized that the amplitude of such secondary processes appears to be nearly of the same order of magnitude compared to the primary processes discussed above.

To summarize, this artificial decomposition into individual processes allows to analyze and identify processes underlying the full system's ionization. Comparing the cases of the fully antisymmetric initial wave function without any restrictions on the electric-field interaction, Fig. 4.12a and b (solid lines), with the artificially restricted subsystems (dashed lines, corresponding to the sum of all individual pathways with restricted field interaction), shows a very good qualitative agreement supporting the validity of the employed decompositional approach. In particular, the overall time-dependent behavior is very well reproduced by the subsystems' dynamics with restricted field-interaction. For example, in the *backward* direction, Fig. 4.12a, the population of the second excited state and its non-adiabatic transition for $t \approx 15\,\text{fs}$ can be traced back to the electronic shake-up process and the motion of the mobile nucleus (panel c). Also the step-like increase ($t \sim 8\,\text{fs}$) of the ground state can be traced back to the population increase (of the ground state) in panel g and its further continuous increase at times $t > 10\,\text{fs}$ in panel e, which are not accompanied by a shake-up process.. Note, that the superposition of the subsystems A & B with respect to the exciting fields employed above is not exact: Discrepancies, in particular in the overall amplitude, are most likely related to the omission of interference effects between emitted density from the two initial localized electronic density distributions, which have been dropped by regarding electrons as distinguishable particles. Further investigations of such influences remain for future research endeavors.

To conclude, the final state of the molecular parent ion after ionization depends strongly on the specific ionization pathway, may it involve elastic or inelastic intramolecular scattering events prior to the electron emission. Furthermore, it was shown that electron-electron correlations significantly contribute to the total ionization probability for both, primary and secondary processes. In particular, quantifying the effect of secondary processes on the same magnitude as primary processes, underlines the inaccuracy of the commonly applied single

---

[6] For the sake of completeness, it is noted that the cases not shown, in which the emission of the second electron takes place in the opposite direction of panels g and h, are of similar shape and magnitude.

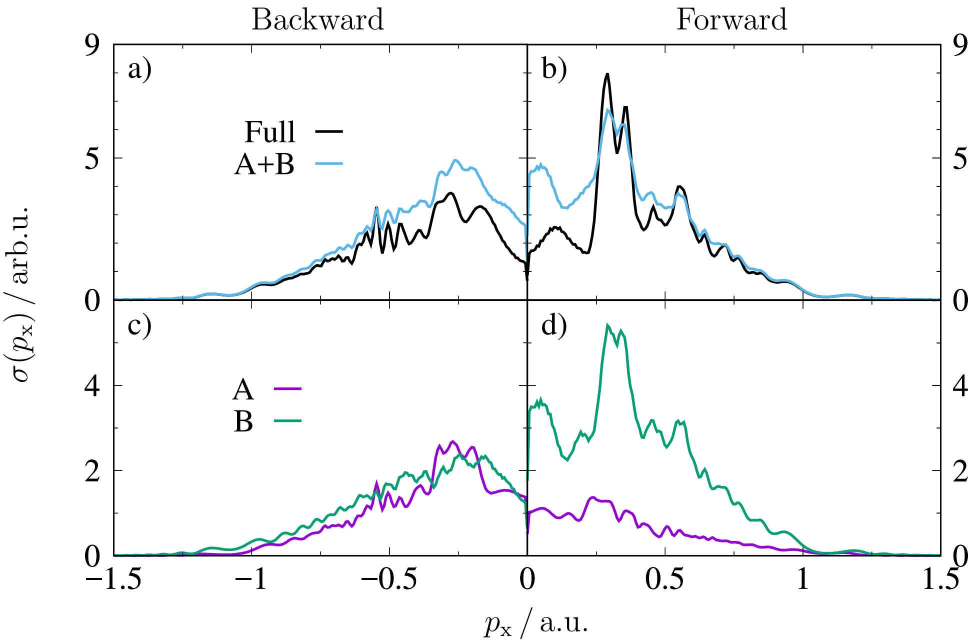

Figure 4.13. Momentum distribution $\sigma(p_\mathrm{x})$ of the emitted electron at $t = 10$ fs. Top panels: Full antisymmetric system and sum of subsystems A and B in *backward* (a) and *forward* (b) direction. Bottom panels: Subsystems A and B in *backward* (c) and *forward* (d) direction. Within the subsystems, direct emission involving negligible scattering leads to peaked structures at momenta below 0.7 a.u., whereas indirect emission results in a smoother momentum distribution.

active electron approximation especially in the context of single-photon ionization of molecules.

4.4 Traces in the Photoelectron Momentum Distribution

Lastly, it is investigated to what extent the different ionization processes are represented in the final momentum distribution of the the photoelectron. To this end, the momentum distribution $\sigma(p_\mathrm{x})$ of the emitted electron (x) is calculated within the evaluation region S as

$$\sigma(p_\mathrm{x}) = \iint \left|\widetilde{\psi}^{S}_{\mathrm{out}}(p_\mathrm{x}, p_\mathrm{y}, P_\mathrm{R}, t = 10\,\mathrm{fs})\right|^2 \mathrm{d}p_\mathrm{y}\ \mathrm{d}P_\mathrm{R}, \tag{4.11}$$

where $\widetilde{\psi}^{S}_{\mathrm{out}}$ is the Fourier transformed single ionization wave function ψ^{S}_{out}. Note that in *forward* (*backward*) direction, emission occurs only at positive (negative) values of p_x. At $t = 10\,$fs, the distribution functions $\sigma(p_\mathrm{x})$ are mostly converged within the respective evaluation region and only weak contributions continue to enter the evaluation region afterwards.

The calculated momentum distributions are shown for the full system and the sum of subsystems A and B in *forward* and *backward* direction in Fig. 4.13a and b, respectively, as well as for the subsystems, A and B, in Fig. 4.13c and d. The *forward*/*backward* asymmetry can be seen in all cases. Intensity differences are traced back to two trends: First, the direct emission, i.e. emission without intramolecular scattering (A: *backward*, B: *forward*), has a larger intensity than signals, where the photoelectron passes the parent ion prior to emission (A: *forward*, B: *backward*); and second, the weaker x electron binding energy in subsystem B leads to a larger ionization yield than obtained for subsystem A, in which the x electron is strongly bound. The combination of both effects leads to an almost equal contribution of the two subsystems to the *backward* emission, Fig. 4.13c, whereas in the *forward* direction, Fig. 4.13d, the intensity of subsystem B's direct emission signal clearly exceeds subsystem A's contributions.

It is noteworthy, that the contributions originating in direct emission show a peak structure at lower momenta (predominantly around (A) $p_\mathrm{x} = -0.25\,\mathrm{a.u.}$ and (B) $p_\mathrm{x} = 0.3\,\mathrm{a.u.}$), whereas pathways that involve intramolecular scattering processes yield only a weakly structured, smoother momentum distribution.

The stronger pronounced peak structure in the momentum distribution of the full system's *forward* emission, Fig. 4.13b, therefore reflects the much larger contribution of direct emission processes into this direction. The smoother distribution of the *backward* emission, Fig. 4.13a, on the other hand, indicates an increased contribution of pathways with significant intramolecular scattering to the emission.

Lastly, the comparison of the full system with the sum of the subsystems, Fig. 4.13a and b, reveals the effect of omitting interference effects between the emitted density from the two initial localized electronic density distributions. While the agreement is good for large positive and negative momenta, a general overestimation of the subsystems' sum is noted for low negative momenta. For low positive momenta, however, only the peak structure stemming from subsystem B matches well with the full system. In the range of $p_\mathrm{x} \in [0, 0.25]\,\mathrm{a.u.}$ the sum of the subsystems even exhibits a shift to lower momenta while displaying a larger signal at the same time.

To summarize, the different shapes of the momentum distribution generated by an ultrashort XUV pulse bears information about the occurrence of intramolecular scattering events accompanying the different ionization processes. Note, however, that the magnitude of these differences correlates with the difference in binding energy of the involved electrons. It is likely, that smaller energy gaps between electronic binding energies as encountered in, e.g. molecules with considerably more electrons, may lead to a reduction of the pronounced effects found here.

4.5 Discussion

In this chapter, the correlated electron-electron and electron-nuclear dynamics in a linear molecular charge-transfer model were studied by solving the time-dependent Schrödinger equation numerically for two electronic and one nuclear degree of freedom in one dimension each. To this end, the ionization of a single electron by an attosecond XUV pulse was considered, and the exact scattering mechanism traced back to the electron's interaction with the residual cation, in particular with the remaining bound electron. The momentum distribution of the remaining bound electron was used to study the different pathways of scattering.

By replacing the fully antisymmetric wave function with one of distinguishable electrons and in a second step, additionally limiting interaction with the ionizing field to a single electron, the contributions of primary and secondary processes to the total emission signal were analyzed. Using this approach, time-dependent signatures in the evolution of the molecular parent ion were identified and traced back to various intramolecular scattering events preceding the electron emission. It was found, that these pathways exhibit different signatures in the photoelectron's final momentum distribution.

Employing two electronic degrees of freedom, significant contributions of static and dynamic correlations on an attosecond timescale within the single-photon ionization process were identified, which lies beyond the scope of the commonly applied single active electron approximation. In particular, relevant pathways to the overall signal were isolated, in which inelastic scattering with partial momentum transfer between the electrons resulted in shake-up and shake-down phenomena. Additional pathways of significant contribution involving elastic scattering were found, where the electron originally accelerated by the electric field transfers its momentum to a different electron within the molecule and takes its place instead. Furthermore, it was shown that different ionization pathways leave the parent molecular ion in different electronic states. As a consequence, correlated electron-nuclear reorganization dynamics is induced, which was shown by the example of non-adiabatic transitions following the ionization process.

It is presumed, that the observations made here for a model system are representative for molecular systems, and, consequently, that both static and dynamical correlations contribute significantly to the ionization processes through various pathways beyond the single active electron picture.

SUMMARY

The scope of this thesis covered two subjects within the framework of ultrafast correlated particle dynamics: In the first part, asymmetries within the photoelectron spectra were investigated for a system dominated by electron-nuclear correlations, while the second part focused on electron-electron interactions. For the former, a detailed analysis of an ionizing pulse provided access into the dynamics occurring before ionization, whereas for the latter, an investigation of the precise ionization mechanisms gave insights into the dynamics during and after ionization. Hereby, the results are beyond the commonly applied single-active electron approximation.
In order to investigate the electron-nuclar correlation dynamics, the time-dependent Schrödinger equation was solved numerically, including both, the electronic and nuclear degree of freedom directely. The underlying model system has been introduced by Shin & Metiu in order to investigate charge-transfer processes. Here, an infrared pulse was employed to pump the system, while an ultrashort XUV pulse probes the induced dynamics at various times. The obtained photoelectron spectrum exhibited an asymmetry for the different emission directions of the electron, which could be utilized to unravel the system's correlated dynamics.
Calculations were performed for two distinct cases: one dominated by adiabatic dynamics, where electronic motion adjusts adiabatically to changes in the nuclear geometry, the other described by dynamics of pronounced non-adiabatic transitions to neighbouring electronic states. In the case of the adiabatic system, it was illustrated that the photoelectron asymmetry accurately reflects the electronic motion prior to emission in the absence, as well as in the presence of an external perturbing IR-field. For the diabatic system, the asymmetry was found to depict specifically the moments of non-adiabatic transitions, however, not electronic motion during other times.
The assumption was made that the electron dynamics visible within the photoelectron spectrum are caused by two things: the naturally occurring dynamics, described by the system's internal forces, and the dynamics induced by the external IR-field. To validate this theory, two sets of calculations with pulses shifted by a phase of π were performed separately, and a technique for reconstructing the unperturbed electron dynamics proposed. It was proven that the asymmetries of both calculations vary in the contributions from the induced dynamics, however, not in the contributions stemming from the dynamics intrinsic

to the system. As such IR-fields can be applied to efficiently increase the signal of the photoelectron asymmetry, while the ability to access the unperturbed dynamics is retained. Furthermore, it was shown that the reconstruction technique starts to break down once the field strength of the perturbing IR-field reaches levels that induce significant population transfers between the electronic states, and as such initiate new intrinsic dynamics.

To identify the properties of the ionizing XUV pulse, which yield the largest asymmetry, the employed system was further configured as a superposition of two neighbouring electronic states, as these exhibit fast oscillations within the electronic momentum. Temporally short XUV pulses were found to considerably increase the measured asymmetries, as less optical cycles within the pulse mean a temporally more compressed interaction, and hence a better reproduction of the correlated dynamics. Additionally, investigation of the frequency of the ionizing pulse revealed that photon energies closely above the ionization threshold lead to considerably larger yields in the asymmetry, as the transition probability to higher continuum states gets significantly reduced.

To summarize, in the first part of this thesis, the asymmetry within the photoelectron spectrum was closely examined and found to carry the system's information on the correlated electron-nuclear dynamics even when perturbed by an external IR-field. Moreover, by utilizing two phase-shifted pulses it was demonstrated possible to access the precise dynamics naturally occurring within a molecular system.

The second part of this thesis covered the extension of the previous system by an additional electronic degree of freedom, and as such enabled the investigation of electron-electron correlations, here, with a focus on electron dynamics during and after photoionization of a single electron with an attosecond XUV pulse. By solving the system's time evolution exactly, this approach distinguishes itself from other techniques which heavily rely on approximations such as, for example, the Born-Oppenheimer approximation or the single-active electron approximation. Especially the latter neglects any electronic correlations effects, but assumes that electrons and nuclei screen each other to a large degree. Consequently the presented results stand in direct contrast to it and illustrate a much more precise picture.

The investigation concentrated on vibrational dynamics initiated in an equilibrium state, i.e. in one of two equal potential wells, so that the dynamics intrinsic to the system were kept to a minimum. This nuclear orientation caused one of the electrons to be bound weaker, while the other was bound stronger, which, in turn, altered how each of the electrons interacts with an ionizing XUV pulse. As electrons are fermionic particles, and as such indistinguishable from each other, the wave function employed to describe the system is symmetric in the electronic coordinates, which made statements about the electronic origin of any measured ionization signal impossible. To identify the origin of the signal and distinguish the weakly from the strongly bound electron, artificial subsystems of desymmetrized initial wave functions were examined alongside the fully fermionic system.

The conducted analysis revealed a fundamental dependence of the ionization pathway on the position of the electron remaining bound, and on the direction of the electron that was emitted. The momentum of the residual electron was identified to deviate for the different pathways of ionization, so that two cases could be isolated: one, where electron emission occurred directly and without scattering with the other electron, resulting in barely any induced dynamics of the residual electron, and two, where elastic and inelastic scattering took place and left the remaining electron in several excited states.

Investigation of the artificial subsystems futher revealed that there is no preferred emission pathway for the weakly bound electron, while for the strongly bound electron “direct” emission, i.e. emission not involving electron-electron scattering, is significantly more likely. Furthermore, emission of the strongly bound electron did exhibit much more irregular scattering interaction with the other electron, giving rise to the question, whether the interaction originated in the ionization, or the ionization originated in the interaction with the other electron (stimulated by the XUV pulse). The former situation would correspond to inelastic scattering leaving the weakly bound electron in an excited state, the latter, on the other hand, to elastic scattering ultimately leading to the emission of the weakly bound electron (while the formerly strongly bound electron takes its place).

To further unravel the exact ionization mechanism, the interaction with the electric field of the ionizing pulse was artificially restricted to a single electron, and the electronic state of the residual electron examined. Emission of the weakly bound electron was found to leave the residual electron in its electronic ground state, regardless of scattering events taking place or not. Consequently, neither was a nuclear reorganization dynamics initiated. In contrast, the emission of the stronger bound electron led to a shake-up of the residual electron, which, in turn, resulted in the onset of nuclear reorganization dynamics accompanied by non-adiabatic transitions between electronic states. To verify the nuclear dynamics as origin of the subsequent population transfers, simulations with a frozen nuclear geometry were performed, resulting in a suppression of the electronic transitions and confirming the assumption.

By limiting the field-particle interaction to the electron which was ultimately not emitted, the amount of ionization signal caused by elastic scattering was isolated, and as such shedding light on the accuracy of the single-active electron approximation. While the total ionization was reduced by one order of magnitude for the weakly bound electron, the amount for the strongly bound electron was on an equal level, thereby highlighting the significance of electron-electron correlations during ionization events. A second observation within the elastic scattering process was an alteration in the electronic composition of the residual electron, which was characterized by shake-up processes for the emission of the weakly bound electron, and no shake-up processes for the strongly bound electron – so directly opposite to the situation discussed before.

Lastly, the photoelectron's momentum distribution was investigated with respect to the features of the individual ionization processes, which showed good agreement with the separational approach of the artificial subsystems.

To conclude, the second part of the presented thesis employed two electronic degrees of freedom in order to study electron-electron correlations during events of single-ionization induced by interaction with an attosecond XUV pulse. By employing artificial subsystems of desymmetrized electronic coordinates, the different ionization pathways occurring within the full fermionic system were thoroughly investigated. As a key result, it was highlighted that the electronic correlations are of significant importance during ionization.

Outlook

For future research endeavors, double ionization phenomena promise further insight into the electronic correlations, especially regarding the system's intrinsic dynamics prior to ionization, nuclear geometry and employed pulse parameters. Furthermore, the investigation of the electronic spin would provide useful information on the spin's role and its impact on the system's dynamics compared to Coulomb interactions, particle correlations, and external perturbations. Lastly, a simulation of real molecules has yet to be conducted.

ZUSAMMENFASSUNG

Die vorliegende Dissertation befasste sich mit zwei Fragestellungen aus dem Forschungsgebiet der Ultrakurzzeitdynamiken korrelierter Teilchen: Während im ersten Teil Asymmetrien im Photoelektronenspektrum eines Systems untersucht wurden, das von Elektron-Kern-Korrelationen dominiert wird, konzentrierte sich der zweite Teil auf die Wechselwirkung zwischen Elektronen miteinander. Eine detaillierte Analyse des ionisierenden Pulses im ersten Teil gewährte hierbei Einblicke in die auftretende Dynamik vor der Ionisation, wohingegen der genau Ionisationsmechanismus im zweiten Teil behandelt und die Dynamik, während und nach der Ionisation, beleuchtet wurde. Damit stehen die Ergebnisse des zweiten Teils in direktem Kontrast zur typischerweise verwendeten *Ein-Elektron-Näherung.*

Um die Elektron-Kern-Korrelationen zu analysieren, wurde die zeitabhängige Schrödingergleichung numerisch für ein Ladungstransfermodell exakt gelöst. Zunächst diente ein Infrarotpuls (IR-Puls) dazu, eine Dynamik innerhalb des Systems anzuregen, welche dann für verschiedene Zeiten mit einem ultrakurzen XUV-Puls untersucht wurde. Hierbei wies das berechnete Photoelektronenspektrum eine Asymmetrie für die verschiedenen Ionisationsrichtungen auf, welche anschließend verwendet werden konnte, um die korrelierte Dynamik des Systems zu entschlüsseln.

Berechnungen wurden dabei für zwei unterschiedliche Typen von Systemen angestellt: Während das eine System vornehmlich eine adiabatische Dynamik aufwies, d.h. die Elektronenbewegung passte sich adiabatisch an eine sich verändernde Kerngeometrie an, wurde das andere durch nicht-adiabatische Übergänge zu benachbarten elektronischen Zuständen charakterisiert. Für den Fall des adiabatischen Systems wurde gezeigt, dass die Asymmetrie im Photoelektronenspektrum die Elektronenbewegung vor der Ionisation widerspiegelt – und das sowohl wenn kein IR-Feld, aber auch wenn ein IR-Feld eine Dynamik im System angeregt hatte. Im Fall des diabatischen Systems wurde gezeigte, dass die Asymmetrie die Zeitpunkte der nicht-adiabatischen Übergänge anzeigt, jedoch die Bewegung der Elektronen zu anderen Zeiten nicht widerspiegelt.

Es wurde die Hypothese aufgestellt, dass die im Photoelektronenspektrum sichtbare Elektronendynamik durch zwei Dinge verursacht wird: der natürlich im System ablaufenden Dynamik, beschrieben durch die im System wirkenden Kräfte, und der durch das IR-Feld induzierten Dynamik. Um diese Theorie zu testen, wurden zwei Simulationen verglichen, bei denen die Phasen der IR-Pulse um π voneinander verschoben waren, und eine Technik vorgeschlagen, um die intrinsische Dynamik des Systems zu rekonstruieren. Es wurde gezeigt, dass sich die Gesamtdynamik des System im induzierten Teil unterscheidet, jedoch die intrinsische Dynamik erhalten bleibt. Daher können solche IR-Felder angewandt werden, um das Signal der Asymmetrie im Photoelektronenspektrum zu verstärken, und um gleichzeitig die ungestörte Dynamik zu untersuchen.

Des Weiteren wurde gezeigt, dass diese Rekonstruktionstechnik zu versagen beginnt, sobald die externen IR-Felder zu stark werden. Dann ist nämlich der induzierte Populationstransfer zwischen den verschiedenen elektronischen Zuständen nicht mehr vernachlässigbar, was zu einer neuen intrinsischen Dynamik führt.

Um die Eigenschaften des ionisierenden XUV-Pulses, welche am effizientesten für die Erzeugung der Asymmetrie sind, zu bestimmen, wurde das System zusätzlich mit einem Überlagerungszustand zweier benachbarter elektronischer Zustände konfiguriert. Hierbei erzeugte der Überlagerungszustand schnelle Oszillationen im Erwartungswert des Elektronenimpulses. Es wurde gezeigt, dass kurze XUV-Pulse die Asymmetrie im Photoelektronenspektrum signifikat erhöhen, da weniger optische Zyklen in den Pulsen ein kürzeres Wechselwirkungsfenster bedeuten, und der in der Asymmetrie widergespiegelte Elektronenimpuls somit genauer ist. Zusätzlich wurde durch eine Untersuchung der Frequenz des XUV-Pulses herausgefunden, dass Photonenergien, welche knapp oberhalb der Ionisationsschwelle liegen, bessere Ergebnisse erzielen, da die Ionisationswahrscheinlichkeit zu hohen Kontinuumszuständen drastisch sinkt.

Zusammenfassend befasste sich der erste Teil dieser Dissertation mit der Asymmetrie im Photoelektronenspektrum, von welcher gezeigt wurde, dass sie Informationen über die korrelierte Elektron-Kern-Dynamik beinhaltet – selbst wenn das System von einem externen IR-Feld gestört wurde. Darüber hinaus wurde demonstriert, wie mithilfe zweier phasenverschobener IR-Pulse die natürlich vorkommende Dynamik des molekularen Modellsystem genau nachgebildet werden kann.

Für den zweiten Teil der vorliegenden Arbeit wurde das zunächst verwendete Modellsystem um einen zweiten elektronischen Freiheitsgrad erweitert, sodass die Untersuchung von korrelierter Elektronendynamik möglich wurde. Hierbei lag der Fokus auf der Untersuchung der Dynamik, während und nach der Photoionisation eines einzelnen Elektrons mithilfe eines Attosekunden-XUV-Pulses. Da die Zeitentwicklung des betrachteten Systems exakt gelöst wurde, grenzt sich dieser Ansatz von anderen Techniken ab, die stark auf Näherungen beruhen, wie z.B. die Born-Oppenheimer- oder die Ein-Elektron-Näherung. Insbesondere die letztgenannte Technik vernachlässigt dabei Elektron-Elektron-

Korrelationen gänzlich, da sie u.A. eine Abschirmung der Coulomb-Abstoßung durch positive Kerne annimmt. Dementsprechend stehen die präsentierten Ergebnisse im starken Kontrast zu ihr und illustrieren ein deutlich genaueres Bild.

Die Analyse konzentrierte sich hierbei auf die Vibrationsdynamik eines Equilibriumszustandes des elektronischen Grundzustandes, da hier die Kerndynamik des System minimal ist. Als eine Konsequenz davon war eines der Elektronen schwächer gebunden als das andere, was eine veränderte Wechselwirkung mit dem ionisierenden XUV-Puls nach sich zog. Da Fermionen ununterscheidbare Teilchen sind, ist die Wellenfunktion, die benutzt wurde, um das System zu beschreiben, symmetrisch in den elektronischen Koordinaten, sodass Aussagen über den elektronischen Ursprung des gemessenen Ionisationssignals unmöglich sind. Um Ursprung des Ionisationssignals dennoch zurückzuverfolgen, und damit das schwach- vom starkgebundenen Elektron unterscheiden zu können, wurden zwei künstliche Teilsysteme untersucht, bei denen die Symmetrie zwischen den elektronischen Koordinaten gebrochen wurde.

Dabei brachte die durchgeführte Analyse zu Tage, dass die Position des nicht-emittierten Elektrons, und die Richtung des emittierten Elektrons von zentraler Bedeutung für den Ionisationskanal sind. Hierzu wurde gezeigt, dass sich der Impuls des weiterhin gebundenen Elektrons für die unterschiedlichen Ionisationstypen unterscheidet. Zwei Fälle wurden identifiziert: einer, wo die Elektronenemission ohne direkte Streuung am anderen Elektron erfolgte; und einer, wo es zu elastischer und inelastischer Streuung vor der Emission kam, sodass im zurückbleibenden Elektron eine Dynamik induziert wurde.

Die Untersuchung der künstlichen Teilsysteme zeigte hierbei, dass das schwachgebundene Elektron keine präferierte Emissionsrichtung aufwies, das starkgebundene Elektron hingegen deutlich wahrscheinlicher in die Richtung emittiert wurde, in der es zu weniger Streuung kam. Darüber hinaus wurde herausgefunden, dass es bei der Emission des starkgebundenen Elektrons zu deutlich mehr Streuung am anderen Elektron kommt. Daraus stellte sich die Frage, ob die Streuung eine Folge, oder gar die Ursache der Ionisation war. Während im ersten Szenario die Streuung inelastisch erfolgen und eine Anregung im zurückbleibenden Elektron bedeuten würde, würde elastische Streuung bedeuten, dass das starkgebundene Elektron seinen Impuls an das andere Elektron abgibt, welches daraufhin emittiert wird. Gleichzeitig würde das starkgebundene Elektron dann die ursprüngliche Position des emittierten Elektrons einnehmen.

Um den genauen Ionisationsmechanismus weiter aufzuschlüsseln, wurde die Wechselwirkung des elektrischen Feldes auf ein Elektron beschränkt, und der elektronische Zustand des zurückbleibenden Elektrons untersucht. Es wurde herausgefunden, dass bei Emission des schwachgebundenen Elektrons das zurückbleibende Elektron weiter den Grundzustand besetzt – unabhängig davon, ob es zu einem Streuprozess kam. Als eine Konsequenz bedeutete dies, dass es zu keiner Reorganisation der Kerngeometrie kam. Im Kontrast dazu führte die Emission des starkgebundenen Elektrons zu einem sogenannten *shake-up* im anderen Elektron, d.h. durch die Emission wurde das zurückbleibende, schwachgebundene Elektron in einen höheren elektronischen Zustand angeregt. Dies wiederum zog dann eine Reorganisation der Kerngeometrie nach sich, was durch nicht-adiabatische Übergänge zwischen verschiedenen elektronischen Zuständen begleitet wurde. Um die induzierte Kernbewegung als Ursache dieses Populations-transfers zu identifizieren, wurden weitere Rechnungen, dieses Mal jedoch mit eingefrorener Kerngeometrie, durchgeführt und es zeigte sich, dass der Populationstransfer in der Tat unterdrückt werden konnte, was damit diese These bestätigte.

Mit Beschränkung der Feldwechselwirkung auf das Elektron, was schlussendlich nicht emittiert wird, konnte die Menge des Ionisationssignals identifiziert werden, welche auf elastische Streuung zurückgeht. Damit konnte dann eine Aussage über die Genauigkeit der Ein-Elektron-Näherung gemacht werden: Während eine Beschränkung der Feldwechselwirkung auf das schwachgebundene Elektron zu einer Reduktion des gesamten Ionisationssignal um eine ganze Größenordnung führte, blieb das Signal bei Beschränkung der Feldwechselwirkung auf das starkgebundene Elektron auf dem gleichen Niveau. Das bedeutet, dass Elektron-Elektron-Korrelationen in diesem Fall signifikant zum Ionisationsprozess beitragen und nicht vernachlässigt werden können. Eine weitere Beobachtung bzgl. der elastischen Streuung und Beschränkung der Feldwechselwirkung auf das Elektron, was schlussendlich nicht emittiert wird, war, dass der elektronische Zustand des verbleibenden Elektrons nun vielmehr dem des anderen Elektrons ähnelte, wenn dieses weiterhin gebunden geblieben wäre.

Zuletzt wurde die Impulsverteilung des Photoelektrons in Hinblick auf die verschiedenen Ionisationsmechanismen untersucht. Hier zeigte sich, dass der Separationsansatz in die künstlichen Teilsysteme gute Übereinstimmung mit dem vollen System aufweist.

Zusammenfassend wurden in der vorgelegten Dissertation zwei elektronische Freiheitsgrad verwandt, um die Korrelation zwischen Elektronen zu untersuchen, während es zu Einfachionisation durch einen Attosekunden-XUV-Puls kommt. Durch die Verwendung von künstlichen Teilsystemen wurden verschiedene Ionisationsmechanismen, wie sie in voll-symmetrischen fermioni-schen Systemen vorkommen, im Detail analysiert. Als Schlüsselergebnis wurde hervorgehoben, wie entscheidend elektronische Korrelationen bei Ionisationsprozessen sind.

Ausblick

Für zukünftige Untersuchungen bietet sich eine genauere Betrachtung von Doppelionisationsphänomenen an, da hier elektronische Korrelationen auch noch nach dem Moment der Ionisation von entscheidender Bedeutung sind. Darüber hinaus sollten der Einfluss unterschiedlicher Kerngeometrien und die gewählten Eigenschaften des ionisierenden Pulses genauer analysiert werden. Weiterhin ist die Rolle des elektronischen Spins im Kontext der Systemdynamik, von Coulomb-Wechselwirkungen, anderer Teilchenkorrelationen und externer Störungen zu bewerten. Zuletzt bleibt noch die Simulation realer Moleküle.

List of Figures

BIBLIOGRAPHY

[1] David Bardell. The invention of the microscope. *Bios*, 75(2):78–84, 2004.

[2] Henry C King. *The history of the telescope.* Courier Corporation, 2003.

[3] VASCO RONCHI. Anno xxx gennaio-febbraio 1975. *Atti Della Fondazione Giorgio Ronchi E Contributi Dell'Istituto Nazionale Di Ottica*, 30:554, 1975.

[4] J. C. D. Brand. *Lines of light : the sources of dispersive spectroscopy, 1800-1930.* Gordon and Breach, Australia, 1995.

[5] John Frederick William Herschel. Xxxi. on the absorption of light by coloured media, and on the colours of the prismatic spectrum exhibited by certain flames; with an account of a ready mode of determining the absolute dispersive power of any medium, by direct experiment. *Earth and Environmental Science Transactions of The Royal Society of Edinburgh*, 9(2):445–460, 1823.

[6] William Henry Fox Talbot. *Some experiments on coloured flamesmicroform.* Edinburgh : William Blackwood ; London : T. Cadell, 1826.

[7] Pieter Zeeman. Over den invloed eener magnetisatie op den aard van het door een stof uitgezonden licht. pages 181–184,242–248. Koninklijke Akademie van Wetenschappen te Amsterdam, 1896.

[8] R Gordon Gould et al. The laser, light amplification by stimulated emission of radiation. In *The Ann Arbor conference on optical pumping, the University of Michigan*, volume 15, page 128, 1959.

[9] Joachim Ullrich, Artem Rudenko, and Robert Moshammer. Free-electron lasers: New avenues in molecular physics and photochemistry. *Annual Review of Physical Chemistry*, 63:635–660, 2012.

[10] RW Schoenlein, S Chattopadhyay, HHW Chong, TE Glover, PA Heimann, CV Shank, AA Zholents, and MS Zolotorev. Generation of femtosecond pulses of synchrotron radiation. *Science*, 287(5461):2237–2240, 2000.

[11] Wet al Ackermann, G Asova, V Ayvazyan, A Azima, N Baboi, J Bähr, V Balandin, B Beutner, A Brandt, A Bolzmann, et al. Operation of

a free-electron laser from the extreme ultraviolet to the water window. *Nature Photonics*, 1(6):336, 2007.

[12] Paul Emma, R Akre, J Arthur, R Bionta, C Bostedt, J Bozek, A Brachmann, P Bucksbaum, Ryan Coffee, F-J Decker, et al. First lasing and operation of an ångstrom-wavelength free-electron laser. *Nature Photonics*, 4(9):641, 2010.

[13] Tetsuya Ishikawa, Hideki Aoyagi, Takao Asaka, Yoshihiro Asano, Noriyoshi Azumi, Teruhiko Bizen, Hiroyasu Ego, Kenji Fukami, Toru Fukui, Yukito Furukawa, et al. A compact x-ray free-electron laser emitting in the sub-ångström region. *Nature Photonics*, 6(8):540, 2012.

[14] Ferenc Krausz and Misha Ivanov. Attosecond physics. *Reviews of Modern Physics*, 81(1):163, 2009.

[15] Mauro Nisoli and Giuseppe Sansone. New frontiers in attosecond science. *Progress in Quantum Electronics*, 33(1):17–59, 2009.

[16] Giuseppe Sansone, Luca Poletto, and Mauro Nisoli. High-energy attosecond light sources. *Nature Photonics*, 5(11):655, 2011.

[17] Tenio Popmintchev, Ming-Chang Chen, Dimitar Popmintchev, Paul Arpin, Susannah Brown, Skirmantas Ališauskas, Giedrius Andriukaitis, Tadas Balčiunas, Oliver D Mücke, Audrius Pugzlys, et al. Bright coherent ultrahigh harmonics in the kev x-ray regime from mid-infrared femtosecond lasers. *Science*, 336(6086):1287–1291, 2012.

[18] Eleftherios Goulielmakis, Martin Schultze, M Hofstetter, Vladislav S Yakovlev, Justin Gagnon, M Uiberacker, Andrew L Aquila, EM Gullikson, David T Attwood, Reinhard Kienberger, et al. Single-cycle nonlinear optics. *Science*, 320(5883):1614–1617, 2008.

[19] Franck Lépine, Misha Y. Ivanov, and Marc J. J. Vrakking. Attosecond molecular dynamics: fact or fiction? *Nature Photonics*, 8:195 EP –, Feb 2014. Review Article.

[20] Felix Plasser, Mario Barbatti, Adélia JA Aquino, and Hans Lischka. Electronically excited states and photodynamics: a continuing challenge. *Theoretical Chemistry Accounts*, 131(1):1073, 2012.

[21] John C Tully. Perspective: Nonadiabatic dynamics theory. *The Journal of Chemical Physics*, 137(22):22A301, 2012.

[22] Heinz Dürr and Henri Bouas-Laurent. *Photochromism: molecules and systems*. Elsevier, 2003.

[23] Micol Alemani, Maike V Peters, Stefan Hecht, Karl-Heinz Rieder, Francesca Moresco, and Leonhard Grill. Electric field-induced isomerization of azobenzene by stm. *Journal of the American Chemical Society*, 128(45):14446–14447, 2006.

[24] Matthew J Comstock, Niv Levy, Armen Kirakosian, Jongweon Cho, Frank Lauterwasser, Jessica H Harvey, David A Strubbe, Jean MJ Fréchet, Dirk Trauner, Steven G Louie, et al. Reversible photomechanical switching of individual engineered molecules at a metallic surface. *Physical Review Letters*, 99(3):038301, 2007.

[25] Roseanne J Sension, Stephen T Repinec, Arpad Z Szarka, and Robin M Hochstrasser. Femtosecond laser studies of the cis-stilbene photoisomerization reactions. *The Journal of Chemical Physics*, 98(8):6291–6315, 1993.

[26] David H Waldeck. Photoisomerization dynamics of stilbenes. *Chemical Reviews*, 91(3):415–436, 1991.

[27] RW Schoenlein, LA Peteanu, RA Mathies, and CV Shank. The first step in vision: femtosecond isomerization of rhodopsin. *Science*, 254(5030):412–415, 1991.

[28] Dario Polli, Piero Altoè, Oliver Weingart, Katelyn M Spillane, Cristian Manzoni, Daniele Brida, Gaia Tomasello, Giorgio Orlandi, Philipp Kukura, Richard A Mathies, et al. Conical intersection dynamics of the primary photoisomerization event in vision. *Nature*, 467(7314):440, 2010.

[29] Richard A Mathies, CH Brito Cruz, Walter T Pollard, and Charles V Shank. Direct observation of the femtosecond excited-state cis-trans isomerization in bacteriorhodopsin. *Science*, 240(4853):777–779, 1988.

[30] S Schenkl, F Van Mourik, G Van der Zwan, S Haacke, and M Chergui. Probing the ultrafast charge translocation of photoexcited retinal in bacteriorhodopsin. *Science*, 309(5736):917–920, 2005.

[31] Gerrit Groenhof, Mathieu Bouxin-Cademartory, Berk Hess, Sam P De Visser, Herman JC Berendsen, Massimo Olivucci, Alan E Mark, and Michael A Robb. Photoactivation of the photoactive yellow protein: why photon absorption triggers a trans-to-cis isomerization of the chromophore in the protein. *Journal of the American Chemical Society*, 126(13):4228–4233, 2004.

[32] Chris T Middleton, Kimberly de La Harpe, Charlene Su, Yu Kay Law, Carlos E Crespo-Hernández, and Bern Kohler. DNA excited-state dynamics: from single bases to the double helix. *Annual Review of Physical Chemistry*, 60:217–239, 2009.

[33] Carlos E Crespo-Hernández, Boiko Cohen, Patrick M Hare, and Bern Kohler. Ultrafast excited-state dynamics in nucleic acids. *Chemical reviews*, 104(4):1977–2020, 2004.

[34] Wolfgang J Schreier, Tobias E Schrader, Florian O Koller, Peter Gilch, Carlos E Crespo-Hernández, Vijay N Swaminathan, Thomas Carell, Wolfgang Zinth, and Bern Kohler. Thymine dimerization in DNA is an ultrafast photoreaction. *Science*, 315(5812):625–629, 2007.

[35] E Teller. Internal conversion in polyatomic molecules. *Israel Journal of Chemistry*, 7(2):227–235, 1969.

[36] H Köppel, W Domcke, and LS Cederbaum. Green's function method in quantum chemistry. *Adv. Chem. Phys*, 57:59–132, 1984.

[37] Fernando Bernardi, Massimo Olivucci, and Michael A Robb. Potential energy surface crossings in organic photochemistry. *Chemical Society Reviews*, 25(5):321–328, 1996.

[38] Graham A Worth and Lorenz S Cederbaum. Beyond Born-Oppenheimer: molecular dynamics through a conical intersection. *Annu. Rev. Phys. Chem.*, 55:127–158, 2004.

[39] W Domcke, DR Yarkony, and H Köppel. Conical intersections: electronic structure. *Dynamics and Spectroscopy (Adv. Ser. in Phys. Chem., Vol. 15, World Scientific, 2004)*, 2004.

[40] Conical Intersections. Theory, computation and experiment, edited by W. Domcke, DR Yarkony, and H. Köppel, 2011.

[41] Ch Neidel, J Klei, C-H Yang, A Rouzée, MJJ Vrakking, K Klünder, M Miranda, CL Arnold, T Fordell, A L'Huillier, et al. Probing time-dependent molecular dipoles on the attosecond time scale. *Physical Review Letters*, 111(3):033001, 2013.

[42] Jakob Juul Larsen, Hirofumi Sakai, CP Safvan, Ida Wendt-Larsen, and Henrik Stapelfeldt. Aligning molecules with intense nonresonant laser fields. *The Journal of Chemical Physics*, 111(17):7774–7781, 1999.

[43] Markus Kitzler and Stefanie Gräfe. *Ultrafast Dynamics Driven by Intense Light Pulses*, volume 86. Springer, 2015.

[44] Richard Neutze, Remco Wouts, David van der Spoel, Edgar Weckert, and Janos Hajdu. Potential for biomolecular imaging with femtosecond x-ray pulses. *Nature*, 406(6797):752, 2000.

[45] Kiyoshi Ueda. High-resolution inner-shell spectroscopies of free atoms and molecules using soft-x-ray beamlines at the third-generation synchrotron radiation sources. *Journal of Physics B: Atomic, Molecular and Optical Physics*, 36(4):R1, 2003.

[46] U Becker and D Shirley. Partial cross section and angular distribution vuv and soft x-ray photoionization, 1996.

[47] Joachim Stöhr. *NEXAFS spectroscopy*, volume 25. Springer Science & Business Media, 2013.

[48] Anders Nilsson, Lars GM Pettersson, and Jens Norskov. *Chemical bonding at surfaces and interfaces*. Elsevier, 2011.

[49] Simon Schreck, Gianina Gavrila, Christian Weniger, and Philippe Wernet. A sample holder for soft x-ray absorption spectroscopy of liquids in transmission mode. *Review of Scientific Instruments*, 82(10):103101, 2011.

[50] Masatoshi Ukai, Akinari Yokoya, Kentaro Fujii, and Yuji Saitoh. X-ray absorption spectra of nucleotides (amp, gmp, and cmp) in liquid water solutions near the nitrogen k-edge. *Chemical Physics Letters*, 495(1-3):90–95, 2010.

[51] H Siegbahn, L Asplund, and P Kelfve. The Auger electron spectrum of water vapour. *Chemical Physics Letters*, 35(3):330–335, 1975.

[52] Eric Henry Stoneley Burhop. *The Auger effect and other radiationless transitions*. Cambridge University Press, 2014.

[53] Walter Bambynek, Bernd Crasemann, RW Fink, H-U Freund, Hans Mark, CD Swift, RE Price, and P Venugopala Rao. X-ray fluorescence yields, Auger, and Coster-Kronig transition probabilities. *Reviews of Modern Physics*, 44(4):716, 1972.

[54] Stephan Hüfner. *Photoelectron spectroscopy: principles and applications*. Springer Science & Business Media, 2013.

[55] Maria Krikunova, Theophilos Maltezopoulos, Philipp Wessels, Moritz Schlie, Armin Azima, Marek Wieland, and Markus Drescher. Ultrafast photofragmentation dynamics of molecular iodine driven with timed

xuv and near-infrared light pulses. *The Journal of Chemical Physics*, 134(2):024313, 2011.

[56] Marc JJ Vrakking. Attosecond imaging. *Physical Chemistry Chemical Physics*, 16(7):2775–2789, 2014.

[57] W Siu, F Kelkensberg, G Gademann, A Rouzée, Per Johnsson, D Dowek, Matteo Lucchini, Francesca Calegari, U De Giovannini, A Rubio, et al. Attosecond control of dissociative ionization of O_2 molecules. *Physical Review A*, 84(6):063412, 2011.

[58] Reinhard Kienberger, Eleftherios Goulielmakis, Matthias Uiberacker, Andrius Baltuska, Vladislav Yakovlev, Ferdinand Bammer, Armin Scrinzi, Th Westerwalbesloh, Ulf Kleineberg, Ulrich Heinzmann, et al. Atomic transient recorder. *Nature*, 427(6977):817, 2004.

[59] Marcus Ossiander, Florian Siegrist, Vage Shirvanyan, R Pazourek, Annkatrin Sommer, Tobias Latka, Alexander Guggenmos, S Nagele, J Feist, J Burgdörfer, et al. Attosecond correlation dynamics. *Nature Physics*, 13(3):280, 2017.

[60] Manohar Awasthi, Yulian V Vanne, Alejandro Saenz, Alberto Castro, and Piero Decleva. Single-active-electron approximation for describing molecules in ultrashort laser pulses and its application to molecular hydrogen. *Physical Review A*, 77(6):063403, 2008.

[61] Manohar Awasthi and Alejandro Saenz. Breakdown of the single-active-electron approximation for one-photon ionization of the $B^1\Sigma_u^+$ state of H_2 exposed to intense laser fields. *Physical Review A*, 81(6):063406, 2010.

[62] S Gräfe, D Scheidel, V Engel, Niels Engholm Henriksen, and Klaus Braagaard Møller. Approaches to wave packet imaging using femtosecond ionization spectroscopy. *The Journal of Physical Chemistry A*, 108(41):8954–8960, 2004.

[63] Stefanie Gräfe and Volker Engel. Local control theory applied to coupled electronic and nuclear motion. *Chemical Physics*, 329(1-3):118–125, 2006.

[64] Mirjam Falge, Patricia Vindel-Zandbergen, Volker Engel, Manfred Lein, Bo Y Chang, and Ignacio R Sola. The time-scale of nonlinear events driven by strong fields: can one control the spin coupling before ionization runs over? *Journal of Physics B: Atomic, Molecular and Optical Physics*, 47(12):124027, 2014.

[65] Mirjam Falge, Volker Engel, Manfred Lein, Patricia Vindel-Zandbergen, Bo Y Chang, and Ignacio R Sola. Quantum wave-packet dynamics in spin-coupled vibronic states. *The Journal of Physical Chemistry A*, 116(46):11427–11433, 2012.

[66] Mirjam Falge, Volker Engel, and Stefanie Gräfe. Fingerprints of adiabatic versus diabatic vibronic dynamics in the asymmetry of photoelectron momentum distributions. *The Journal of Physical Chemistry Letters*, 3(18):2617–2620, 2012.

[67] Mirjam Falge, Volker Engel, and Stefanie Gräfe. Time-resolved photoelectron spectroscopy of coupled electron-nuclear motion. *The Journal of Chemical Physics*, 134(18):184307, 2011.

[68] M Erdmann, EKU Gross, and V Engel. Time-dependent electron localization functions for coupled nuclear-electronic motion. *The Journal of Chemical Physics*, 121(19):9666–9670, 2004.

[69] M Erdmann, S Baumann, S Gräfe, and V Engel. Electronic predissociation: a model study. *The European Physical Journal D-Atomic, Molecular, Optical and Plasma Physics*, 30(3):327–333, 2004.

[70] M Erdmann and V Engel. Combined electronic and nuclear dynamics in a simple model system. ii. spectroscopic transitions. *The Journal of Chemical Physics*, 120(1):158–164, 2004.

[71] M Erdmann, P Marquetand, and V Engel. Combined electronic and nuclear dynamics in a simple model system. *The Journal of Chemical Physics*, 119(2):672–679, 2003.

[72] Eugen Merzbacher. *Quantum mechanics*. Wiley, New York, 1998.

[73] Ira Levine. *Quantum chemistry*. Prentice Hall, 1991.

[74] Claude Cohen-Tannoudji, Bernard Diu, Laloë Franck, Susan Reid Hemley, Nicole Ostrowsky, and Dan Ostrowsky. *Quantum mechanics*, pages 308–311. Wiley-VCH Verlag, 2011.

[75] Charles Jean Joachain. Quantum collision theory. 1975.

[76] MD Feit, JA Fleck Jr, and A Steiger. Solution of the Schrödinger equation by a spectral method. *Journal of Computational Physics*, 47(3):412–433, 1982.

[77] Claude Cohen-Tannoudji, Bernard Diu, Laloë Franck, Susan Reid Hemley, Nicole Ostrowsky, and Dan Ostrowsky. *Quantum mechanics*, pages 173–175. Wiley-VCH Verlag, 2011.

[78] JA Fleck, JR Morris, and MD Feit. Time-dependent propagation of high energy laser beams through the atmosphere. *Applied physics*, 10(2):129–160, 1976.

[79] Masuo Suzuki. Generalized trotter's formula and systematic approximants of exponential operators and inner derivations with applications to many-body problems. *Communications in Mathematical Physics*, 51(2):183–190, 1976.

[80] Gilbert Strang. On the construction and comparison of difference schemes. *SIAM Journal on Numerical Analysis*, 5(3):506–517, 1968.

[81] Haruo Yoshida. Construction of higher order symplectic integrators. *Physics letters A*, 150(5-7):262–268, 1990.

[82] Ronnie Kosloff and H Tal-Ezer. A direct relaxation method for calculating eigenfunctions and eigenvalues of the Schrödinger equation on a grid. *Chemical Physics Letters*, 127(3):223–230, 1986.

[83] Emile S Medvedev and Vladimir I Osherov. Radiationless transitions in polyatomic molecules. *Springer series in Chemical Physics*, pages 128–133, 1995.

[84] David Joshua Tannor. *Introduction to quantum mechanics: a time-dependent perspective*. University Science Books, 2007.

[85] Max Born and Kun Huang. *Dynamical theory of crystal lattices*. Clarendon press, 1954.

[86] Max Born and Robert Oppenheimer. Zur Quantentheorie der Molekeln. *Annalen der Physik*, 389(20):457–484, 1927.

[87] Nicholas C Handy and Aaron M Lee. The adiabatic approximation. *Chemical Physics letters*, 252(5-6):425–430, 1996.

[88] Bruce A Schumm. *Deep down things: The breathtaking beauty of particle physics*, chapter 8. JHU Press, 2004.

[89] John David Jackson. From lorenz to coulomb and other explicit gauge transformations. *American Journal of Physics*, 70(9):917–928, 2002.

[90] Robert Heather and Horia Metiu. An efficient procedure for calculating the evolution of the wave function by fast fourier transform methods for systems with spatially extended wave function and localized potential. *The Journal of Chemical Physics*, 86(9):5009–5017, 1987.

[91] A Keller. Asymptotic analysis in time-dependent calculations with divergent coupling. *Phys. Rev. A*, 52:1450, 1995.

[92] Fritz Ehlotzky. *Quantenmechanik und ihre Anwendungen*, chapter A.6.3. Springer-Verlag, 2006.

[93] Andre Ludwig, Jochen Maurer, BW Mayer, CR Phillips, Lukas Gallmann, and Ursula Keller. Breakdown of the dipole approximation in strong-field ionization. *Physical Review Letters*, 113(24):243001, 2014.

[94] Ronnie Kosloff. Quantum molecular dynamics on grids. *Dynamics of molecules and chemical reactions*, pages 185–230, 1996.

[95] Alexander Schubert. Kohärente und dissipative Wellenpaketdynamik und zeitaufgelöste Spektroskopie: Von zweiatomigen Molekülen zu molekularen Aggregaten, 2012.

[96] Matteo Frigo and Steven G Johnson. The design and implementation of fftw3. *Proceedings of the IEEE*, 93(2):216–231, 2005.

[97] Seokmin Shin and Horia Metiu. Nonadiabatic effects on the charge transfer rate constant: A numerical study of a simple model system. *The Journal of Chemical Physics*, 102(23):9285–9295, 1995.

[98] Seokmin Shin and Horia Metiu. Multiple time scale quantum wavepacket propagation: electron- nuclear dynamics. *The Journal of Physical Chemistry*, 100(19):7867–7872, 1996.

[99] NP Blake, Vl Srdanov, GD Stucky, and H Metiu. A model for electron-zeolite Na$^+$-zeolite interactions: Frame charges and ionic sizes. *The Journal of Physical Chemistry*, 99(7):2127–2133, 1995.

[100] Nick P Blake and H Metiu. Absorption spectrum calculations for a system having a few quantum and many “classical” degrees of freedom. *The Journal of Chemical Physics*, 101(1):223–230, 1994.

[101] Jörn Manz and Ludger Wöste. *Femtosecond chemistry*, volume 2. VCH, 1995.

[102] Andrius Baltuška, Th Udem, M Uiberacker, M Hentschel, Eleftherios Goulielmakis, Ch Gohle, Ronald Holzwarth, VS Yakovlev, A Scrinzi, Th W Hänsch, et al. Attosecond control of electronic processes by intense light fields. *Nature*, 421(6923):611, 2003.

[103] J Itatani, F Quéré, Gennady L Yudin, M Yu Ivanov, Ferenc Krausz, and Paul B Corkum. Attosecond streak camera. *Physical Review Letters*, 88(17):173903, 2002.

[104] Markus Kitzler, Nenad Milosevic, Armin Scrinzi, Ferenc Krausz, and Thomas Brabec. Quantum theory of attosecond xuv pulse measurement by laser dressed photoionization. *Physical Review Letters*, 88(17):173904, 2002.

[105] Eleftherios Goulielmakis, Matthias Uiberacker, Reinhard Kienberger, Andrius Baltuska, Vladislav Yakovlev, Armin Scrinzi, Th Westerwalbesloh, U Kleineberg, Ulrich Heinzmann, Markus Drescher, et al. Direct measurement of light waves. *Science*, 305(5688):1267–1269, 2004.

[106] Ferenc Krausz and Mark I Stockman. Attosecond metrology: from electron capture to future signal processing. *Nature Photonics*, 8(3):205, 2014.

[107] M Hentschel, R Kienberger, Ch Spielmann, Georg A Reider, N Milosevic, Thomas Brabec, Paul Corkum, Ulrich Heinzmann, Markus Drescher, and Ferenc Krausz. Attosecond metrology. *Nature*, 414(6863):509, 2001.

[108] Reinhard Kienberger, Michael Hentschel, Matthias Uiberacker, Ch Spielmann, Markus Kitzler, Armin Scrinzi, M Wieland, Th Westerwalbesloh, U Kleineberg, Ulrich Heinzmann, et al. Steering attosecond electron wave packets with light. *Science*, 297(5584):1144–1148, 2002.

[109] Thomas Brabec and Ferenc Krausz. Intense few-cycle laser fields: Frontiers of nonlinear optics. *Reviews of Modern Physics*, 72(2):545, 2000.

[110] Wolfgang Domcke and Gerhard Stock. Theory of ultrafast nonadiabatic excited-state processes and their spectroscopic detection in real time. *Advances in Chemical Physics*, 100:1–169, 1997.

[111] JA Davies, RE Continetti, DW Chandler, and CC Hayden. Femtosecond time-resolved photoelectron angular distributions probed during photodissociation of no 2. *Physical Review Letters*, 84(26):5983, 2000.

[112] Albert Stolow, Arthur E Bragg, and Daniel M Neumark. Femtosecond time-resolved photoelectron spectroscopy. *Chemical reviews*, 104(4):1719–1758, 2004.

[113] Toshinori Suzuki. Femtosecond time-resolved photoelectron imaging. *Annu. Rev. Phys. Chem.*, 57:555–592, 2006.

[114] SA Aseyev, Yicheng Ni, LJ Frasinski, HG Muller, and MJJ Vrakking. Attosecond angle-resolved photoelectron spectroscopy. *Physical Review Letters*, 91(22):223902, 2003.

[115] Thomas Pfeifer, Mark J Abel, Phillip M Nagel, Aurélie Jullien, Zhi-Heng Loh, M Justine Bell, Daniel M Neumark, and Stephen R Leone. Time-resolved spectroscopy of attosecond quantum dynamics. *Chemical Physics Letters*, 463(1-3):11–24, 2008.

[116] MF Kling, Ch Siedschlag, Aart J Verhoef, JI Khan, Martin Schultze, Th Uphues, Yicheng Ni, Matthias Uiberacker, M Drescher, Ferenc Krausz, et al. Control of electron localization in molecular dissociation. *Science*, 312(5771):246–248, 2006.

[117] Paul Hockett, Christer Z Bisgaard, Owen J Clarkin, and Albert Stolow. Time-resolved imaging of purely valence-electron dynamics during a chemical reaction. *Nature Physics*, 7(8):612, 2011.

[118] Yasuki Arasaki, Kazuo Takatsuka, Kwanghsi Wang, and Vincent McKoy. Femtosecond energy-and angle-resolved photoelectron spectra. *Chemical Physics letters*, 302(5-6):363–374, 1999.

[119] Márcio T do N Varella, Yasuki Arasaki, Hiroshi Ushiyama, Vincent McKoy, and Kazuo Takatsuka. Time-resolved photoelectron spectroscopy of proton transfer in the ground state of chloromalonaldehyde: Wave-packet dynamics on effective potential surfaces of reduced dimensionality. *The Journal of Chemical Physics*, 124(15):154302, 2006.

[120] Yasuki Arasaki, Kwanghsi Wang, Vincent McKoy, and Kazuo Takatsuka. Nuclear and electron dynamics from femto-and subfemto-second time-resolved photoelectron angular distributions. *Journal of Physics B: Atomic, Molecular and Optical Physics*, 45(19):194006, 2012.

[121] Kwanghsi Wang, Vincent McKoy, Paul Hockett, Albert Stolow, and Michael S Schuurman. Monitoring non-adiabatic dynamics in cs2 with time-and energy-resolved photoelectron spectra of wavepackets. *Chemical Physics Letters*, 683:579–585, 2017.

[122] Tamar Seideman. Time-resolved photoelectron angular distributions as a probe of coupled polyatomic dynamics. *Physical Review A*, 64(4):042504, 2001.

[123] Tamar Seideman. Time-resolved photoelectron angular distributions: Concepts, applications, and directions. *Annual Review of Physical Chemistry*, 53(1):41–65, 2002.

[124] GL Yudin, AD Bandrauk, and PB Corkum. Chirped attosecond photoelectron spectroscopy. *Physical Review Letters*, 96(6):063002, 2006.

[125] Olga Smirnova, Michael Spanner, and Misha Yu Ivanov. Coulomb and polarization effects in laser-assisted xuv ionization. *Journal of Physics B: Atomic, Molecular and Optical Physics*, 39(13):S323, 2006.

[126] Stefanie Gräfe, Volker Engel, and Misha Yu Ivanov. Attosecond photoelectron spectroscopy of electron tunneling in a dissociating hydrogen molecular ion. *Physical Review Letters*, 101(10):103001, 2008.

[127] Uwe Manthe. Optimized unoccupied single-particle functions in the (multi-layer) multi-configurational time-dependent Hartree approach. *Chemical Physics*, 515:279–286, 2018.

[128] Haobin Wang. Multilayer multiconfiguration time-dependent Hartree theory. *The Journal of Physical Chemistry A*, 119(29):7951–7965, 2015.

[129] Ali Abedi, Federica Agostini, Yasumitsu Suzuki, and EKU Gross. Dynamical steps that bridge piecewise adiabatic shapes in the exact time-dependent potential energy surface. *Physical Review Letters*, 110(26):263001, 2013.

[130] Federica Agostini, Ali Abedi, Yasumitsu Suzuki, Seung Kyu Min, Neepa T Maitra, and EKU Gross. The exact forces on classical nuclei in non-adiabatic charge transfer. *The Journal of Chemical Physics*, 142(8):084303, 2015.

[131] Julian Albert, Dustin Kaiser, and Volker Engel. Communication: Adiabatic and non-adiabatic electron-nuclear motion: Quantum and classical dynamics, 2016.

[132] Kilian Hader, Julian Albert, EKU Gross, and Volker Engel. Electron-nuclear wave-packet dynamics through a conical intersection. *The Journal of Chemical Physics*, 146(7):074304, 2017.

[133] Mirjam Falge, Friedrich Georg Fröbel, Volker Engel, and Stefanie Gräfe. Time-resolved photoelectron spectroscopy of ir-driven electron dynamics in a charge transfer model system. *Physical Chemistry Chemical Physics*, 19(30):19683–19690, 2017.

[134] VI Matveev and É S Parilis. Shake-up processes accompanying electron transitions in atoms. *Soviet Physics Uspekhi*, 25(12):881, 1982.

[135] Friedrich Georg Fröbel, Ulf Peschel, Stefanie Gräfe, and Alexander Schubert. Attosecond ionization dynamics in a molecular charge-transfer system with correlated electrons. 2019.

[136] KC Kulander. Time-dependent theory of multiphoton ionization of xenon. *Physical Review A*, 38(2):778, 1988.

[137] Matthias Uiberacker, Th Uphues, Martin Schultze, Aart Johannes Verhoef, Vladislav Yakovlev, Matthias F Kling, Jens Rauschenberger, Nicolai M Kabachnik, Hartmut Schröder, Matthias Lezius, et al. Attosecond real-time observation of electron tunnelling in atoms. *Nature*, 446(7136):627, 2007.

[138] Paul Corkum and Ferenc Krausz. Attosecond science. *Nature physics*, 3(6):381, 2007.

[139] Francesca Calegari, Andrea Trabattoni, Alicia Palacios, David Ayuso, Mattea C Castrovilli, Jason B Greenwood, Piero Decleva, Fernando Martín, and Mauro Nisoli. Charge migration induced by attosecond pulses in bio-relevant molecules. *Journal of Physics B: Atomic, Molecular and Optical Physics*, 49(14):142001, 2016.

[140] Sergey Zherebtsov, Adrian Wirth, Thorsten Uphues, Irina Znakovskaya, Oliver Herrwerth, Justin Gagnon, Michael Korbman, Vladislav S Yakovlev, MJJ Vrakking, M Drescher, et al. Attosecond imaging of xuv-induced atomic photoemission and Auger decay in strong laser fields. *Journal of Physics B: Atomic, Molecular and Optical Physics*, 44(10):105601, 2011.

[141] Renate Pazourek, Stefan Nagele, and Joachim Burgdörfer. Attosecond chronoscopy of photoemission. *Reviews of Modern Physics*, 87(3):765, 2015.

[142] Renate Pazourek, Johannes Feist, Stefan Nagele, and Joachim Burgdörfer. Attosecond streaking of correlated two-electron transitions in helium. *Physical Review Letters*, 108(16):163001, 2012.

[143] Suren Sukiasyan, Kenichi L Ishikawa, and Misha Ivanov. Attosecond cascades and time delays in one-electron photoionization. *Physical Review A*, 86(3):033423, 2012.

[144] Kathrin Klünder, Per Johnsson, M Swoboda, Anne L'Huillier, Giuseppe Sansone, Mauro Nisoli, MJJ Vrakking, KJ Schafer, and Johan Mauritsson. Reconstruction of attosecond electron wave packets using quantum state holography. *Physical Review A*, 88(3):033404, 2013.

[145] AK Kazansky and Nikolay M Kabachnik. An attosecond time-resolved study of strong-field atomic photoionization. *Journal of Physics B: Atomic, Molecular and Optical Physics*, 40(21):F299, 2007.

[146] Qi-Cheng Ning, Liang-You Peng, Shu-Na Song, Wei-Chao Jiang, Stefan Nagele, Renate Pazourek, Joachim Burgdörfer, and Qihuang Gong. Attosecond streaking of Cohen-Fano interferences in the photoionization of H_2^+. *Physical Review A*, 90(1):013423, 2014.

[147] Howard D Cohen and U Fano. Interference in the photo-ionization of molecules. *Physical Review*, 150(1):30, 1966.

[148] PC Deshmukh, A Mandal, S Saha, AS Kheifets, VK Dolmatov, and ST Manson. Attosecond time delay in the photoionization of endohedral atoms A@ C 60: A probe of confinement resonances. *Physical Review A*, 89(5):053424, 2014.

[149] Renate Pazourek, Stefan Nagele, and Joachim Burgdörfer. Time-resolved photoemission on the attosecond scale: opportunities and challenges. *Faraday discussions*, 163:353–376, 2013.

[150] Françoise Remacle and RD Levine. Attosecond pumping of nonstationary electronic states of LiH: Charge shake-up and electron density distortion. *Physical Review A*, 83(1):013411, 2011.

[151] Holger Hennig, Jörg Breidbach, and Lorenz S Cederbaum. Electron correlation as the driving force for charge transfer: charge migration following ionization in n-methyl acetamide. *The Journal of Physical Chemistry A*, 109(3):409–414, 2005.

[152] Alexander I Kuleff and Lorenz S Cederbaum. Charge migration in different conformers of glycine: The role of nuclear geometry. *Chemical Physics*, 338(2-3):320–328, 2007.

[153] Françoise Remacle and RD Levine. An electronic time scale in chemistry. *Proceedings of the National Academy of Sciences*, 103(18):6793–6798, 2006.

[154] David Ayuso, Alicia Palacios, Piero Decleva, and Fernando Martín. Ultrafast charge dynamics in glycine induced by attosecond pulses. *Physical Chemistry Chemical Physics*, 19(30):19767–19776, 2017.

[155] Franck Lépine, Misha Y Ivanov, and Marc JJ Vrakking. Attosecond molecular dynamics: fact or fiction? *Nature Photonics*, 8(3):195, 2014.

[156] V Despré, A Marciniak, V Loriot, MCE Galbraith, A Rouzée, MJJ Vrakking, F Lépine, and AI Kuleff. Attosecond hole migration in benzene molecules surviving nuclear motion. *The Journal of Physical Chemistry Letters*, 6(3):426–431, 2015.

[157] Morgane Vacher, Michael J Bearpark, Michael A Robb, and João Pedro Malhado. Electron dynamics upon ionization of polyatomic molecules: Coupling to quantum nuclear motion and decoherence. *Physical Review Letters*, 118(8):083001, 2017.

[158] Morgane Vacher, Lee Steinberg, Andrew J Jenkins, Michael J Bearpark, and Michael A Robb. Electron dynamics following photoionization: Decoherence due to the nuclear-wave-packet width. *Physical Review A*, 92(4):040502, 2015.

[159] Shoutian Sun, Benoit Mignolet, Lin Fan, Wen Li, Raphael D Levine, and Francoise Remacle. Nuclear motion driven ultrafast photodissociative charge transfer of the penna cation: An experimental and computational study. *The Journal of Physical Chemistry A*, 121(7):1442–1447, 2017.

[160] Robert Eisberg and Robert Resnick. *Quantum physics of atoms, molecules, solids, nuclei, and particles.* Wiley, New York, 1985.

Selbstständigkeitserklärung

Ich erkläre, dass ich die vorliegende Arbeit selbständig und unter Verwendung der angegebenen Hilfsmittel, persönlichen Mitteilungen und Quellen angefertigt habe.

Jena, July 2, 2019 . . . .

Wissenschaftlicher Werdegang

seit 09/2015	**Doktorand der Physikalischen Chemie.** Friedrich-Schiller-Universität Jena, Institut für Physikalische Chemie AG Gräfe Teil der *International Research Training Group 2101*
10/2012 – 02/2015	**Master of Science, Physik.** Universität Hamburg Schwerpunkt: Ultrakalte Atome und laser-gekühlte Systeme Abschlussarbeit: *Multi-Band Spectroscopy in Triangular Lattices & Single-Shot 3D Imaging*
10/2008 – 10/2012	**Bachelor of Science, Physik.** Universität Hamburg Schwerpunkt: Festkörperphysik Abschlussarbeit: *Beugungsuntersuchung mit hochenergetischen Elektronen*
08/1999 – 06/2008	**Staatl. Gymnasium.** Bismarckschule Elmshorn Hauptfächer: Mathematik, Physik

Jena, July 2, 2019 ....

Acknowledgements

This work would not have been possible without the help of a few important people and the motivational aid of many others. Foremost I would like to thank Prof. Dr. Stefanie Gräfe, my supervising mentor, not only for being the first referee of this work, but for the opportunity to be part of the *International Research Training Group 2101*, which funded my project. The exchange with our Canadian partners has been an incredibly rewarding experience.

Dr. Alexander Schubert joined our group merely a year before I left, however, all the more did he contribute to my work in the form of daily discussions, research impulses, reviews and stimulating conversations beyond the scope of theoretical physics.

Further, I would like to thank Johannes Steinmetzer, Dr. Lun Yue, Philipp Traber, Michael Siegmann and Dr. Dirk Bender who assisted me in tackling all problems concerning IT and programming head-on and providing me with the basic chemistry knowledge I needed for supervising several pharmaceutical training courses.

Next to the aforementioned coworkers, I thank Dr. Stephan Kupfer, Dr. Martin Richter and Dr. Daniel Kinzel, Karl Michael Ziems, Kevin Fiederling, Matthias Paul and Phillip Seeber for an ever entertaining environment and barbecue sessions beyond count. I hope to share meat and mead with you in the future!

For the Canadian partnership, I extend my gratitude to Prof. Dr. François Légaré and Dr. Heide Ibrahim for a heartfelt welcoming in Montréal and our joint research endeavor concerning OCS. In this context, I also thank Carolin Müller for her aid in our Octopus calculations.

Beyond the day-to-day working life, there was also the social aspect in the setting of the *International Research Training Group 2101*. Trips across the Atlantic ocean brought back more than scientific results and I am glad calling many of you my friends.

Last, I want to thank my parents for their unquestionable faith and everlasting support. I love you.